LAWRENCE
LIVERMORE
NATIONAL
LABORATORY

LLNL-TR-760459

Numerical simulations of realistic grating compressors

N. A. Petersson, B. Sjogreen, S. Schrauth

October 25, 2018

Disclaimer

This work performed under the auspices of the U.S. Department of Energy by Lawrence Livermore National Laboratory under Contract DE-AC52-07NA27344.

Numerical simulations of realistic grating compressors

N. Anders Petersson* Björn Sjögreen* Samuel Schrauth†

October 25, 2018

*Center for Applied Scientific Computing, Lawrence Livermore National Laboratory, PO Box 808, Livermore CA 94551.

†National Ignition Facility, Lawrence Livermore National Laboratory, PO Box 808, Livermore CA 94551.

Contents

1 Introduction

Chirped pulse amplification (CPA), originally proposed by Strickland and Mourou [24, 18], is a critical enabling technology for creating very short laser pulses with very high peak power. It consists of three optical components: a stretcher, an amplifier, and a compressor. An initial laser pulse of short duration and low energy content is first stretched out in time by the stretcher, resulting in a pulse with longer duration, low energy content, and very low peak power. The pulse is then amplified to increase its energy content without changing its duration in time. The amplified pulse is finally compressed in time in the compressor, resulting in a laser pulse with very short duration and very high peak power. The objective of this work is to develop numerical techniques that enable small-scale grating abberations in the compressor to be analyzed through high performance computer simulations.

A short chirped laser pulse contains a continuous spectrum of frequencies. In a non-dispersive media, the angular frequency (ω) is related to the wave number (k) and the wavelength (λ) by

$$k = \frac{\omega}{c}, \quad \lambda = \frac{2\pi}{k} = \frac{2\pi c}{\omega},$$

where c is the speed of light. In the frequency domain, each frequency of the laser pulse corresponds to a monochromatic laser beam with a constant wave number and wavelength. To explain how a laser pulse is compressed in time it is instructive to consider how each frequency component propagates through the (usually four) diffraction gratings in a compressor [25].

A diffraction grating consists of a planar surface with parallel grooves, where the spacing between the grooves is on the order of the wavelength of light, see Figure 1. The grating equation

$$\sin\alpha + \sin\beta_m = \frac{m\lambda}{d_g}, \quad m = 0, \pm 1, \pm 2, \ldots, \tag{1}$$

describes the diffraction angles from one grating due to an incident beam of monochromatic light. Here, α is the angle of incidence, β_m is the angle of diffraction for order m, λ denotes the wavelength of the light, and d_g is the spacing between the grooves in the grating surface. Figure 1 outlines a grating with two diffracted orders, $m = 0$ and $m = 1$.

The solution of the grating equation with $m = 0$ corresponds to specular diffraction and is always present. In this case the diffraction angle equals the incident angle with opposite sign. The ratio λ/d_g determines the integer values of m that result in real-valued diffraction angles. For non-zero diffraction order $m \neq 0$, the diffraction angle β_m depends on the frequency, which is known as angular dispersion. As a result, the path length through the compressor depends on the frequency of the incident beam. By selecting the grating period (d_g) carefully and positioning the individual gratings very precisely, it is possible to make all frequency components exit the compressor simultaneously, thereby forming an output pulse of very short duration and high peak power.

The grating equation gives an accurate description of the kinematics of the propagated beam under ideal conditions, but does not predict the amplitude or phase of the

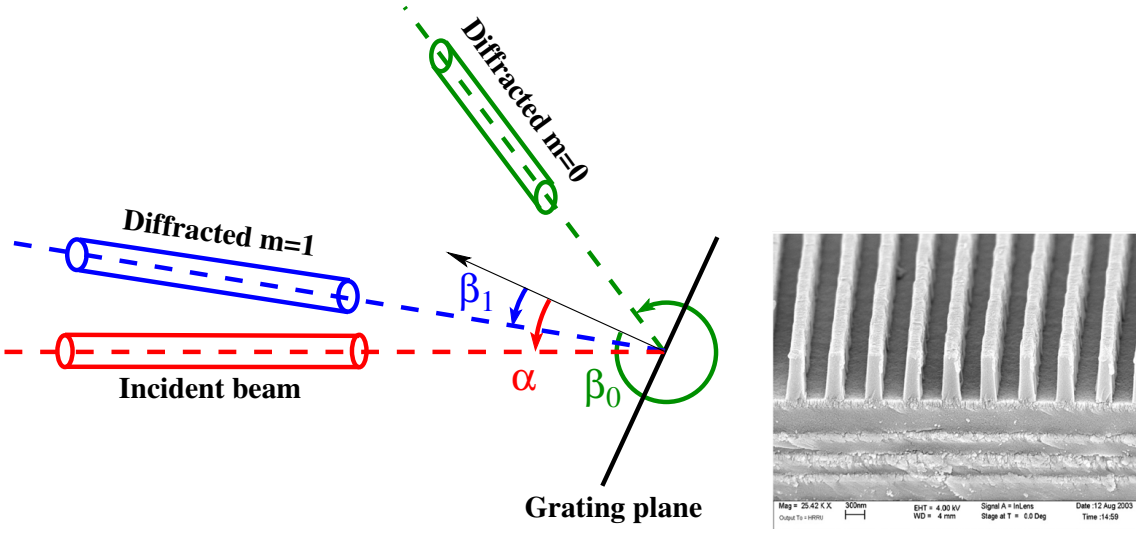

Figure 1: Incident and diffraction angles are measured counter clock-wise from the normal of the grating plane (left). Close-up of a grating surface [4] (right).

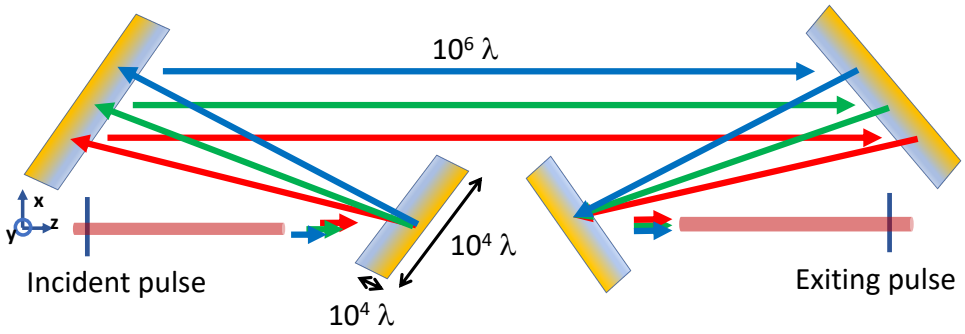

Figure 2: The incident laser pulse is chirped in time and contains a continuous spectrum of frequencies. The diffraction angle in the gratings depends on the wavelength, which depends on the frequency. Thus, the path length through the compressor is frequency dependent. This allows the higher frequencies (blue) to catch up with the lower frequencies (red) such that all frequencies exit almost simultaneously.

beam [16]. Moreover, to accurately model a realistic compressor, it is essential to compute the beam propagation and diffractions under non-ideal conditions. Such conditions occur for various reasons, for example, the grating lines in a real manufactured grating are never perfectly parallel, with perfectly uniform spacing, or uniform line-profile. Furthermore, a perfect compressor is designed for a particular angle of incidence and distance between the gratings, and the grating lines on all gratings are also assumed to be parallel. In reality, the gratings are not perfectly positioned and the grating lines might not be perfectly parallel. Secondly, heating from the laser might cause the grating to deform slightly [1]. Thirdly, when experiments are made in near vacuum conditions, gratings may deform under vacuum loading [12]. All these geometrical perturbations are very small, but the accuracy requirements are very stringent [17]. Some geometrical imperfections can lead to pre-pulses ahead of the main pulse [11]. Even a pre-pulse with a very small amplitude could potentially invalidate a modern high-power laser experiment.

This paper presents a numerical technique, based on solving Maxwell's equations, for simulating the propagation of a laser pulse through a grating compressor with metallic gratings. To outline the proposed technique we assume the compressor consists four gratings, but this is not a restriction of our approach. The incident pulse is first Fourier decomposed into a number of discrete frequency components, where each frequency corresponds to a monochromatic laser beam. For each frequency, the incident beam impinges on the first grating where it is diffracted towards the second grating. The diffracted beam from the first grating becomes the incident beam for the second grating, and so on, until the fourth grating is reached. The fourth grating diffracts the beam towards an observation plane, where the electric field is evaluated for that frequency. The procedure is repeated for all frequencies after which the electric field on the observation plane can be inverse Fourier transformed to obtain the electric field in the time domain. This electric field represents the outgoing laser pulse.

The problem is computationally very challenging because of the disparate length scales that are present. The wavelength of infrared light and the grating line-spacing are both on order of 10^{-6} meters. The size of the gratings are on the order of 10^{-2} to 10^{-1} meters, and the distance between gratings can be on the order of 1 meter. A second order accurate numerical discretization of the surface current on the grating requires about 20 degrees of freedom per wavelength to give reasonable accuracy. This leads to an order of 10^5 to 10^6 degrees of freedom along each side of each grating, which means that there will be of the order 10^{10} to 10^{12} degrees of freedom over the surface of each grating.

Our numerical technique for propagating the beams through the compressor is based on an integral representation of the electric or magnetic fields in terms of the surface current. The surface current satisfies the electric field integral equation (EFIE). After discretization using a finite element method, the integral equation becomes a complex-valued linear system with a dense matrix, which can be solved iteratively using, e.g., the GMRES method. Our first major contribution is the implementation of a multi-level fast multipole algorithm (MLFMA) for accelerating the evaluation of the matrix-vector products during the iterative solution procedure. Due to an inherent numerical instability in the multipole expansion, a substantial part of the dense matrix can not be handled by the MLFMA and must be stored in memory. The memory requirement grows with the

problem size and limit the applicability of the EFIE approach to gratings of size 0.1 mm by 0.1 mm.

Fortunately, we find that the physical optics (PO) approximation [3] of the surface current can provide an accurate representation of the electric and magnetic fields of the diffracted beam, particularly if the fields are scaled by a complex coefficient that only depends on the angle of incidence. With the PO approximation, the surface current follows directly from the incident magnetic field. Thus, the remaining computational challenge is to evaluate the integral representation of the magnetic field on a grating surface, due to the surface current on the preceding grating. For this purpose, we use a multi-level directional Chebyshev interpolation technique. Our second major contribution is the analysis of the accuracy of this technique and the implementation of the method in a parallel, distributed memory code called **js2js**. Based on this code, we are able to simulate a compressor with gratings of size 6 mm by 3 mm, using 64 nodes of a modern Linux cluster.

Compared to previous semi-analytical simulation techniques based on lumped optical element approximations of each grating [8], the proposed method allows arbitrary geometric perturbations of the grating line-profile to be analyzed by directly calculating the resulting electric field in the outgoing beam.

The remainder of the paper is organized as follows. The governing equations are presented in Section 2. The incident laser pulse is specified in the time domain. In Section 3 we describe how the pulse is first approximated by a periodic function in time and then Fourier decomposed into a discrete number of frequencies. Each frequency corresponds to a monochromatic laser beam that can be propagated through the compressor. This section also presents the analytical Gaussian beam solution of the paraxial wave equation. Sections 4 presents a fast multipole method for solving the electric field integral equation. We also compare the accuracy of the physical optics approximation of the surface current. In Section 5, we present a directional Chebyshev interpolation scheme for evaluating the diffracted field on the next grating, or on an observation plane. In Section 6 we first tune the parameters in the directional Chebyshev method followed by a scaling study of the computational cost on a distributed memory parallel computer. A detailed simulation of a symmetric compressor is presented in Section 7. Conclusions are given in Section 8.

2 Governing equations

The propagation of light is modeled by Maxwell's equations in the frequency domain.[1] In the absence of sources and currents, the electric ($\mathbf{E}$) and magnetic ($\mathbf{H}$) fields are governed by

$$i\omega\epsilon\mathbf{E} = \nabla \times \mathbf{H} \tag{2}$$

$$i\omega\mu\mathbf{H} = -\nabla \times \mathbf{E}, \tag{3}$$

where ω is the angular frequency, ϵ is the permittivity, and μ is the permeability of the medium. The laser pulse propagates in air or vacuum between the diffraction gratings,

[1] We use the $\exp(i\omega t)$ sign convention in the Fourier transform, see Section 3.

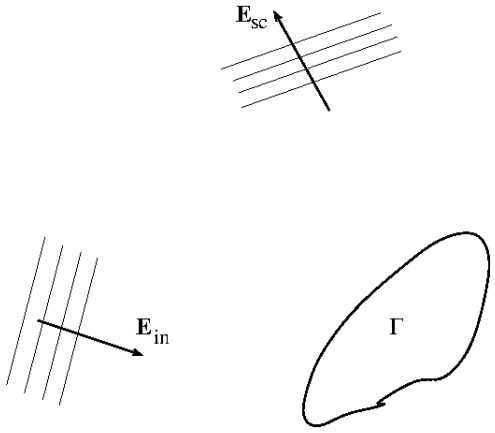

Figure 3: Scattering of an electric field from an object.

and hence, the permittivity and permeability are assumed to be constants.

We consider the configuration in Figure 3, where an incident electric field, $\mathbf{E}_{in}$, is impinging on an object, or a surface, denoted by Γ. The surface Γ is assumed a perfect conductor, implying the boundary conditions

$$\hat{\mathbf{n}} \times \mathbf{E} = \mathbf{0} \quad \mathbf{x} \in \Gamma, \tag{4}$$

$$\hat{\mathbf{n}} \cdot \mathbf{H} = 0 \quad \mathbf{x} \in \Gamma, \tag{5}$$

where $\hat{\mathbf{n}}$ denotes the unit surface normal. The total electric field $\mathbf{E} = \mathbf{E}_{in} + \mathbf{E}_{sc}$, solves (2) and (3) on the domain outside Γ, with boundary condition (4). The scattered field, $\mathbf{E}_{sc}$, is defined by $\mathbf{E} - \mathbf{E}_{in}$. Furthermore, the incident field, $\mathbf{E}_{in}$, is assumed to be a solution of Maxwell's equations in free space.

Equations (2) and (3) can be used to derive a boundary integral representation of the scattered field [3],

$$\mathbf{E}_{sc}(\mathbf{x}) = -i\omega\mu \left(\int_\Gamma \mathbf{J}^s(\mathbf{y}) G(\mathbf{x},\mathbf{y})\, dS_\mathbf{y} + \frac{1}{k^2} \nabla_\mathbf{x} \int_\Gamma \nabla_s \cdot (\mathbf{J}^s(\mathbf{y})) G(\mathbf{x},\mathbf{y})\, dS_\mathbf{y} \right) \tag{6}$$

for the scattered field, $\mathbf{E}_{sc}$, at the point $\mathbf{x}$ exterior to Γ. The surface current $\mathbf{J}^s$ is equal to $\hat{\mathbf{n}} \times \mathbf{H}$, see [23]. The Green's function, G, is the fundamental solution of Helmholtz' equation,

$$G(\mathbf{x},\mathbf{y}) = \frac{e^{-ik|\mathbf{x}-\mathbf{y}|}}{4\pi|\mathbf{x}-\mathbf{y}|}. \tag{7}$$

The surface divergence of a tangential vector field $\mathbf{f}$ is denoted by $\nabla_s \cdot \mathbf{f}$. The notation $\nabla_\mathbf{x}$ denotes the gradient with respect to $\mathbf{x}$.

The scattered magnetic field follows from Faraday's law (3),

$$\mathbf{H}_{sc}(\mathbf{x}) = \frac{-1}{i\omega\mu} \left(\nabla \times \mathbf{E}_{sc}(\mathbf{x}) \right).$$

Because $\nabla \times \nabla\phi(\mathbf{x}) = \mathbf{0}$ for all smooth functions $\phi(\mathbf{x})$, the contribution from the second integral in (6) is identically zero when $\mathbf{x} \notin \Gamma$, leading to

$$\mathbf{H}_{sc}(\mathbf{x}) = \nabla_{\mathbf{x}} \times \int_\Gamma \mathbf{J}^s(\mathbf{y}) G(\mathbf{x},\mathbf{y})\, dS_{\mathbf{y}} = \int_\Gamma \mathbf{J}^s(\mathbf{y}) \times \nabla_{\mathbf{y}} G(\mathbf{x},\mathbf{y})\, dS_{\mathbf{y}}, \quad \mathbf{x} \notin \Gamma, \tag{8}$$

because $\mathbf{J}^s(\mathbf{y})$ does not depend on $\mathbf{x}$ and $\nabla_{\mathbf{x}} G = -\nabla_{\mathbf{y}} G$.

The surface current on Γ is not explicitly known when only the incident fields are given. We will consider two different methods to compute $\mathbf{J}^s$.

The first method is to solve the electric field integral equation (EFIE). The EFIE is derived by cross multiplying (6) by $\hat{\mathbf{n}}$ and specializing $\mathbf{x}$ to the surface, Γ. The boundary condition (4) is used to write the left hand side in terms of the given incident field, and results in the EFIE,

$$\hat{\mathbf{n}} \times \mathbf{E}_{in}(\mathbf{x}) = i\omega\mu\hat{\mathbf{n}} \times \left(\int_\Gamma \mathbf{J}^s(\mathbf{y}) G(\mathbf{x},\mathbf{y})\, dS_{\mathbf{y}} + \frac{1}{k^2} \nabla_{\mathbf{x}} \int_\Gamma \nabla_s \cdot (\mathbf{J}^s(\mathbf{y})) G(\mathbf{x},\mathbf{y})\, dS_{\mathbf{y}} \right), \quad \mathbf{x} \in \Gamma \tag{9}$$

which can be solved for $\mathbf{J}^s$. Note that the integrand is singular since both $\mathbf{x}$ and $\mathbf{y}$ are located on Γ.

Secondly, an alternative to solving the EFIE is to use the Physical Optics (PO) approximation,

$$\mathbf{J}^s(\mathbf{x}) = 2\hat{\mathbf{n}}(\mathbf{x}) \times \mathbf{H}_{in}(\mathbf{x}), \quad \mathbf{x} \in \Gamma \tag{10}$$

to directly evaluate the surface current from the incident field. This approach is computationally very efficient, but introduces a modeling error. The PO approximation is exact when Γ is a plane of infinite extent, see [3].

3 Decomposing a laser pulse into laser beams

The time-dependent electric field, $\mathcal{E}(\mathbf{x},t)$, and its Fourier transform, $\mathbf{E}(\mathbf{x},\omega)$, are related by

$$\mathcal{E}(\mathbf{x},t) = \frac{1}{2\pi} \int_{-\infty}^{\infty} \mathbf{E}(\mathbf{x},\omega) e^{i\omega t}\, d\omega, \tag{11}$$

$$\mathbf{E}(\mathbf{x},\omega) = \int_{-\infty}^{\infty} \mathcal{E}(\mathbf{x},t) e^{-i\omega t}\, dt. \tag{12}$$

Here, ω is the angular frequency. While the frequency-dependent field $\mathbf{E}(\mathbf{x},\omega)$ is complex-valued, the time-dependent field $\mathcal{E}(\mathbf{x},t)$ is real-valued. As a result, $\mathbf{E}$ must satisfy the symmetry condition

$$\mathbf{E}(\mathbf{x},-\omega) = \bar{\mathbf{E}}(\mathbf{x},\omega),$$

where $\bar{\mathbf{E}}$ denotes the complex conjugate of $\mathbf{E}$. The Fourier transform of the magnetic field, $\mathbf{H}(\mathbf{x},\omega)$, satisfies the same symmetry condition. In the usual way we can therefore restrict the analysis of the Fourier transformed problem to $\omega > 0$. However, it is sometimes

convenient to represent time-dependent functions in complex arithmetic. This is done with the implicit understanding that the real part of the complex function represents the physical quantity under consideration.

3.1 Chirped pulses

We describe the incident field in Cartesian coordinates (x, y, z) relative to a fixed "lab" frame, where (x, z)-directions are in the horizontal plane, the y-direction is vertical, and the incident field propagates in the positive z-direction. Let the incident time-dependent electric field on the $z = 0$ plane be centered at the origin of the (x, y)-plane and satisfy

$$\mathcal{E}_{in}(x, y, 0, t) =: \boldsymbol{\eta}(x, y, t). \tag{13}$$

In general, the time-dependence of the incident field may vary over the $z = 0$ plane. In the following it is specified at the origin and is assumed to be the same for all three components of $\boldsymbol{\eta}$,

$$\boldsymbol{\eta}(0, 0, t) = g(t) \begin{pmatrix} \eta_{x0} \\ \eta_{y0} \\ \eta_{z0} \end{pmatrix},$$

for some constants η_{x0}, η_{y0}, and η_{z0}.

We consider the case when the time function of the incident pulse is the chirped Gaussian function,

$$g(t) = p(t)e^{i\omega_c t}, \quad p(t) = \exp\left(\frac{-(1 + ia)t^2}{\tau^2}\right). \tag{14}$$

Here, $\omega_c > 0$ is the angular frequency of the carrier wave, also known as the center frequency. The function $p(t)$ is the envelope function where a and $\tau > 0$ are real constants.

By introducing a phase function $\phi(t)$, we can write the incident time function in (14) as

$$g(t) = \exp\left(\frac{-t^2}{\tau^2}\right) \exp(i\phi(t)), \quad \phi(t) = \omega_c t - at^2/\tau^2. \tag{15}$$

The phase function is quadratic in time and the instantaneous frequency, $\phi'(t) = \omega_c - 2at/\tau^2$, varies linearly in time. Note that $\phi'(t)$ increases with time when $a < 0$. In this case the pulse is said to have up-chirp, which is appropriate for the compressor application. See Figure 4 for an example of the incident time function $g(t)$.

The Fourier transform of $g(t)$ satisfies

$$\widehat{g}(\omega) = \widehat{p}(\omega - \omega_c), \tag{16}$$

where the Fourier transform of $p(t)$ is given by

$$\widehat{p}(\Omega) = \sqrt{\frac{\pi\tau^2}{1 + ia}} \exp\left(\frac{-\Omega^2\tau^2}{4(1 + ia)}\right), \quad \Omega = \omega - \omega_c. \tag{17}$$

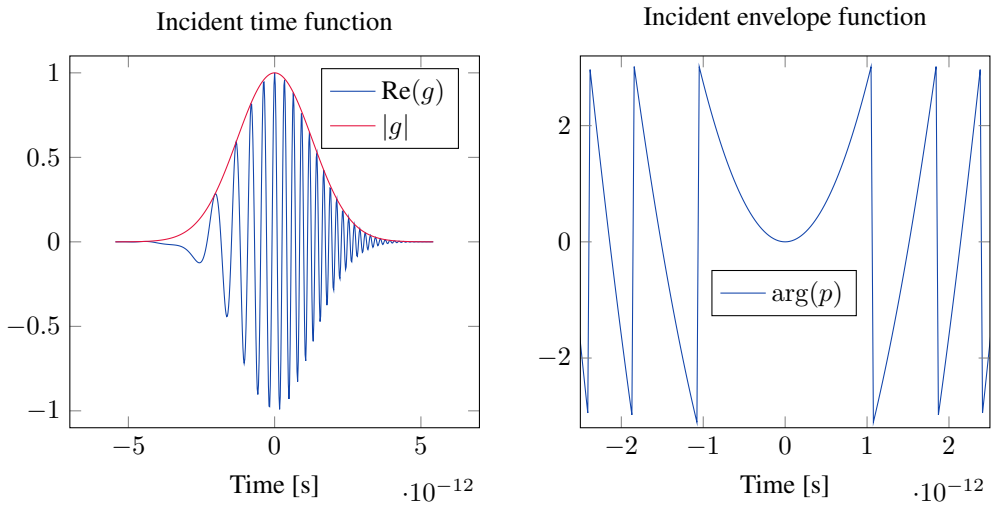

Figure 4: Left: incident time function, $g(t)$, with $\omega_c = 1.7888 \cdot 10^{13}$ rad/s. The actual value of ω_c is 100 times larger. Right: the phase of the incident envelope function, $\tan^{-1}(\mathrm{Im}\,(p)/\mathrm{Re}\,(p))$. Here $\tan^{-1}(\theta) \in (-\pi, \pi]$.

In Figure 5 we show the Fourier transform of the envelope function, $\widehat{p}(\Omega)$. When approximating $\widehat{p}(t)$ by a discrete Fourier transform, we must first truncate the tails of $p(t)$ and approximate it by a periodic function with sufficiently large period T. That period gives the frequency resolution, $\Delta\Omega = 1/T$, for the discrete Fourier transform. A sufficient number of discrete frequencies must then be used to resolve the tails of $\widehat{p}(\Omega)$.

3.2 Paraxial approximation

We are interested in beam-like incident fields, where the beam propagates in the positive z-direction. In this section, we drop the subscript on the incident field. Maxwell's equations in the frequency domain govern the electric field,

$$k^2\mathbf{E} = \nabla \times \nabla \times \mathbf{E}, \quad k = \frac{\omega}{c}, \quad z > 0, \tag{18}$$

$$\mathbf{E}(x, y, 0, \omega) = \mathbf{h}(x, y, \omega), \quad z = 0. \tag{19}$$

Here $\mathbf{h}$ is the Fourier transform (with respect to time) of the boundary data $\boldsymbol{\eta}(x, y, t)$ in (13).

An asymptotic solution of (18)-(19) can be found through the ansatz (see e.g. Lax et al. [15]),

$$\mathbf{E}(x, y, z, \omega) = \boldsymbol{\Psi}(x, y, z, \omega)e^{-ikz}, \quad z > 0, \tag{20}$$

$$\boldsymbol{\Psi}(x, y, 0, \omega) = \mathbf{h}(x, y, \omega). \tag{21}$$

Let the characteristic length scale of the beam be w_0 in the (transverse) (x, y)-directions. The diffraction (Rayleigh) length of a Gaussian beam,

$$z_R = kw_0^2/2,$$

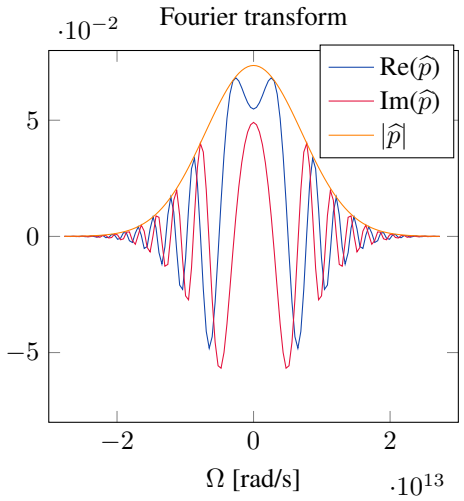

Figure 5: The Fourier transform of the envelope function, $\widehat{p}(\Omega)$.

provides a length scale in the (longitudinal) z-direction. We seek solutions where $w_0 \ll z_R$. Let the Cartesian components if the incident field be $\mathbf{E} = \left(E^{(x)}, E^{(y)}, E^{(z)}\right)^T$ and $\mathbf{\Psi} = \left(\psi^{(x)}, \psi^{(y)}, \psi^{(z)}\right)^T$. By making an asymptotic expansion in $\varepsilon := w_0/z_R \ll 1$, Lax [15] showed that to leading order in ε, the vector wave equation (18) simplifies to decoupled scalar Schrödinger equations for each of the transverse components,

$$2ik\partial_z\psi = (\partial_x^2 + \partial_y^2)\psi, \quad \psi = \psi^{(x)} \text{ or } \psi = \psi^{(y)}. \tag{22}$$

The longitudinal component, which often is neglected because it is a factor ε smaller than the transverse components, satisfies

$$ik\psi^{(z)} = \partial_x\psi^{(x)} + \partial_y\psi^{(y)}. \tag{23}$$

The Schrödinger equation can in some cases be solved analytically. The fundamental solution is the Gaussian TEM_{00} mode. It can be expressed in polar coordinates (r, θ, z),

$$x = r\cos(\theta), \quad y = r\sin(\theta), \quad \rho = \frac{r}{w_0}, \quad \zeta = \frac{z - z_0}{z_R},$$

in terms of the envelope function,

$$\psi_{00}(\rho, \zeta) = \frac{1}{1 - i\zeta}\, e^{-\rho^2(1+i\zeta)/(1+\zeta^2)}. \tag{24}$$

The corresponding electric field satisfies

$$E^{(x)}(r, z) = A_x\psi_{00}\left(\frac{r}{w_0}, \frac{z - z_0}{z_R}\right) e^{-ikz}, \tag{25}$$

$$E^{(y)}(r, z) = A_y\psi_{00}\left(\frac{r}{w_0}, \frac{z - z_0}{z_R}\right) e^{-ikz}, \tag{26}$$

$$E^{(z)}(r, \theta, z) = \frac{i}{z_R - i(z - z_0)}\left(r\cos(\theta)E^{(x)}(r, z) + r\sin(\theta)E^{(y)}(r, z)\right), \tag{27}$$

where A_x and A_y are constants. We note that the longitudinal component, $E^{(z)} = \mathcal{O}(\varepsilon)$, and the divergence of the electric field, $\nabla \cdot \mathbf{E} = \mathcal{O}(\varepsilon/w_0)$.

The corresponding magnetic field follows from (3). Because $w_0/z_R \ll 1$, to leading order in ε we get

$$\sqrt{\frac{\mu}{\epsilon}} H^{(x)}(r,z) = -E^{(y)}(r,z), \tag{28}$$

$$\sqrt{\frac{\mu}{\epsilon}} H^{(y)}(r,z) = E^{(x)}(r,z), \tag{29}$$

$$H^{(z)}(r,\theta,z) = \frac{i}{z_R - i(z-z_0)} \left(r\cos(\theta) H^{(x)}(r,z) + r\sin(\theta) H^{(y)}(r,z) \right). \tag{30}$$

In the above expressions, note that ϵ is the permittivity of the medium, which is different from the expansion coefficient $\varepsilon = w_0/z_R$. Similar to the electric field, the longitudinal component of the magnetic field is of the order $\mathcal{O}(\varepsilon)$.

Even though (25)-(27) and (28)-(30) only solves Maxwell's equations in the limit as $\varepsilon \to 0$, these formulas provide a very good approximation for finite values of $0 < \varepsilon \ll 1$.

4 Integral equation formulation

For either the EFIE or the PO, the scattered electric field can be evaluated at any point, $\mathbf{x}$, by (6) using the computed surface current. Note that (6) is not a singular integral when the scattered field is computed away from Γ.

The scattered $\mathbf{E}_{sc}$ is needed to compute the pulse at the exit of the four grating compressor. The scattered field is also needed when the beam is propagated from one grating to another. The EFIE uses $\mathbf{E}_{sc}$ from one grating as the incident field, $\mathbf{E}_{in}$, to compute the surface current on the next grating. When the PO is used to approximate the surface current, the scattered magnetic field $\mathbf{H}_{sc}$ from one grating is used as the incident magnetic field, $\mathbf{H}_{in}$, on the next grating. The scattered magnetic field is follows from the integral (8).

4.1 Discretization of the EFIE

The EFIE is discretized by a finite element method (FEM) on a quadrilateral mesh using Raviart-Thomas (rooftop) basis functions. This is a standard method that have been used extensively for computation of electromagnetic scattering, starting with the work by Rao etal. [20]. This section summarizes the most important features. For more details, see Chapter 6 of [27], or [13]. The discretization is also known as method of moments (MoM) in the electromagnetics literature.

The approximation of the surface current is sought as a linear combination of basis functions,

$$\mathbf{J}^s(\mathbf{y}) = \sum_{q=1}^{N_e} j_q \mathbf{f}_q(\mathbf{y}), \tag{31}$$

where the rooftop functions $\mathbf{f}_q$ are real valued, divergence conforming, and tangential to Γ. Each rooftop function is associated with an edge of the quadrilateral grid. The edges of the grid are enumerated by $q = 1, \ldots, N_e$, where N_e denotes the total number of edges. The basis functions have support on two quadrilaterals, see Fig. 6. The expansion coefficients, j_q, are complex valued scalars.

Quadrilateral elements makes it straightforward to use different resolutions in the directions along and transverse to the grating lines. The surface current usually have more structure in the line-transverse direction.

The Galerkin approximation, obtained by inserting (31) into (9) and testing with the functions $\mathbf{n} \times \mathbf{f}_p$, leads to a linear system of equations,

$$Z\mathbf{j} = \mathbf{b}, \tag{32}$$

for $\mathbf{j}$, the vector of coefficients j_q. The scalar product is defined over Γ,

$$(\mathbf{u}, \mathbf{v}) = \int_{\mathbf{x}\in\Gamma} \mathbf{u}(\mathbf{x})^H \mathbf{v}(\mathbf{x})\, dS_{\mathbf{x}},$$

where the superscript H denotes transpose and complex conjugation.

The matrix elements are

$$Z_{pq} = i\omega\mu \left(\int_{\mathbf{x}\in\Gamma} \int_{\mathbf{y}\in\Gamma} \mathbf{f}_p(\mathbf{x})^H \mathbf{f}_q(\mathbf{y}) G(\mathbf{x},\mathbf{y})\, dS_{\mathbf{y}}\, dS_{\mathbf{x}} \right.$$
$$\left. -\frac{1}{k^2} \int_{\mathbf{x}\in\Gamma} \int_{\mathbf{y}\in\Gamma} \nabla_s\cdot(\mathbf{f}_p(\mathbf{x}))\nabla_s\cdot(\mathbf{f}_q(\mathbf{y})) G(\mathbf{x},\mathbf{y})\, dS_{\mathbf{y}}\, dS_{\mathbf{x}} \right) \tag{33}$$

and the right hand side

$$b_p = (\mathbf{f}_p, \mathbf{E}_{in})_\Gamma = \int_{\mathbf{x}\in\Gamma} \mathbf{f}_p(\mathbf{x})^H \mathbf{E}_{in}(\mathbf{x})\, dS_{\mathbf{x}} \tag{34}$$

The derivation of (33) and (34) uses the identity

$$(\mathbf{n} \times \mathbf{a}) \cdot (\mathbf{n} \times \mathbf{b}) = \mathbf{a} \cdot \mathbf{b}, \tag{35}$$

which holds if one, or both, of $\mathbf{a}$ and $\mathbf{b}$ are tangential to Γ. Furthermore, the partial integration formula

$$\int_\Gamma \mathbf{f}_p^T \nabla_s \phi\, dS = -\int_\Gamma \phi \nabla_s\cdot\mathbf{f}_p\, dS$$

is used on the second term in (33) to remove the derivatives on the Helmholtz kernel. The surface gradient of ϕ is denoted by $\nabla_s\phi$.

An iterative solver from the PetSc library is used to solve (32). The equation is preconditioned by the Calderon preconditioner using a dual discretization, see [5, 2, 7].

For practical evaluation of Z and b, a bilinear coordinate mapping is defined on each quadrilateral on the grid, transforming each quadrilateral to the unit square. Specifically, for the configuration shown in Fig. 6, the mapping is

$$\mathbf{Y}(\xi,\eta) = \begin{cases} -\xi(1-\eta)\mathbf{y}_F - \xi\eta\mathbf{y}_E + (1+\xi)(1-\eta)\mathbf{y}_A + (1+\xi)\eta\mathbf{y}_D, & -1 \le \xi < 0, \\ (1-\xi)(1-\eta)\mathbf{y}_A + (1-\xi)\eta\mathbf{y}_D + \xi(1-\eta)\mathbf{y}_B + \xi\eta\mathbf{y}_C, & 0 < \xi \le 1, \end{cases} \tag{36}$$

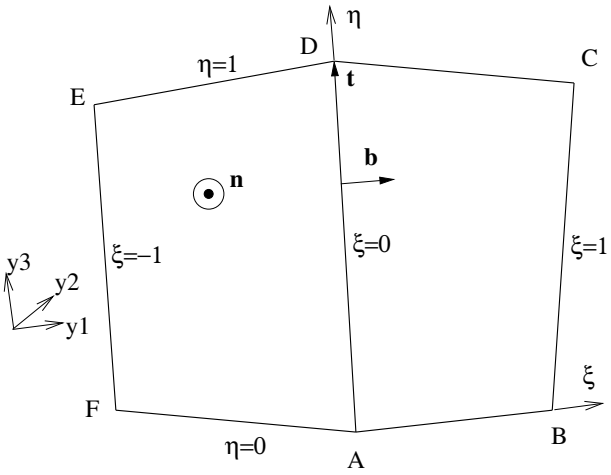

Figure 6: The basis function corresponding to the edge connecting vertices A and D, with the surface normal $\hat{\mathbf{n}}$ directed towards the viewer. The bi-normal $\mathbf{b} = (\mathbf{y}_D - \mathbf{y}_A) \times \hat{\mathbf{n}}$ is tangential to Γ and normal to AD. The basis function has support over the two adjacent faces (A, B, C, D) and (A, D, E, F). It is identically zero everywhere else.

for $0 \le \eta \le 1$. The rooftop basis function associated with edge AD in Fig. 6 is defined by

$$\mathbf{f}(\xi,\eta) = \begin{cases} \frac{1}{\sqrt{g}}(1+\xi)\partial_\xi \mathbf{Y}, & 0 \le \eta \le 1, \ -1 \le \xi < 0, \\ \frac{1}{\sqrt{g}}(1-\xi)\partial_\xi \mathbf{Y}, & 0 \le \eta \le 1, \quad 0 < \xi \le 1, \\ 0, & \text{otherwise}, \end{cases} \tag{37}$$

where $\partial_\xi \mathbf{Y}$ denotes $\partial \mathbf{Y}/\partial \xi$. The unit surface normal and the surface Jacobian are defined by

$$\hat{\mathbf{n}} = \frac{\partial_\xi \mathbf{Y} \times \partial_\eta \mathbf{Y}}{|\partial_\xi \mathbf{Y} \times \partial_\eta \mathbf{Y}|}, \quad \sqrt{g} = \hat{\mathbf{n}} \cdot (\partial_\xi \mathbf{Y} \times \partial_\eta \mathbf{Y}) = |\partial_\xi \mathbf{Y} \times \partial_\eta \mathbf{Y}|,$$

where $\partial_\eta \mathbf{Y}$ denotes $\partial \mathbf{Y}/\partial \eta$. The surface divergence of the basis functions is

$$\nabla_s \cdot \mathbf{f}(\xi,\eta) = \begin{cases} \frac{+1}{\sqrt{g}}, & -1 \le \xi < 0, \\ \frac{-1}{\sqrt{g}}, & 0 < \xi \le 1 \\ 0, & \text{otherwise}. \end{cases} \tag{38}$$

for $0 \le \eta \le 1$. The functions $\mathbf{f}_q$ are discontinuous across the edges, but their edge-normals tangential to Γ are continuous. It holds that

$$\mathbf{b} \cdot \mathbf{f}_q(0,\eta) = 1 \quad 0 \le \eta \le 1, \tag{39}$$

for the bi-normal

$$\mathbf{b} = \partial_\eta \mathbf{Y}/(0,\eta) \times \hat{\mathbf{n}} = (\mathbf{y}_D - \mathbf{y}_A) \times \hat{\mathbf{n}}. \tag{40}$$

At edges EF and BC of the basis function support, $\mathbf{f} = \mathbf{f}(\pm 1, \eta) = \mathbf{0}$ so that the bi-normal components are zero. At edges AB, CD, DE, EF, FA, the bi-normal components are $(\partial_\xi \mathbf{Y} \times \hat{\mathbf{n}}) \cdot \mathbf{f}$, which by (37) is zero.

The coordinate mapping (36) transforms the integrals in (33) and (34) to sums of integrals over unit square elements in coordinates (ξ, η). Each term in the sum is evaluated by Gaussian quadrature over a small number quadrature points. Special numerical quadrature is used on the elements that have singularies, i.e., when $\mathbf{x} = \mathbf{y}$ in the integrand $G(\mathbf{x}, \mathbf{y})$, see [9].

Construction and mapping of basis functions on triangles and quadrilaterals to arbitrary order of accuracy are given in [6].

4.2 Discretization of the PO approximation and evaluation of the scattered fields

When the PO approximation is used, the surface current is assumed to be of the form (31) on the quadrilateral FEM grid. Keeping the same form of approximation faciliates modular software, with interchangeable modules for PO or EFIE. The PO solver uses the formula

$$j_e = \mathbf{b}_e \cdot \mathbf{J}^s(\hat{\mathbf{y}}_e), \tag{41}$$

to determine the coefficients in (31), for any given surface current $\mathbf{J}^s(\mathbf{y})$. Here $\mathbf{b}_e$ is the bi-normal of edge e, given by (40), and $\hat{\mathbf{y}}_e$ is the mid-point of edge e. If the surface current is obtained from a magnetic field, $\mathbf{J}^s = 2\hat{\mathbf{n}} \times \mathbf{H}$, then (41) simplifies to

$$j_e = \mathbf{b}_e \cdot \mathbf{J}^s(\hat{\mathbf{y}}_e) = 2(\partial_\eta \mathbf{Y} \times \hat{\mathbf{n}}) \cdot (\hat{\mathbf{n}} \times \mathbf{H}(\hat{\mathbf{y}}_e) = -2\partial_\eta \mathbf{Y} \cdot \mathbf{H}(\hat{\mathbf{y}}_e).$$

by use of (35). Formula (41) is motivated by

$$\mathbf{b}_e(\mathbf{y}_e) \cdot \sum_{q=1}^{N_e} j_q \mathbf{f}_q(\mathbf{y}_e) = \mathbf{b}_e(\mathbf{y}_e) \cdot \mathbf{f}(\mathbf{y}_e) j_e = j_e,$$

which follows from (39) and the fact that $\mathbf{b}_e(\mathbf{y}_e) \cdot \mathbf{f}_q(\mathbf{y}_e) = 0$ for $e \neq q$. Here $\mathbf{y}_e$ is any point on edge e.

Computation of $\mathbf{E}_{sc}$ and $\mathbf{H}_{sc}$ generated by a given surface current, requires the discretization of the integrals (6) and (8). The first integral of (6) becomes when (31) is inserted,

$$\int_\Gamma \sum_{e=1}^{N_e} j_e \mathbf{f}_e(\mathbf{y}) G(\mathbf{x}, \mathbf{y})\, dS_{\mathbf{y}}. \tag{42}$$

Here $\mathbf{x}$ is assumed to be a point on the observation screen, away from Γ. When the integral over Γ is decomposed into a sum over each separate quadrilateral, and the coordinate mapping (36) is transforming the integral on each quadrilateral, the integral (42) becomes

$$\sum_{q=1}^{N_Q} \int_0^1 \int_0^1 \mathbf{Z}_q(\mathbf{Y}_q(\xi, \eta)) G(\mathbf{x}, \mathbf{Y}_q(\xi, \eta))\, d\xi d\eta, \tag{43}$$

where $q = 1, \ldots, N_Q$ enumerates the quadrilaterals of the grid. As indicated by Fig. 7, on each quadrilateral there are four basis functions, associated with its four edges, that are

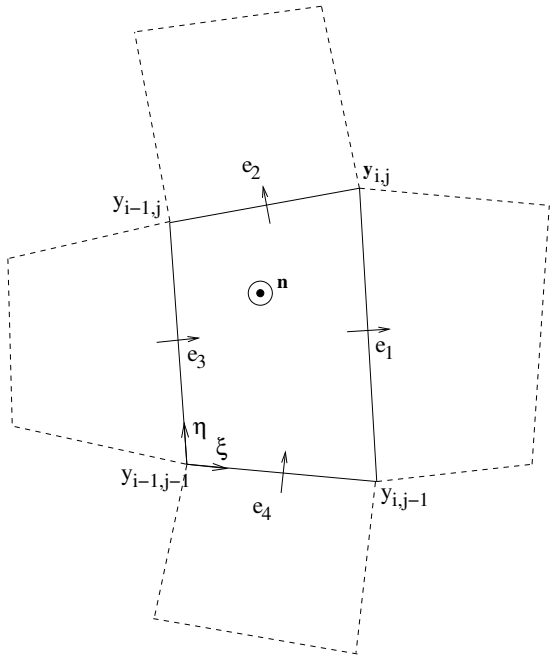

Figure 7: The surface current on each face equals the sum of the contributions from the four basis functions corresponding to the bounding edges. The arrows across the edges indicate the directions of each edge basis function.

non-zero. The quantity $\mathbf{Z}_q$ denotes the contribution from the terms $j_e\mathbf{f}_e$ on quadrilateral q,

$$\mathbf{Z}_q = (j_{e1}\mathbf{f}_{e1}(\mathbf{Y}_q(\xi,\eta)) + j_{e2}\mathbf{f}_{e2}(\mathbf{Y}_q(\xi,\eta)) + j_{e3}\mathbf{f}_{e3}(\mathbf{Y}_q(\xi,\eta)) + j_{e4}\mathbf{f}_{e4}(\mathbf{Y}_q(\xi,\eta)))\sqrt{g_q},$$

where the edges $e_1 \ldots e_4$ denote the four sides of quadrilateral q, as shown in Fig. 7. The surface element $\sqrt{g_q}$ is also factored into the definition of $\mathbf{Z}_q$. By using Gauss-Legendre collocation with 2 points in each direction for (43), the first integral in (6) becomes

$$\sum_{q=1}^{N_Q}\sum_{p=1}^{4} \tilde{w}_p \mathbf{Z}_q(\mathbf{Y}_q(\tilde{\xi}_p,\tilde{\eta}_p))G(\mathbf{x},\mathbf{Y}_q(\tilde{\xi}_p,\tilde{\eta}_p)) = \sum_{q=1}^{N_Q} I_q^{(1)}(\mathbf{x}) \tag{44}$$

where $(\tilde{\xi}_p,\tilde{\eta}_p) \in (-1,1)^2$ are the collocation points and $\tilde{w}_p$ are the collocation weights. The last equality in (44) is obtained by denoting

$$I_q^{(1)}(\mathbf{x}) = \sum_{p=1}^{4} \tilde{w}_p \mathbf{Z}_q(\tilde{\xi}_p,\tilde{\eta}_p)G(\mathbf{x},\mathbf{Y}_q(\tilde{\xi}_p,\tilde{\eta}_p)). \tag{45}$$

For discretization of the the second term in (6), the gradient is first taken inside the integral, and the relation $\nabla_{\mathbf{x}}G = -\nabla_{\mathbf{y}}G$ is used. The integral is written as a sum over quadrilaterals and transformed to local coordinates, in the same way as in the derivation

of (43). The integrand over each face contains a product of the divergence of the surface current and the surface Jacobian $\sqrt{g}$. Thanks to the relation (38), this product is constant

$$j_{e_1} + j_{e_2} - j_{e_3} - j_{e_4}$$

and the integrand reduces to a constant times the gradient of the Green's function. The integral can be adequately approximated by the midpoint rule,

$$I_q^{(2)}(\mathbf{x}) = (j_{e_1} + j_{e_2} - j_{e_3} - j_{e_4})\, D_y G(\mathbf{x}, \tilde{\mathbf{y}}_q), \tag{46}$$

where the coordinate of the midpoint of face q is $\tilde{\mathbf{y}}_q = \mathbf{Y}_q(\frac{1}{2}, \frac{1}{2})$. The gradient of G is approximated by the numerical differentiation

$$\nabla_{\mathbf{y}} G(\mathbf{x}, \mathbf{y}) \approx D_y G(\mathbf{x}, \mathbf{y}) = \frac{1}{2\delta} \begin{pmatrix} G(\mathbf{x}, \mathbf{y} + \delta \mathbf{e}_x) - G(\mathbf{x}, \mathbf{y} - \delta \mathbf{e}_x)) \\ G(\mathbf{x}, \mathbf{y} + \delta \mathbf{e}_y) - G(\mathbf{x}, \mathbf{y} - \delta \mathbf{e}_y)) \\ G(\mathbf{x}, \mathbf{y} + \delta \mathbf{e}_z) - G(\mathbf{x}, \mathbf{y} - \delta \mathbf{e}_z)) \end{pmatrix}, \tag{47}$$

where δ is a small parameter, given the value $10^{-4}\lambda$ in the computations. The wavelength λ here acts as the length scale of the problem. The vectors $\mathbf{e}_x$, $\mathbf{e}_y$, and $\mathbf{e}_z$ are the unit vectors in the x, y, and z-directions respectively. By formula (47), $I_q^{(2)}$ becomes a sum of six terms each requiring one evaluation of the Helmholtz kernel.

The approximation of the scattered field becomes, by the definition (46),

$$\mathbf{E}_{sc}(\mathbf{x}) \approx -i\omega\mu \left(\sum_{q=1}^{N_Q} I_q^{(1)}(\mathbf{x}) - \frac{1}{k^2} \sum_{q=1}^{N_Q} I_q^{(2)}(\mathbf{x}) \right). \tag{48}$$

The integral for the magnetic field (8) is discretized in a similar way, leading to

$$\mathbf{H}_{sc}(\mathbf{x}) \approx \sum_{q=1}^{N_Q} I_q^{(3)}(\mathbf{x}), \tag{49}$$

where the contribution from quadrilateral q is given by

$$I_q^{(3)}(\mathbf{x}) = \sum_{p=1}^{4} \tilde{w}_p \mathbf{Z}_q(\tilde{\xi}_p, \tilde{\eta}_p) \times D_y G(\mathbf{x}, \mathbf{y}_p), \quad \mathbf{y}_p = \mathbf{Y}_q(\tilde{\xi}_p, \tilde{\eta}_p), \tag{50}$$

where (47) is used to evaluate the gradient of G at each collocation point.

4.3 Multilevel fast multipole algorithm

Iterative solution of (32) can become expensive for large problem sizes. Even though only a matrix-vector product $Z\mathbf{j}$ is evaluated for each iteration, the resolution requirements make this into a very costly operation. A direct evaluation $Z\mathbf{j}$ requires $\mathcal{O}(N^2)$ operations, since Z is a full matrix, where N could be on the order of $10^{10} - 10^{12}$. The multilevel

fast multipole algorithm (MLFMA) speeds up the matrix-vector product evaluation, by bringing down the number of operations from $\mathcal{O}(N^2)$ to $\mathcal{O}(N \log N)$. The EFIE solver in this work uses the standard MLFMA, as described, e.g., in [13] or [27].

This section gives a summary of the main features of MLFMA, and points out some practical considerations. The algorithm will not be described in detail.

The MLFMA algorithm uses an expansion of the Helmholtz kernel into lower rank terms,

$$G(\mathbf{x}, \mathbf{y}) \approx \widehat{G}(\mathbf{x}, \mathbf{y}) = \sum_{r=1}^{R} T_{r,L}(\mathbf{x}_m, \mathbf{y}_n) a_r(\mathbf{x} - \mathbf{x}_m) b_r(\mathbf{y} - \mathbf{y}_n). \tag{51}$$

for $\mathbf{x}$ in a neighborhood of $\mathbf{x}_m$ and $\mathbf{y}$ in a neighborhood of $\mathbf{y}_n$. The functions are given by

$$a_r(\mathbf{x}) = e^{-ik\mathbf{x}^T\hat{\mathbf{x}}_r} \quad b_r(\mathbf{y}) = e^{ik\mathbf{y}^T\hat{\mathbf{x}}_r} \quad T_{r,L} = w_r T_L(k|\mathbf{x}_m - \mathbf{y}_n|, \frac{(\mathbf{x}_m - \mathbf{y}_n)^T\hat{\mathbf{x}}_r}{|\mathbf{x}_m - \mathbf{y}_n|})$$

The points $\hat{\mathbf{x}}_r$ are quadrature points on the unit sphere, with quadrature weights w_r. Here, T_L is a multi pole (?) series expansion with L terms. From accuracy considerations, the number of terms in (51) is related to L by $R = 2L^2 + L$.

In MLFMA, the degrees of freedom (edges) are grouped into boxes. The computational domain is covered by a Cartesian grid of square boxes, and each basis function is assigned to one and only one box. Formula (51) is inserted in (33) with $\mathbf{x}_m$ and $\mathbf{y}_n$ as coordinate vectors of the centers of box m and box n respectively.

The matrix-vector product is then evaluated in three steps. First performing a local sum inside each box (essentially terms originating from $b_r(\mathbf{y} - \mathbf{y}_n)$ in (51)), secondly multiplying the result by $T_{r,L}(\mathbf{x}_m, \mathbf{y}_n)$, which can be interpreted as a box to box interaction, and thirdly evaluation of the final result for each degree of freedom locally from information at its box center (terms originating from $a_r(\mathbf{x} - \mathbf{x}_m)$ in (51)), as obtained in step 2.

It can be shown that this can only improve the number of arithmetic operations to become $\mathcal{O}(N^{1.5})$. To obtain the full $\mathcal{O}(N \log N)$ preformance, the above steps have to be performed over a hierarchy of successively coarser box levels.

The approximation (51) breaks down due to the singularity at $\mathbf{x} = \mathbf{y}$, when $\mathbf{x}_m$ and $\mathbf{y}_n$ are close enough that their two neighborhoods overlap. This case is removed from the multi-pole approximation and evaluated by direct matrix-vector multiply. Hence, the matrix-vector multiplication is decomposed in two parts,

$$Z\mathbf{j} = Z_{near}\mathbf{j} + Z_{far}\mathbf{j},$$

where the near matrix, Z_{near} responsible for the singular and near-singular part of the matrix elements, and $Z_{far} = Z - Z_{near}$. The MLFMA is applied only to the multiplication $Z_{far}\mathbf{j}$.

The near matrix includes a region around the self-interaction box $\mathbf{x}_m = \mathbf{y}_n$. The near width, n_w is defined as the number of layers of boxes around the self-interaction box that are included in the near matrix. Fig. 8 shows examples of $n_w = 1, 2$, and 3 in two space dimensions.

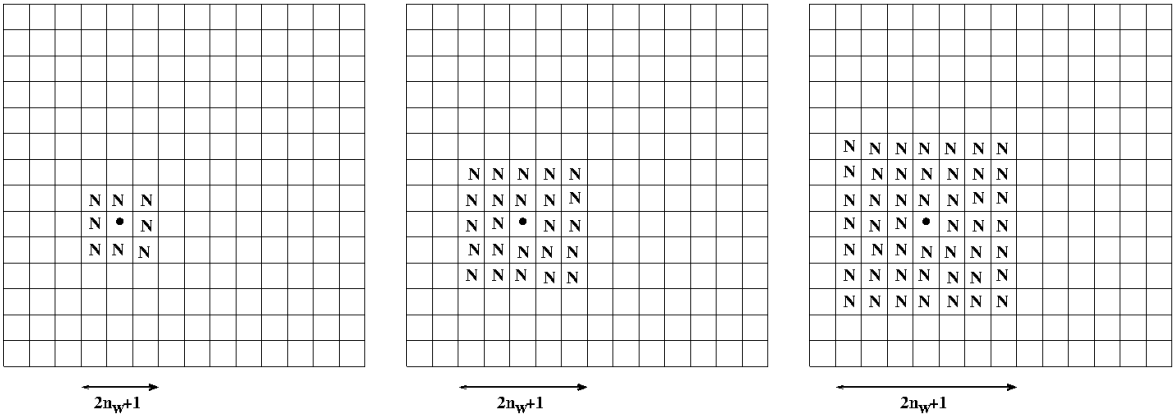

Figure 8: Box grid showing boxes in the near region of self-interaction box (black dot) marked by 'N'. Near widths are $n_w = 1$ (left), $n_w = 2$ (middle), and $n_w = 3$ (right).

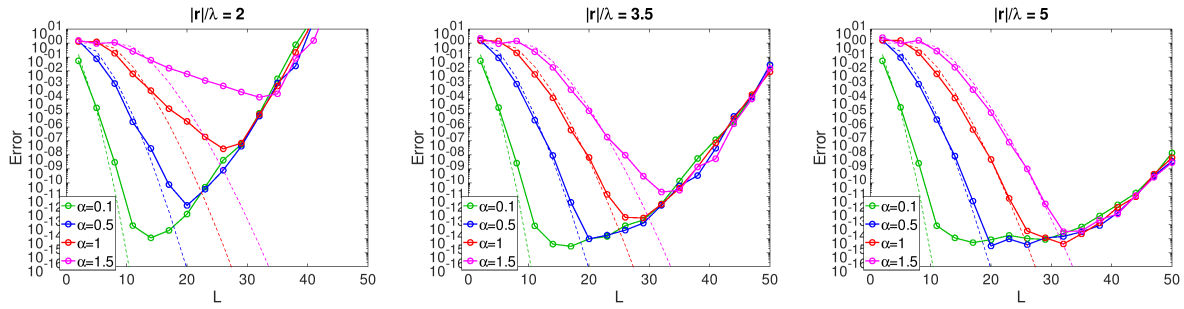

Figure 9: Error vs. L for box diameters 0.1 (green), 0.5 (blue), 1.0 (red), and 1.5 (magenta). Different subplots show different separations: $|\mathbf{r}| = 2$ (left), $|\mathbf{r}| = 3.5$ (middle), and $|\mathbf{r}| = 5$ (right).

4.3.1 Errors from the multipole approximation

When setting up the MLFMA, the near width, n_w, the size of the boxes, and the number of terms in the expansion, R, need to be selected in a way that a) makes the error of the approximation (51) small, and b) makes the computation efficient.

It is straightforward to verify that the relative error of (51) is invariant with respect to the length scale. The numerical experiments will be made with λ, the wavelength, as unit of length. Let s denote the length of the sides of the boxes. The scaled length of the box side will be denoted by $\alpha = s/\lambda$.

The error grows as the separation $|\mathbf{x}_m - \mathbf{y}_n|$ decreases. The error grows as the box size s increases. The maximum of the sum $|\mathbf{y} - \mathbf{y}_n| + |\mathbf{x} - \mathbf{x}_m|$ for $\mathbf{y}$ in box n and $\mathbf{x}$ in box m, is limited by the box diameter $d = \sqrt{2}s$, assuming two space dimensions.

Figure 9 shows some examples of this behavior. The relative error

$$e_M = |G(\mathbf{x}, \mathbf{y}) - \widehat{G}(\mathbf{x}, \mathbf{y})|/|G(\mathbf{x}, \mathbf{y})|$$

is plotted vs. L, the number of terms in function T_L. Because $R = 2L^2 + L$, L determines

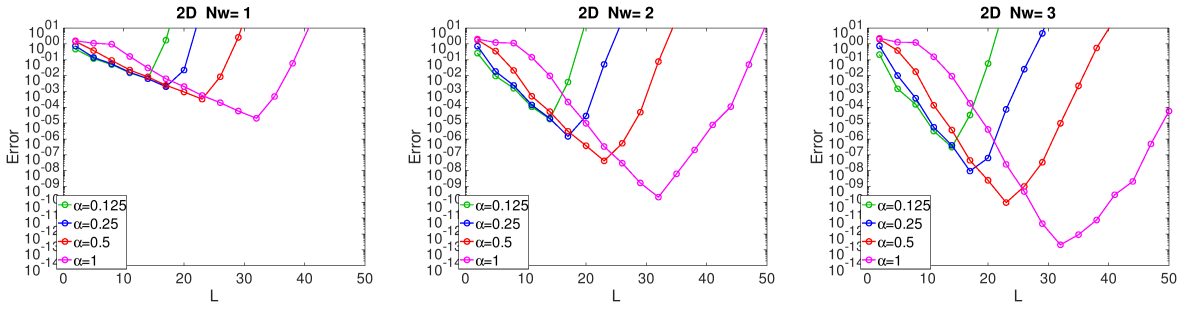

Figure 10: Error vs. L for different box widths. Different subplots show different near widths; $n_w = 1$ (left), $n_w = 2$ (middle), and $n_w = 3$ (right).

the number of terms R in (51). The location of $\mathbf{x}$ and $\mathbf{y}$ are choosen inside the boxes m and n respectively, in a way that makes the error large, determined by trial and error at a few locations near the corners or sides of the boxes. The separation is denoted by $|\mathbf{r}|$. Fig. 9 shows that the error does not decrease montonically when increasing the number of terms in the approximation. The approximation formula is numerically ill-conditioned and diverges if too many terms are used. The dashed curves in Figs. 9 show the error estimate given by the well-known formula (see [22])

$$L \approx kd + 1.8 d_0^{2/3} (kd)^{1/3}, \quad d_0 = log_{10}(1/\epsilon), \tag{52}$$

where $k = 2\pi/\lambda$, d is the box diameter, and ϵ is the error. Formula (52) does not depend on the separation. Fig. 9 indicates that (52) becomes increasingly accurate as the separation increases, as long as L is kept below the ill-conditioning limit.

For box grids, such as shown in Fig. 8, the smallest separation between box centers is $(n_w + 1)\alpha$. The largest error is then obtained for $|\mathbf{y} - \mathbf{y}_n| + |\mathbf{x} - \mathbf{x}_m| = \sqrt{2}\alpha$ and $|\mathbf{x}_m - \mathbf{y}_n| = (n_w + 1)\alpha$. It is therefore natural to plot the error as function of L with $|\mathbf{r}| = (n_w + 1)\alpha$ for different box sizes α.

This is done in Fig. 10, which shows the relative error vs. L for $n_w = 1, 2, 3$ and for box sizes $\alpha = 0.125, 0.25, 0.5$, and 1.

Fig. 11 is similar to Fig. 10, except that the box widths are now $\alpha = 1, 2, 4$, and 8, typical for the coarsened levels in the MLFMA. When coarsening the box grid, the number of terms has to be increased in order to maintain a fixed error. Formula (52) shows that L grows approximately linear rate with box size, implying that R grows quadratically with the grid refinement level.

Remark The grating height is usually less than one wavelength. The box discretization can be made two-dimensional as long as the box width is larger than, or on the order of, one wavelength. If the boxes are smaller than one wavelength, refinement of the box discretization in the z-direction becomes necessary.

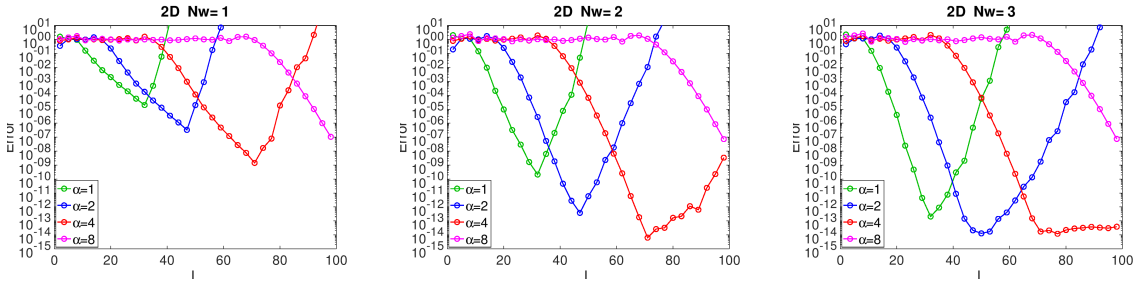

Figure 11: Error vs. L for different box widths. Different subplots show different near widths; $n_w = 1$ (left), $n_w = 2$ (middle), and $n_w = 3$ (right).

4.3.2 The near matrix

The most serious limitation to scaling up the problem size in the EFIE solver comes from the size of the near part of the matrix Z. The size of the near matrix grows linearly with number of degrees of freedom, but nevertheless in practice it becomes too large to fit in computer memory, or even on disk space, at realistic problem sizes for the grating compressor application.

The size of the near matrix is approximately

$$4(\alpha(2n_w + 1))^2 Q^4 \left(\frac{S}{\lambda}\right)^2 \tag{53}$$

matrix elements. The estimate assumes a square grating with side length S, and resolution Q along each dimension measured in points per wavelength.

With the FEM discretization, $Q = 20$ is a reasonable choice. If, e.g., the size of the grating is 10^4 wavelengths along each side, the near matrix would have

$$6.4 \times 10^{13}(\alpha(2n_w + 1))^2$$

elements. For example, taking $n_w = 1$ and $\alpha = 1$ and assuming each matrix element is a 16 byte double precision complex number, gives a total matrix size of 9 petabyte. This is impractical even on the largest super computers.

Figure 10 indicates a way to minimize the near matrix. If n_w is made larger, the box size α can be made smaller while keeping the error fixed. The combined effect of increasing n_w and decreasing α is to make $\alpha(2n_w + 1)$ smaller. As an example, if the desired error level is 10^{-5}, Fig. 10 shows that with near with $n_w = 1$, it is necessary to take $\alpha = 1$. If the near width is $n_w = 2$, the figure shows that it is possible to use $\alpha = 0.25$, and with $n_w = 3$, the desired accuracy can be obtained with $\alpha = 0.125$. Table 1 shows how the factor $(\alpha(2n_w + 1))^2$ in the near matrix size estimate (53) is reduced by more than a factor 10 when increasing the near width from 1 to 3.

Another reason to use $n_w > 1$ is, as seen in Fig. 10, that with $n_w = 1$ there are serious limitations on how small the error can be made.

Even with an optimal choice of n_w and α, the near matrix is prohibitively large. There are alternatives to (51) that are less restrictive for the case of small α. One such method is

Table 1: Matrix size factor for different near widths at fixed error level 10^{-5}.

n_w	α	$(\alpha(2n_w+1))^2$
1	1	9
2	0.25	1.56
3	0.125	0.77

the directional approximation based on Chebyshev interpolation, which will be examined in Section 5.

4.4 Numerical comparison between PO and EFIE

In this section, a numerical experient is presented to evaluate the difference between PO and EFIE. The dimensions in the numerical experiment are scaled down in order to be able to efficiently use the EFIE and PO solvers.

A given incident electric field impinges on a square grating with side $1.01088 \times 10^{-4}\, m$. The grating has sinusodial grating line profile of period $1.1765 \times 10^{-6}\, m$ and height $3.5 \times 10^{-7}\, m$. The base wavelength is $\lambda_0 = 1.053 \times 10^{-6}\, m$, which means there are approximately 96 wavelengths along each side of the grating.

The incident field is a Gaussian beam with beam waist, $w_0 = 1.132 \times 10^{-5}\, m$, located at the grating. Formulas (25)–(27) with $k = 2\pi/\lambda$, $z_0 = 0$, $z_R = kw_0^2/2$, $A_x = 1.0 \times 10^3$, and $A_y = 0$ give the incident x-polarized electric field. When y-polarization is used, the amplitudes are changed into $A_x = 0$ and $A_y = 1.0 \times 10^3$. The angle of incidence is $0.5\, rad$. In this setup there are two reflections; the zero order specular reflection and the first order reflection with reflection angle $\beta_1 = 0.428605\, rad$. The scattered field is evaluated on a square flat plate with side $7.0 \times 10^{-5}\, m$, placed in the path of the first order reflection, and normal to the reflected beam, at a distance $6.405 \times 10^{-5}\, m$ away.

The grating is discretized by a quadrilateral grid of 1920×1920 elements, corresponding to a resolution of 20 elements per wavelength. The grid also resolves the grating, because the grating period is on the order of a wavelength. The scattered field is evaluated on the observation screen at 100×100 equally spaced points.

Figure 12 shows contour levels of the real part of the surface current coefficients j_q on the grating, for only the vertical edges. The left subplot shows the computation by the EFIE, and the right subplot shows the solution obtained by PO. Fig. 13 compares the surface currents along the line $y = 4.686 \times 10^{-6}\, m$. The EFIE solution is plotted in blue color and the PO surface current in red color. The upper subplots show the real (left) and imaginary (right) parts of the surface current on the vertical edges. The lower subplots show the real (left) and imaginary (right) parts of the surface current on the horizontal edges. The grating lines are parallel to the y-axis.

Figure 14 shows a close up of the upper left subplot of Fig. 13 in the region near the origin. The figure also displays the grating profile in black color, scaled down by a factor

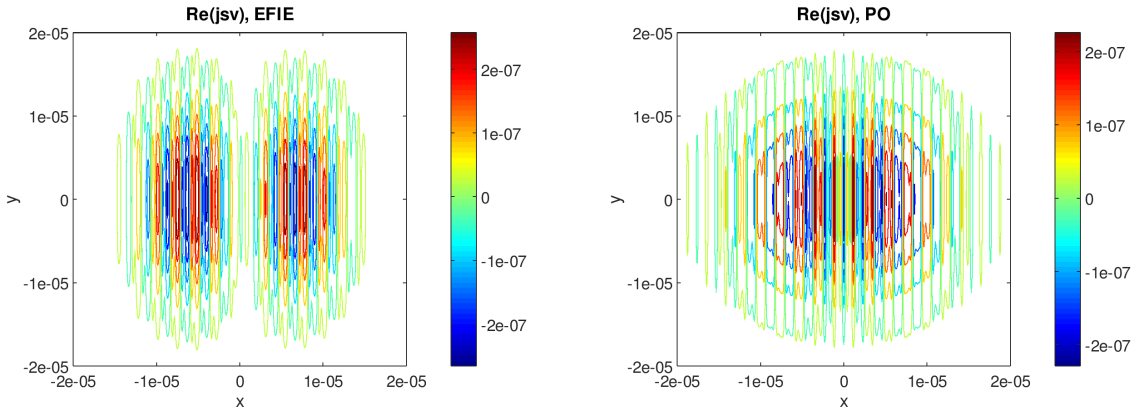

Figure 12: Real part of surface curent on vertical edges. EFIE (left) and PO (right).

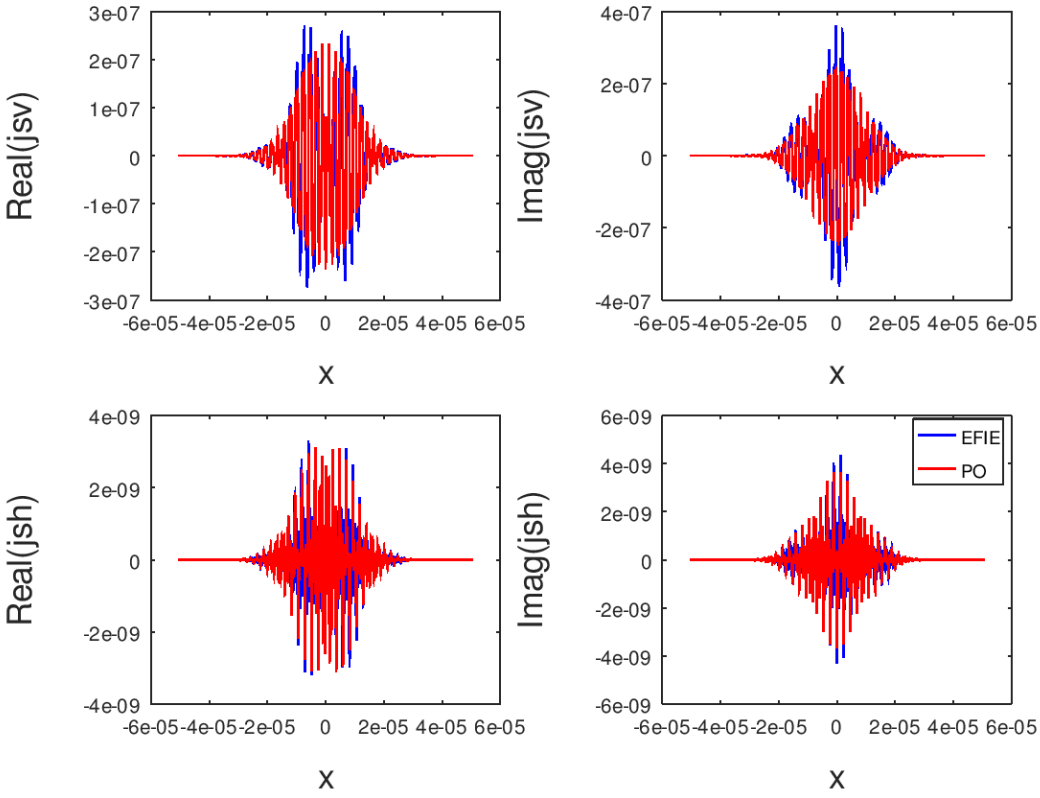

Figure 13: Real and imaginary parts of vertical and horizontal surface currents coefficients along $y = 4.686\,\mu m$. EFIE (blue) and PO (red).

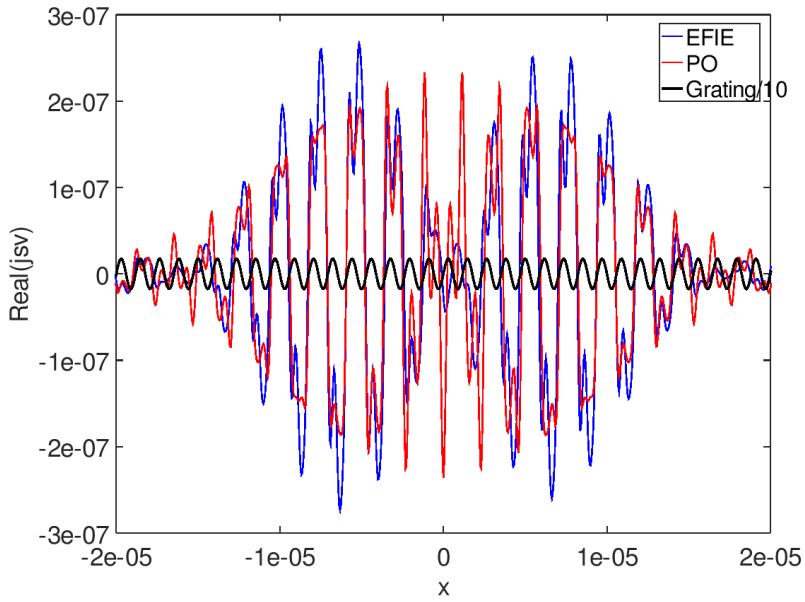

Figure 14: Real part of the vertical surface currents coefficient along $y = 4.686\,\mu m$. Close up near the center of the grating. EFIE (blue), PO (red), and grating profile(black).

10 to fit the scale of the plot. The EFIE and PO surface currents have similar phase, but differs significantly in amplitude. The scattered electric fields on the observation screen are displayed in Figs. 15–16. Figure 15 shows the field evaluated from the surface current computed by the EFIE, and Fig. 16 shows the field from the surface current computed by the PO approximation. The two solutions are of similar appearance in the plots. However, the color scale indicated by the color bars reveals that the EFIE and the PO solutions have different magnitudes.

Fig. 17 shows plots of the scattered field vs. x along $y = 0$. The field scattered from surface current computed by the EFIE is plotted in blue, while the corresponding PO field is plotted in red. The two solutions appear to be of similar shape but with different amplitudes. From Figs. 15–17, and from other unreported numerical experiments, it seems likely that the scattered field computed by the EFIE can be approximated with good precision by the scattered field computed by PO times a complex scaling factor,

$$\mathbf{E}_{sc}^{EFIE}(\mathbf{x}) \approx z_* \mathbf{E}_{sc}^{PO}(\mathbf{x}). \tag{54}$$

To investigate this conjecture numerically, the scaling factor z_* and the accuracy of the approximation (54) were computed for wavelengths $\lambda = \lambda_0 \pm 6$, nm and different angles of incidence. The results are summarized in Table 2. The angles of incidence in the last three rows of Table 2 are the exit angles obtained from (1) when the incident angle is 0.5. In the full compressor simulation, these angles are incident at the second grating. The third column of Table 2 shows the polarization used. In all cases except one, the incident field is x-polarized. In the full compressor simulation, the pulse is x polarized

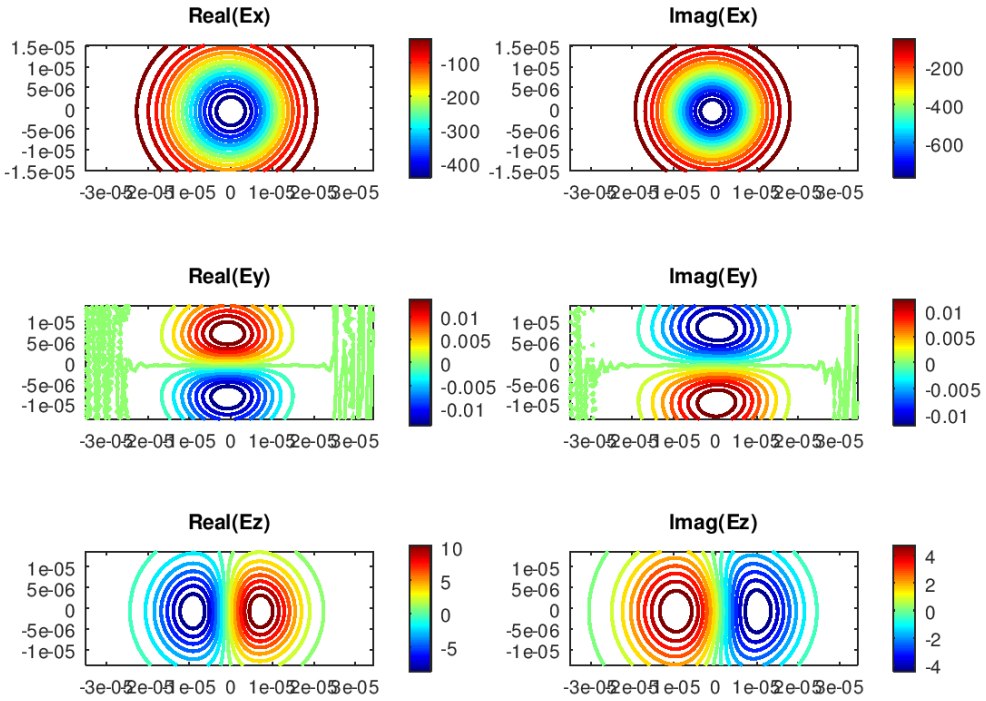

Figure 15: Scattered field on an observation screen, computed from the EFIE surface current. The subfigures show: real part of $\mathbf{E}^{(x)}$ (upper left), imaginary part of $\mathbf{E}^{(x)}$ (upper right) real part of $\mathbf{E}^{(y)}$ (middle left), imaginary part of $\mathbf{E}^{(y)}$ (middle right) real part of $\mathbf{E}^{(z)}$ (lower left), imaginary part of $\mathbf{E}^{(z)}$ (lower right)

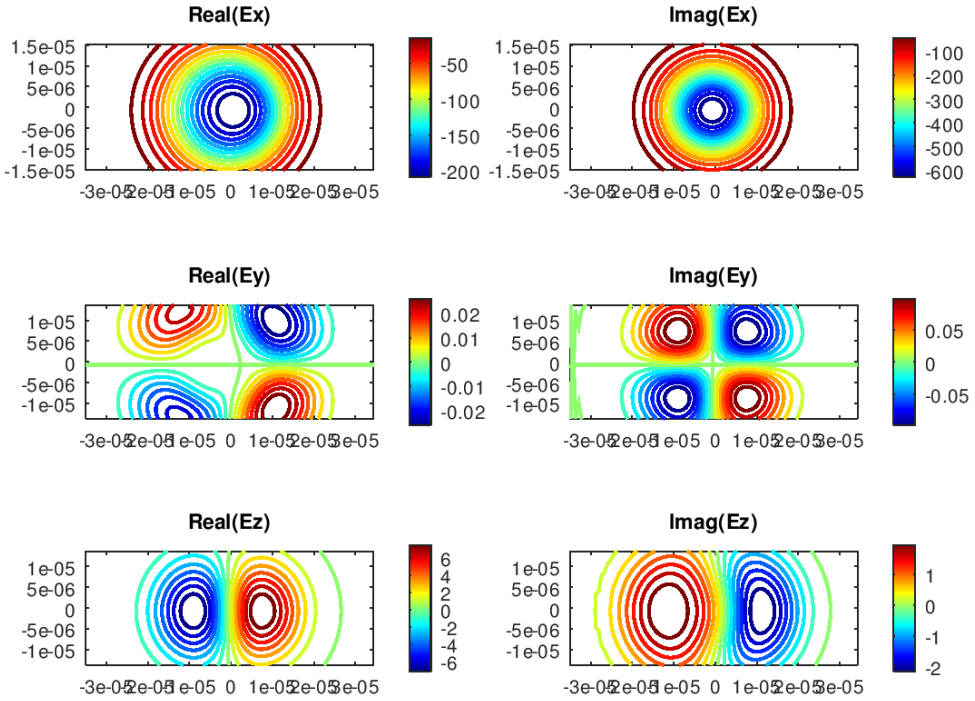

Figure 16: Scattered field on an observation screen, computed from the PO surface current. The subfigures show: real part of $\mathbf{E}^{(x)}$ (upper left), imaginary part of $\mathbf{E}^{(x)}$ (upper right) real part of $\mathbf{E}^{(y)}$ (middle left), imaginary part of $\mathbf{E}^{(y)}$ (middle right) real part of $\mathbf{E}^{(z)}$ (lower left), imaginary part of $\mathbf{E}^{(z)}$ (lower right)

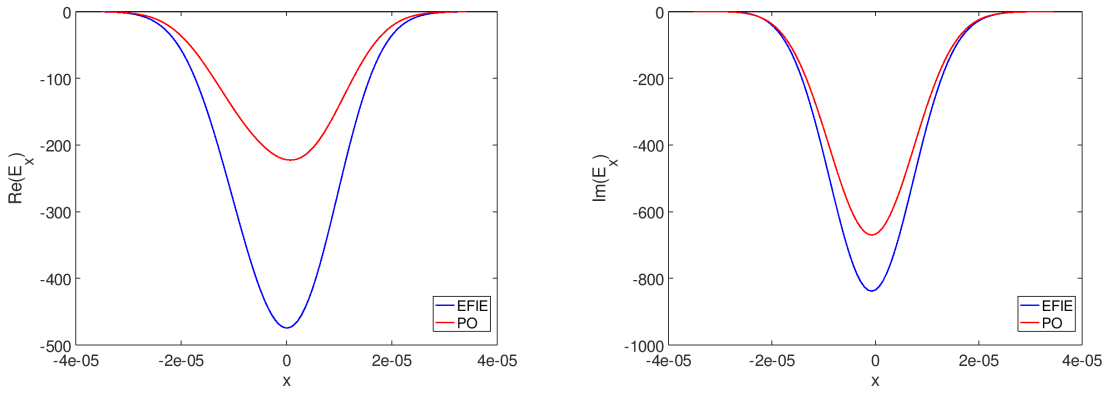

Figure 17: The x-component of the scattered electric field on an observation screen along $y = 0$. The left subplot shows the real part and right subplot shows the imaginary part. EFIE in blue color, PO in red color.

λ	α_{in}	Polarization	z_*	e_r
1.053000e-06	0.5	x	1.3384 - i0.264542	4.159251e-03
1.059000e-06	0.5	x	1.33611 - i0.251531	3.738560e-03
1.047000e-06	0.5	x	1.34047 - i0.27826	4.627962e-03
1.053000e-06	0.5	y	0.983974 + i0.388689	1.553897e-03
1.053000e-06	0.25	x	1.19522 + i0.427491	4.012426e-02
1.053000e-06	0.75	x	1.10786 + i0.497721	4.410252e-02
1.053000e-06	0.428605	x	1.33856 - i0.265264	4.338732e-03
1.059000e-06	0.434219	x	1.33622 - i0.251656	3.975381e-03
1.047000e-06	0.423005	x	1.34059 - i0.278417	4.919738e-03

Table 2: Result from fitting the PO and EFIE scattered fields to the relation (54). The columns show wavelength, angle of incidence, polarization of the incident field, the scaling coefficient z_*, and the relative error.

with variation in wavelength the same as used in the table.

Table 2 shows the estimated scaling factor, using the least squares formula

$$z_* = \frac{(\mathbf{E}_{sc}^{EFIE}, \mathbf{E}_{sc}^{PO})_2}{(\mathbf{E}_{sc}^{EFIE}, \mathbf{E}_{sc}^{EFIE})_2}$$

to define z_*. The scalar product and norm are defined by

$$(\mathbf{E}_1, \mathbf{E}_2)_2 = \frac{1}{N_o} \sum_{q=1}^{N_o} (\mathbf{E}_1)_q^H (\mathbf{E}_2)_q \qquad ||\mathbf{E}||_2 = \sqrt{(\mathbf{E}, \mathbf{E})_2}$$

where N_o is the number of points on the observation screen, and $\mathbf{E}_q$ denotes the field at point q.

The last column of Table 2 shows the relative error in the approximation,

$$e_r = \frac{||\mathbf{E}_{sc}^{EFIE} - z_* \mathbf{E}_{sc}^{PO}||_2}{||\mathbf{E}_{sc}^{EFIE}||_2},$$

which stays below 0.5% for all cases, except when $\alpha_{in} = 0.25$ or $\alpha_{in} = 0.75$.

5 Directional interpolation of the farfield

The complexity for naively evaluating the discretized electric (48) or magnetic (49) fields due to N_{tot} point sources at M_{tot} receiver locations would be $\mathcal{O}(N_{tot} M_{tot})$. Similar to the classical fast multipole method [14], we can accelerate the evaluation of those sums by grouping sources and receiver locations into clusters and applying a hierarchical technique based on a directional Chebyshev interpolation approach [19].

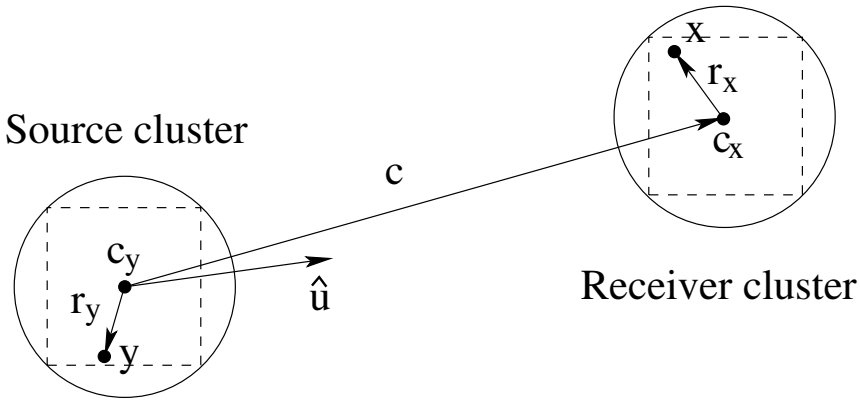

Figure 18: The geometry of the source and receiver clusters.

5.1 The directional kernel

Let $\mathbf{c}_x \in \mathbb{R}^3$ and $\mathbf{c}_y \in \mathbb{R}^3$ be the locations of the centers of two clusters in which the points $\mathbf{x} \in \mathbb{R}^3$ and $\mathbf{y} \in \mathbb{R}^3$ are located (see Figure 18). Furthermore, let

$$\mathbf{x} = \mathbf{c}_x + \mathbf{r}_x, \quad \mathbf{y} = \mathbf{c}_y + \mathbf{r}_y.$$

We assume that both clusters have diameter $d > 0$, i.e., $|\mathbf{r}_x| \leq d/2$ and $|\mathbf{r}_y| \leq d/2$, such that

$$\mathbf{x} - \mathbf{y} = (\mathbf{c}_x - \mathbf{c}_y) + (\mathbf{r}_x - \mathbf{r}_y) =: \mathbf{c} + \mathbf{r}, \quad \mathbf{c} = \mathbf{c}_x - \mathbf{c}_y, \quad \mathbf{r} = \mathbf{r}_x - \mathbf{r}_y, \quad |\mathbf{r}| \leq d.$$

Let $k > 0$ and $i = \sqrt{-1}$. Following the ideas of Messner et al. [19], we write the Green's function for Helmholtz equation as

$$G(\mathbf{x}, \mathbf{y}) = e^{-ik\hat{\mathbf{u}}\cdot(\mathbf{x}-\mathbf{y})} K^u(\mathbf{x}, \mathbf{y}), \quad K^u(\mathbf{x}, \mathbf{y}) = \frac{\exp(ik\hat{\mathbf{u}} \cdot (\mathbf{x} - \mathbf{y}) - ik|\mathbf{x} - \mathbf{y}|)}{4\pi|\mathbf{x} - \mathbf{y}|}. \tag{55}$$

The function K^u is called the directional kernel associated with the unit direction $\hat{\mathbf{u}} \in \mathbb{R}^3$.

The directional kernel can be written as function of $\mathbf{r}$,

$$K^u(\mathbf{r}) = \frac{e^{i\phi(\mathbf{r})}}{4\pi|\mathbf{c} + \mathbf{r}|}, \quad \phi(\mathbf{r}) = k\left(\hat{\mathbf{u}} \cdot (\mathbf{c} + \mathbf{r}) - |\mathbf{c} + \mathbf{r}|\right) \in \mathbb{R}. \tag{56}$$

We have,

$$|\mathbf{c} + \mathbf{r}|^2 = |\mathbf{c}|^2 + 2\mathbf{c} \cdot \mathbf{r} + |\mathbf{r}|^2 = |\mathbf{c}|^2 \left(1 + \frac{2d}{|\mathbf{c}|}(\hat{\mathbf{c}} \cdot \boldsymbol{\rho}) + \frac{d^2}{|\mathbf{c}|^2}|\boldsymbol{\rho}|^2\right), \quad \boldsymbol{\rho} = \frac{\mathbf{r}}{d}.$$

where $\hat{\mathbf{c}} = \mathbf{c}/|\mathbf{c}|$ and $|\boldsymbol{\rho}| \leq 1$. For $d/|\mathbf{c}| \ll 1$ we have $\varepsilon := 2(\hat{\mathbf{c}} \cdot \boldsymbol{\rho})\, d/|\mathbf{c}| + |\boldsymbol{\rho}|^2\, d^2/|\mathbf{c}|^2 \ll 1$. A Taylor series expansion of $\sqrt{1+\varepsilon}$ gives

$$|\mathbf{c} + d\boldsymbol{\rho}| = |\mathbf{c}| \left(1 + \frac{1}{2}\left(\frac{2d}{|\mathbf{c}|}(\hat{\mathbf{c}} \cdot \boldsymbol{\rho}) + \frac{d^2}{|\mathbf{c}|^2}|\boldsymbol{\rho}|^2\right) - \frac{1}{8}\left(\frac{2d}{|\mathbf{c}|}(\hat{\mathbf{c}} \cdot \boldsymbol{\rho}) + \frac{d^2}{|\mathbf{c}|^2}|\boldsymbol{\rho}|^2\right)^2 + \mathcal{O}(\varepsilon^3)\right).$$

We can write the phase angle in (56) as

$$\phi(d\boldsymbol{\rho}) = \phi_0 + \phi_1(\boldsymbol{\rho}) + k|\mathbf{c}|R(\boldsymbol{\rho}), \quad R(\boldsymbol{\rho}) = \mathcal{O}\left(\frac{d^3}{|\mathbf{c}|^3}\right) \in \mathbb{R}, \tag{57}$$

where

$$\phi_0 = k|\mathbf{c}|\left(\hat{\mathbf{u}}\cdot\hat{\mathbf{c}} - 1\right), \tag{58}$$

$$\phi_1(\boldsymbol{\rho}) = kd\left(\hat{\mathbf{u}} - \hat{\mathbf{c}}\right)\cdot\boldsymbol{\rho} - \frac{kd^2}{2|\mathbf{c}|}\left(|\boldsymbol{\rho}|^2 - (\hat{\mathbf{c}}\cdot\boldsymbol{\rho})^2\right). \tag{59}$$

Away from the singularity, the Green's function for Helmholtz equation varies on the length scale of the wave length, $\lambda = 2\pi/k$. Under certain conditions that will be stated below, the directional kernel varies on a significantly longer length scale, which allows it the be efficiently approximated by a Chebyshev interpolant. In the following, we assume that $\mathbf{x}$ and $\mathbf{y}$ are well separated from the singularity, $|\mathbf{c}| > 2d$, such that the properties of the directional kernel can be modeled by the normalized directional kernel

$$\widetilde{K}^u(\mathbf{r}) = \frac{K^u(\mathbf{r})}{|K^u(\mathbf{r})|} = \exp(i\phi(\mathbf{r})). \tag{60}$$

5.2 Scaling properties of the normalized directional kernel

The error in the approximation for the directional kernel depends on the cluster diameter, d, the separation $|\mathbf{c}|$, and the aperture, which can be measured as $|\hat{\mathbf{u}} - \hat{\mathbf{c}}|$. The following lemma shows that the problem dimensions can be scaled up, while keeping the phase function approximately invariant.

Lemma 1. *Consider a cluster size $d_1 > 0$, a separation vector $\mathbf{c}_1 = |\mathbf{c}_1|\hat{\mathbf{c}}$, and a direction $\hat{\mathbf{u}}_1$ where the angle between $\hat{\mathbf{c}}$ and $\hat{\mathbf{u}}_1$ equals $\varphi_1 \geq 0$. Let $\alpha \geq 1$ be a scaling factor, that scales up the problem according to*

$$d = \alpha d_1, \tag{61}$$

$$\mathbf{c} = \alpha^2 \mathbf{c}_1, \tag{62}$$

$$|\hat{\mathbf{u}} - \hat{\mathbf{c}}| = \frac{1}{\alpha}|\hat{\mathbf{u}}_1 - \hat{\mathbf{c}}|. \tag{63}$$

Furthermore assume a two dimensional configuration, so that $\mathbf{c}_1$, $\hat{\mathbf{u}}_1$, $\hat{\mathbf{u}}$, and $\boldsymbol{\rho}$ are in the same plane. Then the phase functions (58) and (59) of the scaled variables, $\phi_0(\alpha)$ and $\phi_1(\alpha)$ satisfy

$$\phi_0(\alpha) = k|\mathbf{c}|(\hat{\mathbf{u}}\cdot\hat{\mathbf{c}} - 1) = k|\mathbf{c}_1|(\hat{\mathbf{u}}_1\cdot\hat{\mathbf{c}} - 1) \tag{64}$$

$$\phi_1(\alpha) = \phi_{1,\infty} + \mathcal{O}(\alpha^{-1}) \tag{65}$$

when $\alpha \to \infty$. Here

$$\phi_{1,\infty} = kd_1|\hat{\mathbf{u}}_1 - \hat{\mathbf{c}}||\boldsymbol{\rho}|\cos(\theta_1 - \varphi_1/2) - \frac{kd_1^2}{2|\mathbf{c}_1|}\left(|\boldsymbol{\rho}|^2 - (\hat{\mathbf{c}}\cdot\boldsymbol{\rho})^2\right),$$

where θ_1 is the angle between $\boldsymbol{\rho}$ and $\hat{\mathbf{u}}_1 - \hat{\mathbf{c}}$.

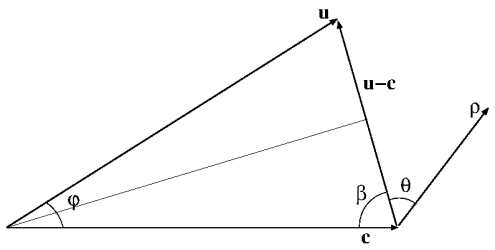

Figure 19: By drawing the normal bisecting φ, it is seen that the angle β between $\hat{\mathbf{c}}$ and $\hat{\mathbf{u}} - \hat{\mathbf{c}}$ is equal to $\pi/2 - \varphi/2$. The angle $\beta + \theta$ is invariant when $\hat{\mathbf{u}}$ is moving, since $\hat{\mathbf{c}}$ and $\boldsymbol{\rho}$ are fixed. Therefore, $\theta - \varphi/2$ is invariant.

Note, the vector $\mathbf{r}$ is scaled by α in the same way as the cluster diameter. The vectors $\hat{\mathbf{c}}$ and $\boldsymbol{\rho}$ are unchanged by the scaling (61)–(63). Moreover, the remainder, $k|\mathbf{c}|R$, in the phase function (57), behaves as $\mathcal{O}(\alpha^{-1})$ for large α.

The significance of Lemma 1 is that if the error in the directional approximation of $G(\mathbf{x}, \mathbf{y})$ is known for some problem parameters d, $|\mathbf{c}|$, $\hat{\mathbf{u}}$, scaling the problem size by (61)–(63) to a larger α will essentially leave the phase function, and thereby the error, invariant. This property will be used to facilitate selection of the problem parameters d, $|\mathbf{c}|$, and $\hat{\mathbf{u}}$ to achieve a given error tolerance.

Remark 1. *The assumption of two-dimensionality in Lemma 1 can be replaced by the somewhat weaker requirement that for any α, $\hat{\mathbf{u}}$ resides in the plane spanned by $\mathbf{c}_1$ and $\hat{\mathbf{u}}_1$. The proof below then holds with $\boldsymbol{\rho}$ replaced by its projection onto that plane.*

Proof. Because

$$|\hat{\mathbf{u}} - \hat{\mathbf{c}}|^2 = 1 - 2\hat{\mathbf{u}} \cdot \hat{\mathbf{c}} + 1 = 2(1 - \hat{\mathbf{u}} \cdot \hat{\mathbf{c}}), \tag{66}$$

it follows that

$$\phi_0(\alpha) = k|\mathbf{c}|(\hat{\mathbf{u}} \cdot \hat{\mathbf{c}} - 1) = -\frac{1}{2} k|\mathbf{c}||\hat{\mathbf{u}} - \hat{\mathbf{c}}|^2,$$

the scale invariance of which is straightforward from (62) and (63).

Let θ be the angle between $\hat{\mathbf{u}} - \hat{\mathbf{c}}$ and $\boldsymbol{\rho}$, so that $(\hat{\mathbf{u}} - \hat{\mathbf{c}}) \cdot \boldsymbol{\rho} = |\hat{\mathbf{u}} - \hat{\mathbf{c}}||\boldsymbol{\rho}| \cos\theta$. For ϕ_1 in scaled variables

$$\phi_1(\alpha) = kd|\hat{\mathbf{u}} - \hat{\mathbf{c}}||\boldsymbol{\rho}| \cos\theta - \frac{kd^2}{2|\mathbf{c}|} \left(|\boldsymbol{\rho}|^2 - (\hat{\mathbf{c}} \cdot \boldsymbol{\rho})^2 \right)$$

The second term is scale invariant from (61) and (62). For the first term

$$kd|\hat{\mathbf{u}} - \hat{\mathbf{c}}||\boldsymbol{\rho}| \cos\theta = kd_1|\hat{\mathbf{u}}_1 - \hat{\mathbf{c}}||\boldsymbol{\rho}| \cos\theta, \tag{67}$$

however this is not perfectly scale invariant since θ depends on α. To investigate how θ depends on α, first note that from geometric considerations it holds that

$$\theta - \varphi/2 = \theta_1 - \varphi_1/2, \tag{68}$$

see Fig. 19. Secondly, equation (66) gives $|\hat{\mathbf{u}} - \hat{\mathbf{c}}|^2 = 2(1 - \cos\varphi) = 4\sin^2\varphi/2$, so that $|\hat{\mathbf{u}} - \hat{\mathbf{c}}| = 2|\sin\varphi/2|$. The scaling (63) gives

$$\alpha \sin\varphi/2 = \sin\varphi_1/2$$

and, hence, for α large,

$$\varphi = 2\arcsin(\frac{1}{\alpha}\sin\varphi_1/2) = \frac{2}{\alpha}\sin\varphi_1/2 + \mathcal{O}(\alpha^{-3}). \tag{69}$$

Combining (69) and (68) shows that

$$\begin{aligned}\cos\theta = \cos(\theta_1 - \varphi_1/2 + \varphi/2) &= \cos(\theta_1 - \varphi_1/2)\cos\varphi/2 - \sin(\theta_1 - \varphi_1/2)\sin\varphi/2 \\ &= \cos(\theta_1 - \varphi_1/2) + \mathcal{O}(\alpha^{-1}),\end{aligned} \tag{70}$$

and (65) follows by inserting (70) into (67). □

5.3 1-D directional Chebyshev interpolation

A standard accuracy result for Chebyshev interpolation [26] is stated in the following lemma.

Lemma 2. *Let $f(\xi)$ be a smooth function defined on the unit interval $\xi \in [-1, 1]$. Its Chebyshev interpolant is a polynomial of degree $\ell - 1 \geq 0$, defined by*

$$f_\ell(\xi) = \sum_{m=1}^{\ell} \sigma_\ell(\xi, \bar{\xi}_m) f(\bar{\xi}_m), \quad \xi \in [-1, 1], \tag{71}$$

where

$$\sigma_\ell(\xi, \bar{\xi}_m) = \frac{1}{\ell} + \frac{2}{\ell}\sum_{n=1}^{\ell-1} T_n(\xi) T_n(\bar{\xi}_m). \tag{72}$$

Here, $T_n(\xi)$ is the nth order Chebyshev polynomial of the first kind and $\bar{\xi}_m$ is the mth Chebyshev-Lobatto node point,

$$\bar{\xi}_m = \cos\left(\frac{(2m-1)\pi}{2\ell}\right), \quad m = 1, 2, \ldots, \ell. \tag{73}$$

The interpolation error can be bounded by

$$|f_\ell - f|_\infty \leq \frac{1}{2^\ell(\ell+1)!} \max_{\xi\in[-1,1]} \left|f^{(\ell+1)}(\xi)\right|. \tag{74}$$

To illustrate the properties of the normalized directional kernel (60), consider the one-dimensional case where

$$\mathbf{r}_x = \frac{d}{2}\xi\hat{\mathbf{e}}, \quad \mathbf{r}_y = \frac{d}{2}\eta\hat{\mathbf{e}}, \quad (\xi, \eta) \in [-1, 1]^2,$$

for some unit direction $\hat{\mathbf{e}} \in \mathbb{R}^3$ and a fixed cluster separation vector $\mathbf{c}$. Then, $\boldsymbol{\rho} = (\xi-\eta)\hat{\mathbf{e}}/2$ and we define

$$\kappa(\xi,\eta) := \widetilde{K}^u(d\boldsymbol{\rho}) = \kappa_1(\xi,\eta)e^{ir(\xi,\eta)}, \quad \kappa_1(\xi,\eta) = e^{i\psi(\xi,\eta)}, \tag{75}$$

where $r(\xi,\eta) = k|\mathbf{c}|R((\xi-\eta)\hat{\mathbf{e}}/2)$ is the remainder term and the phase angle satisfies

$$\psi(\xi,\eta) = \phi_0 + \frac{kd(\xi-\eta)}{2}(\hat{\mathbf{u}}-\hat{\mathbf{c}})\cdot\hat{\mathbf{e}} - \frac{kd^2(\xi-\eta)^2}{8|\mathbf{c}|}\left(1-(\hat{\mathbf{c}}\cdot\hat{\mathbf{e}})^2\right). \tag{76}$$

If the remainder term is small, the properties of the modified kernel (60) are determined by $\kappa_1(\xi,\eta)$.

A Chebyshev interpolant of $\kappa_1(\xi,\eta)$ can be constructed by first interpolating in η followed by interpolating in ξ,

$$\kappa_{1,l}(\xi,\eta) = \sum_{m=1}^{\ell}\sigma_\ell(\xi,\bar{\xi}_m)\sum_{n=1}^{\ell}\sigma_\ell(\eta,\bar{\eta}_n)\kappa_1(\bar{\xi}_m,\bar{\eta}_n), \quad (\xi,\eta)\in[-1,1]^2. \tag{77}$$

As we proceed to show, the accuracy of the interpolant is controlled by the non-dimensional coefficients

$$C_a = kd|\hat{\mathbf{u}}-\hat{\mathbf{c}}|, \quad C_s = \frac{kd^2}{|\mathbf{c}|}. \tag{78}$$

To estimate the error in the two-dimensional interpolant we define the max-norm of functions $f(\xi,\eta)$ in $(\xi,\eta)\in[-1,1]^2$ by

$$|f|_\infty = \max_{-1\le\xi\le1,-1\le\eta\le1}|f(\xi,\eta)|.$$

The following Lemma gives an error estimate for the interpolant.

Lemma 3. *The error in the Chebyshev interpolant $\kappa_{1,\ell}(\xi,\eta)$, defined by (77), can be bounded by*

$$|\kappa_{1,\ell}-\kappa_1|_\infty \le \frac{|P_{\ell+1}(a,b)|_\infty}{2^{2\ell}(\ell+1)!} \le \frac{P_{\ell+1}(C_a+C_s,C_s)}{2^{2\ell}(\ell+1)!}, \tag{79}$$

where $a = i\psi_1'(\zeta)$ and $b = i\psi_1''(\zeta)$, with $\zeta = (\xi-\eta)/2 \in [-1,1]$. The polynomial $P_{\ell+1}(a,b)$ is defined in Appendix A by (133) and the coefficients are given in (134). For all $\ell \ge 1$, $P_{\ell+1}(0,0) = 0$. For real arguments, $\alpha > 0$ and $\beta > 0$, the polynomial $P_q(\alpha,\beta)$ is a monotonically increasing function of both arguments.

Proof. By defining the Chebyshev interpolant in the η-direction,

$$\widetilde{\kappa}(\xi,\eta) = \sum_{n=1}^{\ell}\sigma_\ell(\eta,\bar{\eta}_n)\kappa_1(\xi,\bar{\eta}_n),$$

the interpolant (77) can be written

$$\kappa_{1,l}(\xi,\eta) = \sum_{m=1}^{\ell}\sigma_\ell(\xi,\bar{\xi}_m)\widetilde{\kappa}(\bar{\xi}_m,\eta). \tag{80}$$

Define the η-direction interpolation error by

$$e_\eta(\xi,\eta) = \widetilde{\kappa}(\xi,\eta) - \kappa_1(\xi,\eta)$$

and rewrite the interpolant (80) as

$$\kappa_{1,l}(\xi,\eta) = \sum_{m=1}^{\ell} \sigma_\ell(\xi,\bar{\xi}_m)\kappa_1(\bar{\xi}_m,\eta) + \sum_{m=1}^{\ell} \sigma_\ell(\xi,\bar{\xi}_m)e_\eta(\bar{\xi}_m,\eta).$$

The interpolation error can now be expressed as

$$\kappa_{1,l}(\xi,\eta) - \kappa_1(\xi,\eta) = \left(\sum_{m=1}^{\ell} \sigma_\ell(\xi,\bar{\xi}_m)\kappa_1(\bar{\xi}_m,\eta) - \kappa_1(\xi,\eta)\right) + \sum_{m=1}^{\ell} \sigma_\ell(\xi,\bar{\xi}_m)e_\eta(\bar{\xi}_m,\eta).$$

where the first two terms on the right hand side are the interpolation error in the ξ-direction, and the third term is the η-direction error interpolated in the ξ-direction. Denoting

$$e_\xi(\xi,\eta) = \sum_{m=1}^{\ell} \sigma_\ell(\xi,\bar{\xi}_m)\kappa_1(\bar{\xi}_m,\eta) - \kappa_1(\xi,\eta)$$

we obtain for the error,

$$\kappa_{1,l}(\xi,\eta) - \kappa_1(\xi,\eta) = e_\xi + \sum_{m=1}^{\ell} \sigma_\ell(\xi,\bar{\xi}_m)e_\eta(\bar{\xi}_m,\eta).$$

The one dimensional bound (74) can be applied in the ξ variable, for each η to give

$$|e_\xi|_\infty \leq \frac{1}{2^\ell(\ell+1)!}|\frac{\partial^{l+1}\kappa_1}{\partial\xi^{l+1}}|_\infty$$

Because the Chebyshev polynomials satisfy the bound $|T_n(\xi)| \leq 1$ for $-1 \leq \xi \leq 1$,

$$\max_{-1\leq\xi\leq 1} |\sigma_l(\xi,\bar{\xi}_m)| \leq 1/\ell + 2(\ell-1)/\ell = 2 - \frac{1}{\ell},$$

so that

$$|\sum_{m=1}^{\ell} \sigma_\ell(\xi,\bar{\xi}_m)e_\eta(\bar{\xi}_m,\eta)|_\infty \leq \ell\left(2-\frac{1}{\ell}\right)|e_\eta|_\infty \leq (2\ell-1)\frac{1}{2^\ell(\ell+1)!}|\frac{\partial^{l+1}\kappa_1}{\partial\eta^{l+1}}|_\infty$$

Thus, the total interpolation error can be bounded by

$$|\kappa_{1,\ell} - \kappa_1|_\infty \leq \frac{1}{2^\ell(\ell+1)!}\left(|\frac{\partial^{l+1}\kappa_1}{\partial\xi^{l+1}}|_\infty + (2\ell-1)|\frac{\partial^{l+1}\kappa_1}{\partial\eta^{l+1}}|_\infty\right).$$

The same estimate made with the ξ-direction interpolation before the η-direction interpolation, leads by symmetry to

$$|\kappa_{1,\ell} - \kappa_1|_\infty \leq \frac{1}{2^\ell(\ell+1)!}\left((2\ell-1)|\frac{\partial^{l+1}\kappa_1}{\partial\xi^{l+1}}|_\infty + |\frac{\partial^{l+1}\kappa_1}{\partial\eta^{l+1}}|_\infty\right).$$

The two estimates are averaged to give the final, symmetric, estimate

$$|\kappa_{1,\ell} - \kappa_1|_\infty \leq \frac{\ell}{2^\ell(\ell+1)!}\left(|\frac{\partial^{l+1}\kappa_1}{\partial\xi^{l+1}}|_\infty + |\frac{\partial^{l+1}\kappa_1}{\partial\eta^{l+1}}|_\infty\right),$$

for the two-dimensional Chebyshev interpolation error.

It is convenient to express the kernel and phase function in terms of $\zeta = 0.5(\xi - \eta)$,

$$\kappa_1(\zeta) = e^{i\psi_1(\zeta)}, \quad \psi_1(\zeta) = \phi_0 + kd\zeta(\hat{\mathbf{u}} - \hat{\mathbf{c}})\cdot\hat{\mathbf{e}} - \frac{kd^2\zeta^2}{2|\mathbf{c}|}\left(1 - (\hat{\mathbf{c}}\cdot\hat{\mathbf{e}})^2\right), \quad \zeta \in [-1, 1]. \tag{81}$$

The derivatives satisfy

$$\frac{\partial^q\kappa_1}{\partial\xi^q} = \frac{1}{2^q}\frac{d^q\kappa_1}{d\zeta^q}, \quad \frac{\partial^q\kappa_1}{\partial\eta^q} = (-1)^q\frac{1}{2^q}\frac{d^q\kappa_1}{d\zeta^q}, \quad q = 1, 2, \ldots,$$

and the bound for the total interpolation error can be written

$$|\kappa_{1,\ell} - \kappa_1|_\infty \leq \frac{\ell}{2^\ell(\ell+1)!}\frac{1}{2^\ell}\max_{-1\leq\zeta\leq 1}\left|\frac{d^{\ell+1}\kappa_1(\zeta)}{d\zeta^{\ell+1}}\right| \tag{82}$$

We have

$$\frac{d\psi_1}{d\zeta} = kd(\hat{\mathbf{u}} - \hat{\mathbf{c}})\cdot\hat{\mathbf{e}} - \frac{kd^2\zeta}{|\mathbf{c}|}(1 - (\hat{\mathbf{c}}\cdot\hat{\mathbf{e}})^2), \quad \frac{d^2\psi_1}{d\zeta^2} = -\frac{kd^2}{|\mathbf{c}|}(1 - (\hat{\mathbf{c}}\cdot\hat{\mathbf{e}})^2).$$

Because the third and all higher derivatives of the phase function $\psi_1(\zeta)$ are zero, the derivatives of $\kappa_1(\zeta)$ satisfy (see Appendix A)

$$\begin{aligned}
\kappa_1' &= \kappa_1 a,\\
\kappa_1'' &= \kappa_1\left(a^2 + b\right),\\
\kappa_1^{(3)} &= \kappa_1\left(a^3 + 3ab\right),\\
\kappa_1^{(4)} &= \kappa_1\left(a^4 + 6a^2b + 3b^2\right),\\
\kappa_1^{(5)} &= \kappa_1\left(a^5 + 10a^3b + 15ab^2\right),\\
\kappa_1^{(6)} &= \kappa_1\left(a^6 + 15a^4b + 45a^2b^2 + 15b^3\right),\\
&\vdots\\
\kappa^{(q)} &= \kappa_1 P_q(a, b).
\end{aligned}$$

where $P_q(a, b)$ is a polynomial in $a = i\psi_1'$ and $b = i\psi_1''$. We conclude that the error bound of the interpolated kernel error in (82) depends on the order of interpolation, ℓ, and the derivatives of the phase function, ψ_1' and ψ_1''. Because $|\kappa_1| = 1$,

$$|\kappa^{(q)}| = |P_q(a, b)| \leq P_q(|a|, |b|).$$

The last inequality follows from the triangle inequality because all coefficients in the polynomial $P_q(a, b)$ are positive. For all unit directions $\hat{\mathbf{e}}$, the coefficients are bounded by

$$|a| \leq C_a + C_s, \quad |b| \leq C_s.$$

□

5.4 3-D directional Chebyshev interpolation

The one-dimensional Chebyshev interpolation formula (71) is straightforward to generalize to smooth functions $g(x)$ defined on any finite interval $x \in [a,b]$, $-\infty < a < b < \infty$, by using the affine mappings $x = \Phi(\xi)$ and $\xi = \Phi^{-1}(x)$,

$$\Phi(\xi) = \frac{a+b}{2} + \frac{b-a}{2}\xi, \quad \Phi^{-1}(x) = \frac{2x-(a+b)}{b-a}. \tag{83}$$

The corresponding Chebyshev interpolant is defined by

$$g_\ell(x) = \sum_{m=1}^{\ell} s_\ell(x, \bar{x}_m) g(\bar{x}_m), \quad x \in [a,b], \tag{84}$$

$$s_\ell(x, \bar{x}_m) = \sigma_\ell(\Phi^{-1}(x), \bar{\xi}_m), \quad \bar{x}_m = \Phi(\bar{\xi}_m). \tag{85}$$

An interpolant of a function of a three-dimensional variable, $F(\mathbf{x})$, where $\mathbf{x} = (x_1, x_2, x_3)$ with $x_k \in [a_k, b_k]$ for $k = 1, 2, 3$, can be constructed as a tensor product of one-dimensional interpolants. For simplicity we assume that the interpolation order is the same in all directions. We introduce the multi-index $\mathbf{m} = (m_1, m_2, m_3)$ and $L = (\ell, \ell, \ell)$. The three-dimensional interpolant can then be written

$$F_\ell(\mathbf{x}) = \sum_{\mathbf{m}=1}^{L} S_\ell(\mathbf{x}, \bar{\mathbf{x}}_\mathbf{m}) F(\bar{\mathbf{x}}_m), \quad \mathbf{x} \in [a_1, b_1] \times [a_2, b_2] \times [a_3, b_3], \tag{86}$$

$$S_\ell(\mathbf{x}, \bar{\mathbf{x}}_\mathbf{m}) = s_\ell^{(1)}(x_1, \bar{x}_{m_1}) s_\ell^{(2)}(x_2, \bar{x}_{m_2}) s_\ell^{(3)}(x_3, \bar{x}_{m_3}). \tag{87}$$

Here, $s_\ell^{(k)}$ corresponds to the interval $x_k \in [a_k, b_k]$ for $k = 1, 2, 3$. The three-dimensional interpolation formula is generalized to the directional kernel $K^u(\mathbf{x}, \mathbf{y})$ by first interpolating in $\mathbf{y}$ followed by interpolating in $\mathbf{x}$,

$$K_\ell^u(\mathbf{x}, \mathbf{y}) = \sum_{\mathbf{m}=1}^{L} S_\ell(\mathbf{x}, \bar{\mathbf{x}}_\mathbf{m}) \sum_{\mathbf{n}=1}^{L} S_\ell(\mathbf{y}, \bar{\mathbf{y}}_\mathbf{n}) K^u(\bar{\mathbf{x}}_\mathbf{m}, \bar{\mathbf{y}}_\mathbf{n}). \tag{88}$$

From the definition of the directional kernel (55) we have

$$K^u(\mathbf{x}, \mathbf{y}) = e^{+ik\hat{\mathbf{u}}\cdot(\mathbf{x}-\mathbf{y})} G(\mathbf{x}, \mathbf{y}). \tag{89}$$

By applying the same transformation to K_ℓ^u, we arrive at the directional interpolant of the Green's function for Helmholtz equation,

$$\begin{aligned} G_\ell^u(\mathbf{x}, \mathbf{y}) &= e^{-ik\hat{\mathbf{u}}\cdot(\mathbf{x}-\mathbf{y})} \sum_{\mathbf{m}=1}^{L} S_\ell(\mathbf{x}, \bar{\mathbf{x}}_\mathbf{m}) \sum_{\mathbf{n}=1}^{L} S_\ell(\mathbf{y}, \bar{\mathbf{y}}_\mathbf{n}) e^{+ik\hat{\mathbf{u}}\cdot(\bar{\mathbf{x}}_\mathbf{m}-\bar{\mathbf{y}}_\mathbf{n})} G(\bar{\mathbf{x}}_\mathbf{m}, \bar{\mathbf{y}}_\mathbf{n}) \\ &= \sum_{\mathbf{m}=1}^{L} S_\ell(\mathbf{x}, \bar{\mathbf{x}}_\mathbf{m}) e^{+ik\hat{\mathbf{u}}\cdot(\bar{\mathbf{x}}_\mathbf{m}-\mathbf{x})} \sum_{\mathbf{n}=1}^{L} S_\ell(\mathbf{y}, \bar{\mathbf{y}}_\mathbf{n}) e^{-ik\hat{\mathbf{u}}\cdot(\bar{\mathbf{y}}_\mathbf{n}-\mathbf{y})} G(\bar{\mathbf{x}}_\mathbf{m}, \bar{\mathbf{y}}_\mathbf{n}). \end{aligned} \tag{90}$$

By using the relation (89), we see that the absolute value of the interpolation error for G_ℓ^u,

$$|G_\ell^u(\mathbf{x},\mathbf{y}) - G(\mathbf{x},\mathbf{y})| = |e^{-ik\hat{\mathbf{u}}\cdot(\mathbf{x}-\mathbf{y})}\,(K_\ell^u(\mathbf{x},\mathbf{y}) - K^u(\mathbf{x},\mathbf{y}))\,| = |K_\ell^u(\mathbf{x},\mathbf{y}) - K^u(\mathbf{x},\mathbf{y})|,$$

equals the absolute value of the interpolation error for K_ℓ^u.

The structure of the three-dimensional directional kernel (88) is similar to the one-dimensional kernel $\kappa_1(\xi,\eta)$ defined in (75). We therefore expect the accuracy of the interpolant $G_\ell^u(\mathbf{x},\mathbf{y})$ to depend on the interpolation order, ℓ, and the values of the dimensionless coefficients C_a and C_s, defined in (78). We proceed by testing this assertion numerically. Similar to the MLFMA method, it is straightforward to verify that the relative error in the interpolated directional kernel (90) is invariant with respect to the length scale. Here set the length scale to equal the wave length, λ, which means that the scaled wave number is $k = 2\pi$.

To reduce the computational burden, let all sources and receiver locations be located in the plane $z = 0$. Furthermore, let the source cluster be a square with side length $w = d/\sqrt{2}$ centered at the origin. The receiver cluster is also a square with side length w, but the center is located at $\mathbf{c} = |\mathbf{c}|\hat{\mathbf{c}}$, with $\hat{\mathbf{c}} = (\cos(\varphi_0), \sin(\varphi_0), 0)$. We evaluate the directional kernel in the direction $\hat{\mathbf{u}} = (\cos(\varphi_0+\varphi_1), \sin(\varphi_0+\varphi_1), 0)$. We place a regular grid of points $\mathbf{x}_{i,j}$ with $(i,j) \in [1,25]^2$ over the source square and a similar grid of points $\mathbf{y}_{k,l}$ with $(k,l) \in [1,25]^2$ over the receiver square. Thereafter, the accuracy of $G_\ell^u(\mathbf{x}_{i,j},\mathbf{y}_{k,l})$ is evaluated for all combinations of the grid point indices (i,j) and (k,l).

We start by evaluating to what extent the scaling invariance in Lemma 1 also applies to the accuracy of the interpolated kernel $G_\ell^u(\mathbf{x},\mathbf{y})$. Given the diameter d of the source and receiver clusters, we specify the coefficient C_s in (78) and set the cluster separation to be

$$|\mathbf{c}| = \frac{kd^2}{C_s}. \tag{91}$$

Furthermore, we specify the coefficient C_a in (78) and choose the angle φ_1 such that

$$|\hat{\mathbf{u}} - \hat{\mathbf{c}}| = \frac{C_a}{kd}. \tag{92}$$

In Figure 20 we report the relative max-norm error in $G_\ell^u(\mathbf{x},\mathbf{y})$ for $1 \le d/\lambda \le 20$ when $C_s = 0.5$, $C_a = 1.0$, and $\varphi_0 = 0$, for interpolation orders $\ell = 5, 6, 7$. Clearly, the relative error is almost independent of the cluster size d under this scaling, except for small values of $d/\lambda < 3$. Recall that the remainder term in the phase angle in (57) is proportional to $d/|\mathbf{c}|$, because $kd^2/|\mathbf{c}| = C_s$ is constant. This also implies that $d/|\mathbf{c}| = C_s/(kd)$, tends to zero as d/λ increases, as is shown in the figure on the right. For these parameter values, the remainder term in the phase angle can clearly be ignored for $d/\lambda \ge 3$. On the right side of the figure we also illustrate how the angle φ_1 decreases as d/λ increases, due to the aperture condition (92).

In Figure 21 we report how the accuracy of the directional Chebyshev interpolation depends on C_s and ℓ, when $C_a = C_s$ and $d/\lambda = 5$. In agreement with the theoretical prediction in Lemma 3, we observe that the interpolation error tends to zero when $C_s =$

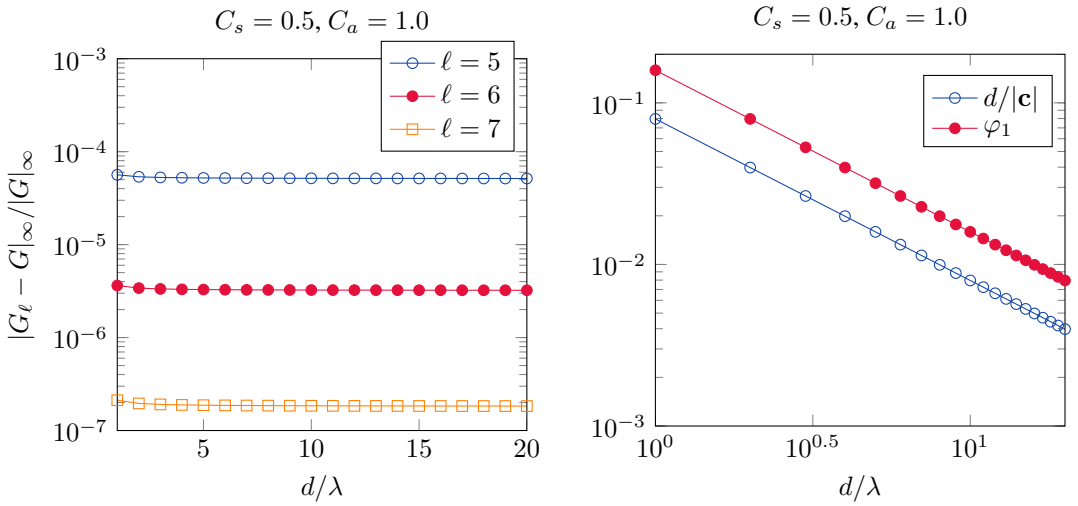

Figure 20: The relative max-error in the interpolated directional Chebyshev kernel for different interpolation orders (left). The angle φ_1 and $d/|\mathbf{c}|$ as function of d/λ (right).

$C_a \to 0$, for each fixed interpolation order. We also note that the interpolation error grows with $C_s = C_a$. For $C_s = C_a = 1$, a 5th order interpolant gives the interpolation error $\approx 10^{-4}$. For $C_s = C_a = 5$, a 10th order interpolant must be used to make the interpolation error smaller than 10^{-4}. For larger values of $C_s = C_a$, the accuracy deteriorates quickly as $C_a = C_s$ increases. From these results, it is clear that the order of interpolation can only be kept moderate if C_s and C_a are not larger than a some constant of unit order of magnitude.

Next, we fix $d/\lambda = 10$ and study how the relative error in G^u_ℓ depends on the coefficients C_a and C_s, see Figure 22. To obtain a relative error of 10^{-5} with $\ell = 5$ we have to use $C_a = 0.5$ and $C_s \leq 0.4$, or $C_s = 0.25$ and $C_a \leq 0.8$. If we increase the interpolation order to $\ell = 6$, the accuracy essentially improves by an order of magnitude, and the same accuracy can be obtained with larger values of C_a and C_s. By increasing the interpolation order to $\ell = 7$, the accuracy improves by another order of magnitude (data not shown to save space).

Remark 2. *For a fixed interpolation order, ℓ, the directional Chebyshev interpolation technique is only accurate when the values of C_a and C_s are of the order of magnitude 1, or smaller. For larger values of C_a and C_s, the interpolant can only be made accurate by using a very high interpolation order, which renders the method extremely expensive in several space dimensions.*

Remark 3. *Engquist and Ying [10] proved the existence of a low-rank approximation of the Green's function for Helmholtz equation under the assumption that the coefficients C_s and C_a in* (78) *are of the order of magnitude 1, or smaller.*

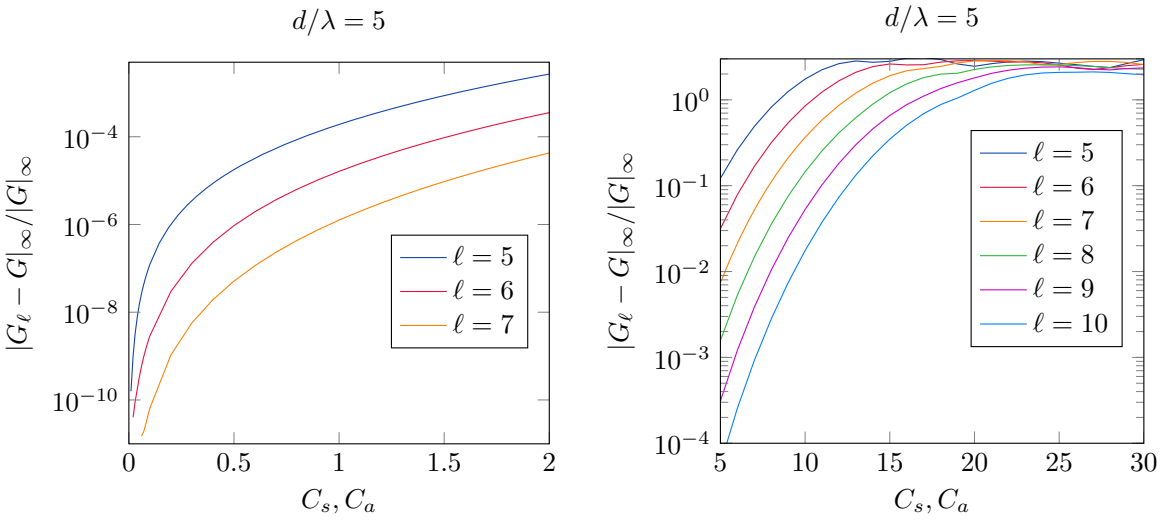

Figure 21: Relative max-error in the interpolated directional Chebyshev kernel for $d/\lambda = 5$ and $C_s = C_a$, as function of C_s for different interpolation orders, ℓ. Left: small values of C_s, Right: larger values of C_s.

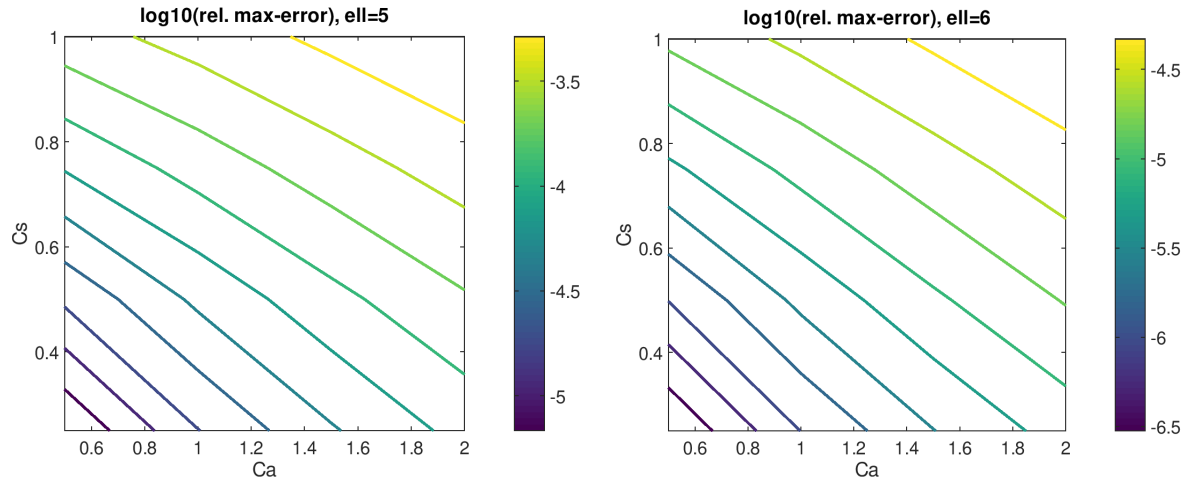

Figure 22: Relative max-error in the interpolated directional Chebyshev kernel (on a $\log_{10}$ scale) as function of C_a and C_s for interpolation orders $\ell = 5$ (left) and $\ell = 6$ (right).

5.5 Constructing the cluster decomposition

If the sources and receiver locations were separated sufficiently far from each other, we could place *all* sources in one cluster and *all* receiver locations in another. More specifically, let all sources be contained in a cluster of radius $D/2 \gg \lambda$ and let all receivers be located inside another cluster of the same radius. Furthermore, let the separation vector between the centers of the two clusters be $\mathbf{C}$.

In a table-top grating compressor, the distance between the first and second gratings is $L_{12} \approx 0.5$ m. The first grating is approximately square and has a side length of $W_1 \approx 11$ mm. The second grating has a rectangular extent of about $W_2 \times W_1$, where $W_2 \approx 120$ mm. The radius of a sphere enclosing the second grating is therefore $R \approx 60.25$ mm. Assuming the compressor is designed to operate in the infrared spectrum with wavelength $\lambda = 1.053 \cdot 10^{-6}$ m, the corresponding wave number is $k \approx 5.97 \cdot 10^6$ 1/m. By taking $|\mathbf{C}| = L_{12}$ and $D = 2R$, we get

$$k|\mathbf{C}| \approx 2.98 \cdot 10^6, \quad kD \approx 7.19 \cdot 10^5.$$

In terms of the dimensionless coefficient C_s in (78),

$$C_s = \frac{kD^2}{|\mathbf{C}|} = \frac{(kD)^2}{k|\mathbf{C}|} \approx 1.73 \cdot 10^5.$$

From the theory in Section 5.3 and the numerical experiments in Section 5.4 we know that the directional Chebyshev interpolant can only be accurate if C_s is smaller than some order-of-magnitude 1 constant. We conclude that the directional interpolant G_ℓ^u can *not* provide an accurate approximation with all sources in one cluster and all receiver locations in another cluster.

To proceed, we start by noting that the accuracy of the directional interpolant G_ℓ^u is controlled by the interpolation order, ℓ, and the dimensionless coefficients C_a and C_s in (78). For a fixed interpolation order ℓ, the accuracy improves as C_s and C_a get smaller. Consider a cluster of sources and a cluster of receiver locations and define the max-norm of the relative interpolation error in G_ℓ^u by

$$\varepsilon = \frac{|G_\ell^u(\mathbf{x},\mathbf{y}) - G(\mathbf{x},\mathbf{y})|_\infty}{|G(\mathbf{x},\mathbf{y})|_\infty}, \quad |\mathbf{x} - \mathbf{c}_x| \le \frac{d}{2}, \quad |\mathbf{y} - \mathbf{c}_y| \le \frac{d}{2}, \quad \mathbf{c} = \mathbf{c}_x - \mathbf{c}_y. \tag{93}$$

The results in Sections 5.3-5.4 show that for a fixed interpolation order, ℓ, the interpolation error increases as either C_s or C_a increases. When the sources and receiver locations are divided into several clusters and the Chebyshev interpolation in G_ℓ^u is performed in several directions, the values of the dimensionless coefficients C_s and C_a will vary. To guarantee that the interpolation error does not exceed a prescribed tolerance, ε, for any combination of source and receiver clusters, we introduce upper threshold values for C_s and C_a,

$$\frac{kd^2}{|\mathbf{c}|} =: C_s \le \mathcal{A}_s, \tag{94}$$

$$kd|\hat{\mathbf{u}} - \hat{\mathbf{c}}| =: C_a \le \mathcal{A}_a. \tag{95}$$

The first inequality is called the parabolic separation condition. The second inequality is called the aperture condition. For a fixed interpolation order ℓ, the threshold values $\mathcal{A}_s$ and $\mathcal{A}_a$ must be chosen such that the given interpolation accuracy, $\varepsilon > 0$, is obtained. When the interpolation order (ℓ) is small, the threshold values $\mathcal{A}_a$ and $\mathcal{A}_s$ must be chosen very small to obtain a very accurate interpolant. A more efficient way of making the interpolant very accurate is to instead increase ℓ, which enables larger values of $\mathcal{A}_a$ and $\mathcal{A}_s$ to be used. We will numerically investigate the tuning of these parameters in Section 6.

In practice, we use the separation condition (94) to determine the maximum diameter d_0 of the source and receiver clusters. For example, using the table-top compressor dimensions, we get

$$kd_0 \leq \sqrt{\mathcal{A}_s k|\mathbf{C}|} \approx 1727, \quad d_0 \leq 2.89 \cdot 10^{-4} \text{ m},$$

with $\mathcal{A}_s = 1$. Thus, the first and second gratings must be divided into clusters of diameter $d \leq d_0$. Because the height of the grating is less than a wave length, we can treat the clusters as being two-dimensional. The corresponding side length of each cluster becomes $w_0 = d_0/\sqrt{2} \approx 2{\cdot}10^{-4}$ m. As a result, the sources on the first grating must be grouped into $W_1/w_0 \approx 55$ clusters in each direction for a total of 3025 source clusters. The receivers on the second grating need to be divided into $W_2/w_0 \approx 600$ clusters along the longer side of the grating and 55 clusters along the shorter side, for a total of 33,000 clusters. In this case, the aperture condition (95) implies that

$$|\hat{\mathbf{u}} - \hat{\mathbf{c}}| \leq \frac{\mathcal{A}_a}{1727},$$

where $\mathcal{A}_a \approx 1$. There must be at least one direction $\hat{\mathbf{u}}$ that satisfies this condition for each pair of source and receiver clusters.

Because the surface of each grating is close to planar, the minimum distance between two gratings, or a grating and an observation plane, can easily be found by evaluating the distance between a few points of each grating. For a general configuration, let the smallest separation be C, see Figure 23. We then use the parabolic separation condition (94) to calculate the maximum cluster diameter d_0, corresponding to a maximum side length of $w_0 = d_0/\sqrt{2}$. A grating with side lengths L_x by L_y must therefore be divided into N_1 by N_2 (approximately square) clusters, with

$$N_1 = \left\lceil \frac{L_x}{w_0} \right\rceil, \quad N_2 = \left\lceil \frac{L_y}{w_0} \right\rceil, \quad w_0 = \sqrt{\frac{\mathcal{A}_s C}{2k}}.$$

5.6 Choosing the discrete directions

It is convenient to use spherical coordinates to quantify the range of directions between source and receiver clusters. As before, let $\mathbf{c}_y$ and $\mathbf{c}_x$ be the center locations of a source and a receiver cluster, respectively. By taking the polar axis to coincide with the second

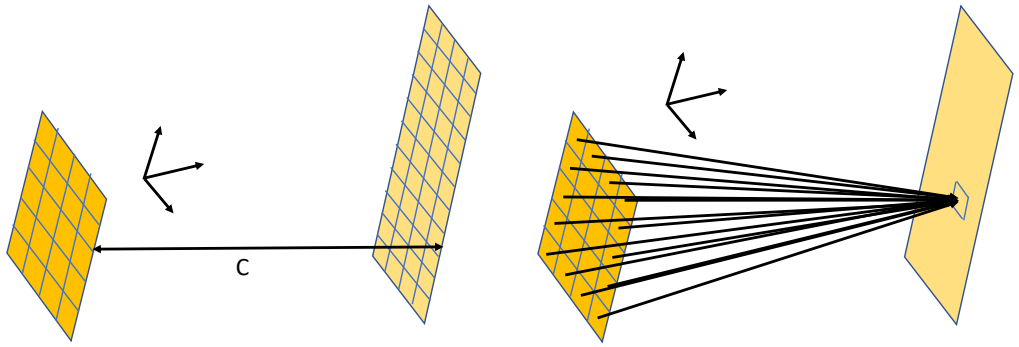

Figure 23: Left: the minimum separation distance between the gratings determines the size of the clusters. Boundaries between cluster are indicated by blue lines. Right: the fields in each receiver follows as a sum over the contributions from all source clusters. Each contribution uses the discrete direction $\hat{\mathbf{u}}_\delta$ that minimizes $|\hat{\mathbf{u}}_\delta - \hat{\mathbf{c}}|$.

Cartesian coordinate direction,

$$\mathbf{c}_x - \mathbf{c}_y = \chi \hat{\mathbf{c}}, \quad \chi = |\mathbf{c}_x - \mathbf{c}_y|, \quad \hat{\mathbf{c}} = \begin{bmatrix} \sin\theta \sin\phi \\ \cos\theta \\ \sin\theta \cos\phi \end{bmatrix}, \quad \phi \in [0, 2\pi), \;\; \theta \in [0, \pi]. \tag{96}$$

The angle ϕ is called the azimuth and θ is the polar angle. Because the gratings are almost planar, we can calculate the range in angles by only evaluating the polar and azimuth angles for the 16 combinations of corners locations of the two gratings. This leads to

$$\phi \in [\phi_{min}, \phi_{max}], \quad \theta \in [\theta_{min}, \theta_{max}]. \tag{97}$$

Note that the variation in the polar angle normally is small and fluctuates around $\pi/2$. In particular, it is always bounded away from the polar singularities.

Let the discrete angles $(\phi_\delta, \theta_\delta)$ correspond to the direction

$$\hat{\mathbf{u}}_\delta = \begin{bmatrix} \sin\theta_\delta \sin\phi_\delta \\ \cos\theta_\delta \\ \sin\theta_\delta \cos\phi_\delta \end{bmatrix},$$

and let (ϕ, θ) be the angles corresponding to $\hat{\mathbf{c}}$. The aperture condition (95) prescribes a bound on $|\hat{\mathbf{c}} - \hat{\mathbf{u}}_\delta|$. Trigonometric identities give

$$\begin{aligned} |\hat{\mathbf{c}} - \hat{\mathbf{u}}_\delta|^2 &= (\sin\theta \sin\phi - \sin\theta_\delta \sin\phi_\delta)^2 + (\cos\theta - \cos\theta_\delta)^2 + (\sin\theta \cos\phi - \sin\theta_\delta \cos\phi_\delta)^2 \\ &= 2 - 2\cos\theta \cos\theta_\delta - 2\sin\theta \sin\theta_\delta \cos(\phi - \phi_\delta) \end{aligned}$$

By introducing $\Delta\phi = (\phi - \phi_\delta)/2$ and $\Delta\theta = (\theta - \theta_\delta)/2$,

$$\begin{aligned}|\hat{\mathbf{c}} - \hat{\mathbf{u}}_\delta|^2 &= 2 - 2\cos\theta\cos\theta_\delta(\cos^2\Delta\phi + \sin^2\Delta\phi) - 2\sin\theta\sin\theta_\delta(\cos^2\Delta\phi - \sin^2\Delta\phi) \\ &= 2 - 2\cos^2\Delta\phi\cos(\theta - \theta_\delta) - 2\sin^2\Delta\phi\cos(\theta + \theta_\delta) \\ &= 4\cos^2\Delta\phi\sin^2\Delta\theta + 4\sin^2\Delta\phi\sin^2\left(\frac{\theta + \theta_\delta}{2}\right).\end{aligned}$$

Because $\sin^2((\theta + \theta_\delta)/2) \leq 1$,

$$|\hat{\mathbf{c}} - \hat{\mathbf{u}}_\delta|^2 \leq 4\left(\cos^2\Delta\phi\sin^2\Delta\theta + \sin^2\Delta\phi\right) = 4\left(1 - \cos^2\Delta\phi\cos^2\Delta\theta\right).$$

By assuming $\Delta\theta = \Delta\phi$, the aperture condition (95) gives,

$$4\left(1 - \cos^4\Delta\phi\right) \leq \frac{\mathcal{A}_a^2}{(kd)^2}.$$

Hence, by defining

$$\Delta\theta_{kd} = \Delta\phi_{kd} = \cos^{-1}\left(\left(1 - \frac{\mathcal{A}_a^2}{4(kd)^2}\right)^{1/4}\right) \approx \frac{1}{2\sqrt{2}}\frac{\mathcal{A}_a}{kd}, \tag{98}$$

we satisfy the aperture condition if

$$|\phi - \phi_\delta| \leq 2\Delta\theta_{kd}, \quad |\theta - \theta_\delta| \leq 2\Delta\theta_{kd}. \tag{99}$$

The approximation on the right hand side of (98) holds for $\mathcal{A}_a/kd \ll 1$.

Given $\Delta\theta_{kd}$ and the ranges of azimuth and polar angles (97), we discretize the directions on a regular $N_\theta \times N_\phi$ grid. The angle condition (99) is satisfied by the discrete directions

$$\theta_{\delta_1} = \theta_{min} + 4(\delta_1 - 1/2)\Delta\theta_{kd}, \quad \delta_1 = 1, 2, \ldots, N_\theta, \tag{100}$$

$$\phi_{\delta_2} = \phi_{min} + 4(\delta_2 - 1/2)\Delta\theta_{kd}, \quad \delta_2 = 1, 2, \ldots, N_\phi, \tag{101}$$

where

$$N_\theta = \left\lceil \frac{\theta_{max} - \theta_{min}}{4\Delta\theta_{kd}} \right\rceil, \quad N_\phi = \left\lceil \frac{\phi_{max} - \phi_{min}}{4\Delta\theta_{kd}} \right\rceil. \tag{102}$$

Note that $\delta = (\delta_1, \delta_2)$ is a multi-index. Thus, the Cartesian components of the $N_\theta \times N_\phi$ discrete directions become

$$\hat{\mathbf{u}}_\delta = \begin{bmatrix} \sin\theta_{\delta_1}\sin\phi_{\delta_2} \\ \cos\theta_{\delta_1} \\ \sin\theta_{\delta_1}\cos\phi_{\delta_2} \end{bmatrix}, \quad \delta = (\delta_1, \delta_2), \quad \delta_1 \in [1, N_\theta], \quad \delta_2 \in [1, N_\phi]. \tag{103}$$

Using the above construction, at least one of the $N_{dir} = N_\theta \times N_\phi$ discrete directions $\hat{\mathbf{u}}_\delta$ will satisfy the aperture condition (95) for the separation vector $\mathbf{c} = \mathbf{c}_x - \mathbf{c}_y$, corresponding to each pair of source and receiver clusters.

5.7 Single-level directional summation

We consider evaluating the magnetic field due to a surface current $\mathbf{J}^s(\mathbf{y})$ over the grating surface $\mathbf{y} \in \Gamma_1$. The magnetic field is evaluated at a location $\mathbf{x}_i \in \Gamma_2$, where Γ_2 is the surface of the next grating, or an observation surface. Let the quadrilateral faces (quads) on Γ_1 be grouped into N_{sc} source clusters, denoted by $\mathfrak{S}_s$, with $s = 1, 2, \ldots, N_{sc}$. In a similar way, the quads on Γ_2 are grouped into M_{rc} receiver clusters $\mathfrak{R}_r$, with $r = 1, 2, \ldots M_{rc}$ (see Figure 23). In particular, we consider $\mathfrak{S}_s$ and $\mathfrak{R}_r$ to hold the index ranges for the quads in the corresponding source and receiver clusters.

The formula for the discretized scattered magnetic field (49) can be decomposed into its contributions from each source cluster[2],

$$\mathbf{H}(\mathbf{x}_i) = \sum_{s=1}^{N_{sc}} \mathbf{H}^s(\mathbf{x}_i), \quad \mathbf{H}^s(\mathbf{x}_i) = \sum_{q \in \mathfrak{S}_s} \sum_{p=1}^{P} G(\mathbf{x}_i, \mathbf{y}_{q,p}) \mathbf{A}_{q,p}. \tag{104}$$

The coefficient $\mathbf{A}_{q,p} \in \mathbb{C}^3$ follows by extracting the coefficient for each source location $\mathbf{y}_{q,p}$, within the quad q, from the term $I_q^{(3)}$ in (50). Here, P is the number of point sources per quad.

The single-level directional summation method uses the directional interpolant $G_\ell^u(\mathbf{x}, \mathbf{y})$ from (90) to approximate $G(\mathbf{x}, \mathbf{y})$ in the sum (104). The interpolation order, ℓ, is assumed to be constant throughout the algorithm. Henceforth we denote the directional interpolant, associated with the direction $\hat{\mathbf{u}}_\delta$, by G^δ. Furthermore, the notation for the interpolation function S_ℓ in (87) is modified to indicate to which cluster it belongs. We therefore replace the interpolation order in the subscript by the cluster index r, $S_r(\mathbf{x}, \bar{\mathbf{x}}_m)$.

Let $\mathbf{x}_i$ be located in the receiver cluster $\mathfrak{R}_r$. After reordering the terms in (104),

$$\mathbf{H}(\mathbf{x}_i) \approx \widetilde{\mathbf{H}}_r(\mathbf{x}_i) = \sum_{s=1}^{N_{sc}} e^{-ik\hat{\mathbf{u}}_\delta \cdot \mathbf{x}_i} \sum_{\mathbf{m}=1}^{L} S_r(\mathbf{x}_i, \bar{\mathbf{x}}_\mathbf{m}) e^{+ik\hat{\mathbf{u}}_\delta \cdot \bar{\mathbf{x}}_\mathbf{m}} \sum_{\mathbf{n}=1}^{L} G(\bar{\mathbf{x}}_\mathbf{m}, \bar{\mathbf{y}}_\mathbf{n}) \bar{\mathbf{A}}_{s,\mathbf{n}}^\delta, \tag{105}$$

$$\bar{\mathbf{A}}_{s,\mathbf{n}}^\delta = e^{-ik\hat{\mathbf{u}}_\delta \cdot \bar{\mathbf{y}}_\mathbf{n}} \sum_{q \in \mathfrak{S}_s} \sum_{p=1}^{P} S_s(\mathbf{y}_{q,p}, \bar{\mathbf{y}}_\mathbf{n}) e^{ik\hat{\mathbf{u}}_\delta \cdot \mathbf{y}_{q,p}} \mathbf{A}_{q,p}, \quad \delta \in [1, N_{dir}], \quad s \in [1, N_{sc}]. \tag{106}$$

Here, $\bar{\mathbf{x}}_m$ is a Chebyshev node point in the receiver cluster $\mathfrak{R}_r$ and $\bar{\mathbf{y}}_n$ is a Chebyshev node point in source cluster $\mathfrak{S}_s$. The interpolation weights in the receiver and source clusters are S_r and S_s, respectively. The quantity $\bar{\mathbf{A}}_{s,\mathbf{n}}^\delta$ is the anterpolated source strength at $\bar{\mathbf{y}}_\mathbf{n}$, in the direction $\hat{\mathbf{u}}_\delta$. The direction $\hat{\mathbf{u}}_\delta$ is chosen to minimize $|\hat{\mathbf{u}}_\delta - \hat{\mathbf{c}}|$, where $\hat{\mathbf{c}}$ is the unit separation direction between the source cluster $\mathfrak{S}_s$ and the receiver cluster $\mathfrak{R}_r$. The index of the direction satisfies $\delta = D(r, s)$, where

$$D(r, s) = \arg\min_q |\hat{\mathbf{u}}_q - \hat{\mathbf{c}}(r, s)|, \qquad \hat{\mathbf{c}}(r, s) = \frac{\mathbf{c}_x^r - \mathbf{c}_y^s}{|\mathbf{c}_x^r - \mathbf{c}_y^s|}.$$

[2]In this section, we simplify the notation by dropping the subscript on the scattered magnetic field and denote $\mathbf{H} = \mathbf{H}_{sc}$.

The individual steps for evaluating the expression for $\widetilde{\mathbf{H}}_r$ can be made clearer by further decomposing the sums in (105),

$$\widetilde{\mathbf{H}}_r(\mathbf{x}_i) = \sum_{s=1}^{N_{sc}} e^{-ik\hat{\mathbf{u}}_\delta \cdot \mathbf{x}_i} \sum_{\mathbf{m}=1}^{L} S_r(\mathbf{x}_i, \bar{\mathbf{x}}_\mathbf{m}) e^{+ik\hat{\mathbf{u}}_\delta \cdot \bar{\mathbf{x}}_\mathbf{m}} \bar{\mathbf{H}}^s_{r,\mathbf{m}}, \quad \delta = D(r,s), \quad r \in [1, M_{rc}] \tag{107}$$

$$\bar{\mathbf{H}}^s_{r,\mathbf{m}} = \sum_{\mathbf{n}=1}^{L} G(\bar{\mathbf{x}}_\mathbf{m}, \bar{\mathbf{y}}_\mathbf{n}) \bar{\mathbf{A}}^\delta_{s,\mathbf{n}}, \quad \mathbf{m} \in [1, L], \quad s \in [1, N_{sc}], \quad r \in [1, M_{rc}]. \tag{108}$$

We call $\bar{\mathbf{H}}^s_{r,\mathbf{m}}$ the directional field values at the Chebyshev node points in the receiver cluster, corresponding to the direction $\hat{\mathbf{u}}_\delta$, where $\delta = D(r,s)$.

To evaluate the magnetic field for all locations in the receiver cluster $\mathfrak{R}_r$, we first apply (106) to calculate the directional anterpolated source strengths $\bar{\mathbf{A}}^\delta_{s,\mathbf{n}}$ at each Chebyshev node point $\bar{\mathbf{y}}_n$ in the the direction $\delta = D(r,s)$ for all source clusters s. Secondly, we use (108) to calculate the directional field values $\bar{\mathbf{H}}^s_{r,\mathbf{m}}$ at each Chebyshev node point in the receiver cluster. This calculation is called the transfer operation. Thirdly, the directional field values at each receiver location $\mathbf{x}_i$ are obtained from the interpolation formula (107), which aggregates the directional terms from each receiver cluster. For a fixed receiver cluster, $\mathbf{x}_i \in \mathfrak{R}_r$, note that the direction ($\hat{\mathbf{u}}_\delta$) only depends on the source cluster, $\mathfrak{S}_s$.

To compare the operational counts between explicitly evaluating (104) and using the directional summation formulas, assume that there are N_{sc} source clusters, each holding N_{qd} quads with P point sources per quad. Furthermore, assume that there are M_{rc} receiver clusters, each holding M_{qd} quads, and that the field is evaluated at Q locations per quad. There are in total $N_{tot} = N_{sc}N_{qd}P$ sources and $M_{tot} = M_{rc}M_{qd}Q$ receivers. Explicitly evaluating (104) thus requires

$$\mathcal{O}(N_{tot}M_{tot}) = \mathcal{O}((N_{qd}PM_{qd}Q)N_{sc}M_{rc})$$

operations.

The number of Chebyshev node points equals $|L| = \ell^3$ in each source and receiver cluster. To evaluate (106) for the anterpolated source strengths in all source clusters and in all directions requires $\mathcal{O}(N_{dir}N_{sc}N_{qd}P\ell^3)$ operations. However, not all directions are needed for all combinations of source and receiver clusters, so the operational count can be reduced to $\mathcal{O}(M_{rc}N_{sc}N_{qd}P\ell^3)$ Calculating the directional field values at the Chebyshev node points in all receiver clusters using (108) requires $\mathcal{O}(N_{sc}M_{rc}\ell^6)$ operations. The interpolation to all receiver locations in one cluster using (107) requires $\mathcal{O}(N_{sc}M_{qd}Q\ell^3)$ operations; repeating that step for all M_{rc} clusters leads to $\mathcal{O}(M_{rc}N_{sc}M_{qd}Q\ell^3)$ operations for the interpolation step. The total number of operations for the single-level directional summation algorithm therefore becomes

$$\mathcal{O}((N_{qd}P\ell^3 + \ell^6 + M_{qd}Q\ell^3)N_{sc}M_{rc}) = \mathcal{O}\left(N_{tot}\frac{M_{tot}\ell^3}{M_{qd}Q}\right) + \mathcal{O}\left(M_{tot}\frac{N_{tot}\ell^3}{N_{qd}P}\right) + \mathcal{O}\left(\frac{N_{tot}\ell^3}{N_{qd}P}\,\frac{M_{tot}\ell^3}{M_{qd}Q}\right). \tag{109}$$

We conclude that the single level directional interpolation method can only be faster than the explicit summation method if the number of sources per quad, $N_{qd}P$, and the number of receivers per quad, $M_{qd}Q$ are sufficiently large compared to ℓ^3.

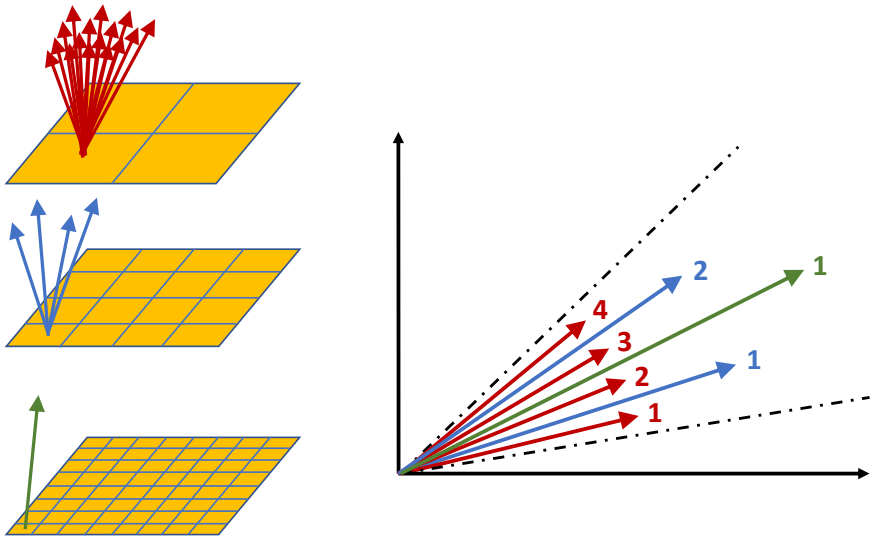

Figure 24: Left: the discrete directions in a source or receiver tree with three levels ($\nu = 0, 1, 2$). Right: the discrete directions in ϕ (or θ) are constructed to divide the aperture in equal angle increments. Here, $\nu = 0$ is shown in red, $\nu = 1$ in blue, and $\nu = 2$ in green.

5.8 The multi-level directional algorithm

The number of discrete directions, $\hat{\mathbf{u}}_\delta$, with $\delta \in [1, N_\theta] \times [1, N_\phi]$ in (103) can be made smaller by increasing the angle $\Delta\theta_{kd}$ in (98), which is possible by making the cluster size smaller than the maximum value (d_0) allowed by the separation condition (94). Reducing the cluster size, while keeping the separation distance fixed, only makes the dimensionless separation coefficient C_s smaller; the parabolic separation condition (94) is therefore satisfied for all $d \leq d_0$. We can organize the source and receiver clusters in a tree structure, where the root level ($\nu = 0$) is given by the single level cluster decomposition, described above. Given level ν in the tree, we construct level $\nu + 1$ by subdividing each source and receiver cluster into four child clusters of approximately equal size. For every subdivision, the diameter of the clusters become a factor of two smaller. This implies that the angle $\Delta\theta_{kd}$ approximately doubles, which halves the number of discrete directions in both the azimutal and polar directions (θ and ϕ), resulting in approximately four times fewer directions, see Figure 24. The subdivision is stopped once the aperture condition (95) is satisfied for a single direction. We use the same algorithm as in Section 5.6 to select the set of discrete directions $\hat{\mathbf{u}}_\delta^\nu$ on each level ν, based on the local cluster size on that level. If d_0 is the cluster diameter on the root level $\nu = 0$, the cluster diameter on level $\nu > 0$ becomes $d_\nu = d_0/2^\nu$. At level ν in the tree, the aperture condition (98) gives

$$\Delta\theta_{kd_\nu} = \cos^{-1}\left(\left(1 - \frac{\mathcal{A}_a^2}{4(kd_\nu)^2}\right)^{1/4}\right) \approx \frac{1}{2\sqrt{2}}\frac{\mathcal{A}_a}{kd_\nu}.$$

From (102), the leaf level in the tree, $\nu = B$ is determined by the smallest ν for which

$$\Delta\theta_{kd_\nu} \geq \frac{1}{4}\max(\theta_{max} - \theta_{min}, \phi_{max} - \phi_{min}) =: \frac{a_{max}}{4}.$$

By combining the last two equations,

$$B \approx \left\lceil \log_2 \left(\frac{a_{max} k d_0}{\sqrt{2}\mathcal{A}_a} \right) \right\rceil. \tag{110}$$

The multi-level directional interpolation algorithm was only partly described by Messner et al. [19], and we proceed by describing it in more detail.

5.8.1 Two levels

We begin by considering a tree with two levels, e.g., the top two levels in Figure 24. Let the receiver location $\mathbf{x}_i$ be included in the receiver cluster $\mathfrak{R}_r^{\nu+1}$ on level $\nu+1$, which is a child of the receiver cluster $\mathfrak{R}_{r'}^{\nu}$ on level ν. The indices of the clusters on level $\nu+1$, which are children of the parent cluster s' on level ν, are denoted by the set

$$s \in \mathfrak{C}^\nu(s').$$

We want to calculate the interaction with the four source clusters $\mathfrak{S}_s^{\nu+1}$ on level $\nu+1$, with $s \in \mathfrak{C}^\nu(s')$.

We assume that the parent clusters $\mathfrak{R}_{r'}^{\nu}$ and $\mathfrak{S}_{s'}^{\nu}$ satisfy the aperture condition on level ν, based on the direction $\hat{\mathbf{u}}' = \hat{\mathbf{u}}_{\delta'}^{\nu}$. On level $\nu+1$, let the direction $\hat{\mathbf{u}} = \hat{\mathbf{u}}_{\delta}^{\nu+1}$ satisfy the aperture condition between the receiver cluster $\mathfrak{R}_r^{\nu+1}$ and the child source clusters $\mathfrak{S}_s^{\nu+1}$, with $s \in \mathfrak{C}^\nu(s')$. The reason all four child source clusters can use the same direction is that the cluster diameter is a factor of two smaller on the child level, so the difference between the directions $\hat{\mathbf{u}}$ and $\hat{\mathbf{c}}$ can be a factor of two larger, while still honoring the aperture condition (95).

We start by considering how the directional kernel $K^{u'}(\mathbf{x}, \mathbf{y})$, corresponding to the direction $\hat{\mathbf{u}}'$ on level ν, can be interpolated from the Chebyshev node points[3] $\bar{\mathbf{y}}_\sigma^\nu$ in the source cluster $\mathfrak{S}_{s'}^{\nu}$ on that level. Let $\bar{\mathbf{y}}_n^{\nu+1}$ be a Chebyshev node point in the child source cluster $\mathfrak{S}_s^{\nu+1}$. We have

$$K^{u'}(\mathbf{x}, \bar{\mathbf{y}}_n^{\nu+1}) \approx \sum_{\sigma=1}^{L} K^{u'}(\mathbf{x}, \bar{\mathbf{y}}_\sigma^\nu) S_{s'}^\nu(\bar{\mathbf{y}}_n^{\nu+1}, \bar{\mathbf{y}}_\sigma^\nu),$$

where $S_{s'}^\nu$ holds the interpolation coefficients for the source cluster $\mathfrak{S}_{s'}^{\nu}$. Because

$$K^{u'}(\mathbf{x}, \mathbf{y}) = G(\mathbf{x}, \mathbf{y}) e(\hat{\mathbf{u}}' \cdot (\mathbf{x} - \mathbf{y})), \quad e(\alpha) := e^{ik\alpha}, \tag{111}$$

we get

$$G(\mathbf{x}, \bar{\mathbf{y}}_n^{\nu+1}) \approx e(\hat{\mathbf{u}}' \cdot \bar{\mathbf{y}}_n^{\nu+1}) \sum_{\sigma=1}^{L} e(-\hat{\mathbf{u}}' \cdot \bar{\mathbf{y}}_\sigma^\nu) G(\mathbf{x}, \bar{\mathbf{y}}_\sigma^\nu) S_{s'}^\nu(\bar{\mathbf{y}}_n^{\nu+1}, \bar{\mathbf{y}}_\sigma^\nu). \tag{112}$$

[3] In this section, we drop the bold-face notation on the multi-index for a Chebyshev node point.

On level $\nu+1$, we can derive a corresponding formula using the node points $\bar{\mathbf{y}}_n^{\nu+1}$ to interpolate to the source locations $\mathbf{y}_{q,p}$, using the direction $\hat{\mathbf{u}} = \hat{\mathbf{u}}_\delta^{\nu+1}$,

$$G(\mathbf{x},\mathbf{y}_{q,p}) \approx e(\hat{\mathbf{u}}\cdot\mathbf{y}_{q,p}) \sum_{n=1}^{L} e(-\hat{\mathbf{u}}\cdot\bar{\mathbf{y}}_n^{\nu+1}) S_s^{\nu+1}(\mathbf{y}_{q,p},\bar{\mathbf{y}}_n^{\nu+1}) G(\mathbf{x},\bar{\mathbf{y}}_n^{\nu+1})$$
$$= e(\hat{\mathbf{u}}\cdot\mathbf{y}_{q,p}) \sum_{n=1}^{L} e(-\hat{\mathbf{u}}\cdot\bar{\mathbf{y}}_n^{\nu+1}) S_s^{\nu+1}(\mathbf{y}_{q,p},\bar{\mathbf{y}}_n^{\nu+1}) e(\hat{\mathbf{u}}'\cdot\bar{\mathbf{y}}_n^{\nu+1}) \sum_{\sigma=1}^{L} G(\mathbf{x},\bar{\mathbf{y}}_\sigma^{\nu}) e(-\hat{\mathbf{u}}'\cdot\bar{\mathbf{y}}_\sigma^{\nu}) S_{s'}^{\nu}(\bar{\mathbf{y}}_n^{\nu+1},\bar{\mathbf{y}}_\sigma^{\nu}), \tag{113}$$

where we assumed that $\mathbf{y}_{q,p}$ belongs to source cluster $\mathfrak{S}_s^{\nu+1}$.

The contributions to the field value $\mathbf{H}(\mathbf{x}_i)$, where $\mathbf{x}_i \in \mathfrak{R}_{r'}^{\nu}$, from all sources in the parent cluster $\mathfrak{S}_{s'}^{\nu}$ follows from (104).

$$\mathbf{H}_{r'}^{s'}(\mathbf{x}_i) = \sum_{s\in\mathfrak{C}^\nu(s')} \sum_{q\in\mathfrak{S}_s^{\nu+1}} \sum_{p=1}^{P} G(\mathbf{x}_i,\mathbf{y}_{q,p})\mathbf{A}_{q,p}$$

By inserting the two-level interpolant from (113) in the above expression, we get the approximation

$$\mathbf{H}_{r'}^{s'}(\mathbf{x}_i) \approx \widetilde{\mathbf{H}}_{r'}^{\delta',\nu}(\mathbf{x}_i) = \sum_{s\in\mathfrak{C}^\nu(s')} \sum_{q\in\mathfrak{S}_s^{\nu+1}} \sum_{p=1}^{P}\sum_{n=1}^{L}\sum_{\sigma=1}^{L}$$
$$G(\mathbf{x}_i,\bar{\mathbf{y}}_\sigma^{\nu}) e(-\hat{\mathbf{u}}'\cdot\bar{\mathbf{y}}_\sigma^{\nu}) S_{s'}^{\nu}(\bar{\mathbf{y}}_n^{\nu+1},\bar{\mathbf{y}}_\sigma^{\nu}) e(\hat{\mathbf{u}}'\cdot\bar{\mathbf{y}}_n^{\nu+1}) e(-\hat{\mathbf{u}}\cdot\bar{\mathbf{y}}_n^{\nu+1}) S_s^{\nu+1}(\mathbf{y}_{q,p},\bar{\mathbf{y}}_n^{\nu+1}) e(\hat{\mathbf{u}}\cdot\mathbf{y}_{q,p})\mathbf{A}_{q,p}.$$

After reordering the sums,

$$\widetilde{\mathbf{H}}_{r'}^{\delta',\nu}(\mathbf{x}_i) = \sum_{\sigma=1}^{L} G(\mathbf{x}_i,\bar{\mathbf{y}}_\sigma^{\nu}) e(-\hat{\mathbf{u}}'\cdot\bar{\mathbf{y}}_\sigma^{\nu}) \sum_{s\in\mathfrak{C}^\nu(s')}\sum_{n=1}^{L} S_{s'}^{\nu}(\bar{\mathbf{y}}_n^{\nu+1},\bar{\mathbf{y}}_\sigma^{\nu}) e(\hat{\mathbf{u}}'\cdot\bar{\mathbf{y}}_n^{\nu+1})$$
$$e(-\hat{\mathbf{u}}\cdot\bar{\mathbf{y}}_n^{\nu+1}) \sum_{q\in\mathfrak{S}_s^{\nu+1}}\sum_{p=1}^{P} S_s^{\nu+1}(\mathbf{y}_{q,p},\bar{\mathbf{y}}_n^{\nu+1}) e(\hat{\mathbf{u}}\cdot\mathbf{y}_{q,p})\mathbf{A}_{q,p}. \tag{114}$$

Note that the Chebyshev node points on level $\nu+1$, $\bar{\mathbf{y}}_n^{\nu+1}$, are inside the cluster $\mathfrak{S}_s^{\nu+1}$. Similarly, $\bar{\mathbf{y}}_\sigma^{\nu}$ is inside the cluster $\mathfrak{S}_{s'}^{\nu}$.

We can now generalize the anterpolation step to the two-level case. As in the single level algorithm, we first calculate the anterpolated sources on level $\nu+1$ at $\bar{\mathbf{y}}_n^{\nu+1}$ (using the direction $\hat{\mathbf{u}}$). The expression for the anterpolated sources on level $\nu+1$ are defined as the sum on the second line of (114),

$$\bar{\mathbf{A}}_{s,n}^{\delta,\nu+1} = e(-\hat{\mathbf{u}}\cdot\bar{\mathbf{y}}_n^{\nu+1}) \sum_{q\in\mathfrak{S}_s^{\nu+1}}\sum_{p=1}^{P} S_s^{\nu+1}(\mathbf{y}_{q,p},\bar{\mathbf{y}}_n^{\nu+1}) e(\hat{\mathbf{u}}\cdot\mathbf{y}_{q,p})\mathbf{A}_{q,p}. \tag{115}$$

The directional sources on level ν are then obtained by anterpolation between levels $\nu+1$ and ν,

$$\bar{\mathbf{A}}_{s',\sigma}^{\delta',\nu} = e(-\hat{\mathbf{u}}'\cdot\bar{\mathbf{y}}_{\sigma}^{\nu}) \sum_{s\in\mathfrak{C}^{\nu}(s')} \sum_{n=1}^{L} S_{s'}^{\nu}(\bar{\mathbf{y}}_{n}^{s,\nu+1},\bar{\mathbf{y}}_{\sigma}^{\nu}) e(\hat{\mathbf{u}}'\cdot\bar{\mathbf{y}}_{n}^{s,\nu+1}) \bar{\mathbf{A}}_{s,n}^{\delta,\nu+1}, \quad \delta'\in\mathfrak{D}^{\nu+1}(\delta). \tag{116}$$

Note that the contributions from all child source clusters in $\mathfrak{S}_{s'}^{\nu}$ are accounted for by summing over $s\in\mathfrak{C}^{\nu}(s')$. Also note that the above formula applies to all directions δ' on level ν that are the closest to the child direction δ on level $\nu+1$. The relation between the directions on the two levels is denoted by the set $\delta'\in\mathfrak{D}^{\nu+1}(\delta)$. Given the direction δ on level $\nu+1$, the directions δ' on level ν satisfy

$$\delta'\in\mathfrak{D}^{\nu+1}(\delta): \quad |\hat{\mathbf{u}}_{\delta'}^{\nu} - \hat{\mathbf{u}}_{\delta}^{\nu+1}| < \min_{q\neq\delta} |\hat{\mathbf{u}}_{\delta'}^{\nu} - \hat{\mathbf{u}}_{q}^{\nu+1}|. \tag{117}$$

By inserting (116) and (115) into (114), the field value after the two-level anterpolation satisfies

$$\widetilde{\mathbf{H}}_{r}^{\delta',\nu}(\mathbf{x}_i) = \sum_{\sigma=1}^{L} G(\mathbf{x}_i,\bar{\mathbf{y}}_{\sigma}^{\nu}) \bar{\mathbf{A}}_{s',\sigma}^{\delta',\nu}. \tag{118}$$

The two-level interpolation formula is derived by first interpolating $G(\mathbf{x}_i,\mathbf{y})$ from $G(\bar{\mathbf{x}}_m^{\nu+1},\mathbf{y})$ (in the direction $\hat{\mathbf{u}}$), and then interpolating $G(\bar{\mathbf{x}}_m^{\nu+1},\mathbf{y})$ from $G(\bar{\mathbf{x}}_{\rho}^{\nu},\mathbf{y})$ (in the direction $\hat{\mathbf{u}}'$). Similar to the anterpolation case, this leads to

$$G(\mathbf{x}_i,\mathbf{y}) \approx e(-\hat{\mathbf{u}}\cdot\mathbf{x}_i) \sum_{m=1}^{L} S_{r}^{\nu+1}(\mathbf{x}_i,\bar{\mathbf{x}}_m^{\nu+1}) e(\hat{\mathbf{u}}\cdot\bar{\mathbf{x}}_m^{\nu+1}) \\ e(-\hat{\mathbf{u}}'\cdot\bar{\mathbf{x}}_m^{\nu+1}) \sum_{\rho=1}^{L} G(\bar{\mathbf{x}}_{\rho}^{\nu},\mathbf{y}) e(\hat{\mathbf{u}}'\cdot\bar{\mathbf{x}}_{\rho}^{\nu}) S_{r'}^{\nu}(\bar{\mathbf{x}}_m^{\nu+1},\bar{\mathbf{x}}_{\rho}^{\nu}).$$

We evaluate the above expression for $\mathbf{y}=\bar{\mathbf{y}}_{\sigma}^{\nu}$. Before substituting it into (118), we specialize the formula to locations $\mathbf{x}_i$ in receiver cluster r on level $\nu+1$. After reordering the terms,

$$\widetilde{\mathbf{H}}_{r}^{\delta,\nu+1}(\mathbf{x}_i) = e(-\hat{\mathbf{u}}\cdot\mathbf{x}_i) \sum_{m=1}^{L} S_{\ell}(\mathbf{x}_i,\bar{\mathbf{x}}_m) e(\hat{\mathbf{u}}\cdot\bar{\mathbf{x}}_m) \\ e(-\hat{\mathbf{u}}'\cdot\bar{\mathbf{x}}_m) \sum_{\rho=1}^{L} S'_{\ell}(\bar{\mathbf{x}}_m,\bar{\mathbf{x}}_{\rho}^{\nu}) e(\hat{\mathbf{u}}'\cdot\bar{\mathbf{x}}_{\rho}^{\nu}) \sum_{\sigma=1}^{L} G(\bar{\mathbf{x}}_{\rho}^{\nu},\bar{\mathbf{y}}_{\sigma}^{\nu}) \bar{\mathbf{A}}_{s',\sigma}^{\delta',\nu}$$

The above sums can be decomposed into three steps. First, transfer the directional field values to the Chebyshev points $\bar{\mathbf{x}}_{\rho}^{\nu}$ on level ν (also known as M2L, for multipole-to-local),

$$\widetilde{\mathbf{H}}_{r',\rho}^{\delta',\nu} = \sum_{\sigma=1}^{L} G(\bar{\mathbf{x}}_{\rho}^{\nu},\bar{\mathbf{y}}_{\sigma}^{\nu}) \bar{\mathbf{A}}_{s',\sigma}^{\delta',\nu}, \quad \rho\in[1,L]. \tag{119}$$

Thereafter, interpolate the field values to the Chebyshev points $\bar{\mathbf{x}}_m^{\nu+1}$ on level $\nu+1$. In the above example, there is only one source cluster s' that interacts with the receiver cluster r', in the single direction $\hat{\mathbf{u}}' = \hat{\mathbf{u}}_{\delta'}^{\nu}$. In general, there will be more than one source cluster and we must account for contributions from all directions $\hat{\mathbf{u}}_{\delta'}^{\nu}$ that are related to the the direction $\hat{\mathbf{u}}_{\delta}^{\nu+1}$ by (117). These considerations lead to the local-to-local (L2L) formula

$$\widetilde{\mathbf{H}}_r^{\delta,\nu+1}(\bar{\mathbf{x}}_m^{\nu+1}) = \sum_{\delta' \in \mathfrak{D}^{\nu+1}(\delta)} e(-\hat{\mathbf{u}}_{\delta'}^{\nu} \cdot \bar{\mathbf{x}}_m^{\nu+1}) \sum_{\rho=1}^{L} S'_\ell(\bar{\mathbf{x}}_m^{\nu+1}, \bar{\mathbf{x}}_\rho^{\nu}) e(\hat{\mathbf{u}}' \cdot \bar{\mathbf{x}}_\rho^{\nu}) \widetilde{\mathbf{H}}_{r',\rho}^{\delta',\nu}, \quad m \in [1, L]. \tag{120}$$

Finally, we are ready to interpolate to the individual receiver points. This operation is known as the L2E (local-to-element) formula,

$$\widetilde{\mathbf{H}}_r^{\delta,\nu+1}(\mathbf{x}_i) = e(-\hat{\mathbf{u}} \cdot \mathbf{x}_i) \sum_{m=1}^{L} S_r^{\nu+1}(\mathbf{x}_i, \bar{\mathbf{x}}_m^{\nu+1}) e(\hat{\mathbf{u}} \cdot \bar{\mathbf{x}}_m^{\nu+1}) \widetilde{\mathbf{H}}_r^{\delta,\nu+1}(\bar{\mathbf{x}}_m^{\nu+1}), \tag{121}$$

which is the same expression as in the single level case.

5.8.2 The general case

Given a tree structure with $B+1$ levels, note that the number of directions only depends on the level in the tree, and is the same for all source and receiver clusters on each level. The root level corresponds to $\nu = 0$ and the leaf level has $\nu = B$. Recall that there is only one direction on the leaf level.

The multi-level algorithm starts by anterpolating the point source strengths $\mathbf{A}_{q,p}$ to the Chebyshev node points in each source cluster on that level. This is done by setting $\nu + 1 = B$ and evaluating (115) with $\hat{\mathbf{u}} = \hat{\mathbf{u}}_1^B$ for all source clusters on the leaf level. Next, the directional source strengths on level $\nu = B - 1$ are anterpolated from the leaf level Chebyshev node points by applying (116) to each direction δ' on level $\nu = B - 1$. The directional anterpolation of the source strengths is repeated recursively until the root level of the source tree is reached. The directional field values at the root level of the tree are then evaluated by setting $\nu = 0$ and applying (119) to all directions δ' and receiver clusters r' on the root level of the receiver tree. The directional field values are then interpolated to level $\nu = 1$ by using formula (120). Note that contributions from several directions on level $\nu = 0$ are aggregated in this step. The directional interpolation is repeated recursively until the leaf level of the receiver tree is reached, thereby defining the directional field values at the Chebyshev node points in all receiver clusters, using the single direction on the leaf level. Finally, the field values at the receiver locations are evaluated from formula (121), applied to all receiver clusters on the leaf level.

To estimate the operational count of the multi-level algorithm we assume that the number of directions decrease by a factor of four when the level is increased from ν to $\nu+1$. At the same time, the number of clusters increases by a factor of four, see Figure 24. Thus the number of clusters times the number of directions is independent of the level, both for the source and receiver trees,

$$N_{sc}^B = N_{sc}^{\nu} N_{dir}^{\nu} = \text{const.}, \quad M_{rc}^B = M_{rc}^{\nu} N_{dir}^{\nu} = \text{const.}, \quad \nu = 0, 1, \ldots, B. \tag{122}$$

The operational count for the leaf level anterpolation (115) is $\mathcal{O}(N_{sc}^B \ell^3 P N_{qd})$. Anterpolating from level $\nu+1$ to level ν using (116) needs $\mathcal{O}(16 N_{sc}^{\nu} N_{dir}^{\nu} \ell^6$ operations. That step must be repeated B times. The top level transfer algorithm (119) requires $\mathcal{O}(N_{dir}^0 N_{sc}^0 M_{rc}^0 \ell^6)$ operations. The directional interpolation from level ν to level $\nu+1$ using (120) needs $\mathcal{O}(16 N_{dir}^{\nu} M_{rc}^{\nu} \ell^6)$ operations; it must be repeated B times to get to the leaf level. Finally, the leaf level interpolation formula (121) needs $\mathcal{O}(M_{rc}^B Q M_{qd} \ell^3)$ operations.

By using (122), the total operational count of the multi-level directional Chebyshev interpolation algorithm becomes

$$\mathcal{O}(N_{sc}^B (P N_{qd} \ell^3 + 16 B \ell^6) + \mathcal{O}(N_{dir}^0 N_{sc}^0 M_{rc}^0 \ell^6) + \mathcal{O}(M_{rc}^B (Q M_{qd} \ell^3 + 16 B \ell^6).$$

The total number of point sources equals $N_{tot} = N_{sc}^B P N_{qd}$ and the total number of receiver locations satisfies $M_{tot} = M_{rc}^B Q M_{qd}$. By using (122), we can write the total number of operations as

$$\mathcal{O}(N_{tot} \ell^3) + \mathcal{O}(M_{tot} \ell^3) + \mathcal{O}(N_{dir}^0 \ell^6 (16 N_{sc}^0 B + N_{sc}^0 M_{rc}^0 + 16 M_{rc}^0 B)).$$

The integer B follows from (110) and $N_{dir}^0 \approx 4^B$.

5.9 Parallel implementation

The multi-level algorithm was implemented on a parallel computer with distributed memory using the MPI library. The parallel implementation separately distributes the coarsest level receiver clusters and source clusters onto the processors. Let N_{proc} denote the total number of processors used. If there are M_{rc} receiver clusters and N_{sc} and source clusters on level $\nu = 0$, then each processor will hold approximately M_{rc}/N_{proc} receiver clusters, and N_{sc}/N_{proc} source clusters. It is assumed that M_{rc} and N_{sc} are larger than N_{proc}. If the number of processors is larger than M_{rc} or N_{sc} the algorithm becomes inefficient, because in the current implementation, there is no parallel decomposition of the directions. The child clusters are constructed by subdividing the clusters on the coarser level. This requires no communication, since it is done locally in each processor.

The interpolation and anterpolation operations can be performed locally inside each processor without any communication. These operations are expected to scale perfectly. The transfer operation on the top level of the tree ($\nu = 0$), described by (119), requires communication between the processors. Algorithm 1 describes how this is done. It is assumed that each process knows its unique identity, available in the variable `myid` in Algorithm 1. The function $\texttt{owner}_{rec}\texttt{(}r\texttt{)}$ returns identity of the process that owns receiver cluster r. The function $\texttt{owner}_{src}\texttt{(}s\texttt{)}$ is similar, but for the source clusters. The function `sum_reduce(v,p,s)` sums the variable **v** over all processors, and returns the sum, **s**, in process number p only. The complexity of Algorithm 1 is estimated as follows. There is one broadcast operation per receiver cluster, giving a cost on the order of $M_{rc}|L| \log N_{proc}$. A parallel update of the local part of the sum, giving on the order of $|L|^2 M_{rc} N_{sc}/N_{proc}$ operations. Sum-reduction of a vector of length $|L| N_{dir}$, giving on the order of $|L| M_{rc} N_{dir} \log N_{proc}$ operations. Considering the polynomial order fixed, this leads to a total cost which grows as $\mathcal{O}(N_{sc} M_{rc}/N_{proc} + M_{rc} N_{dir} \log N_{proc})$.

Algorithm 1 Parallel evaluation of the transfer algorithm.

% $\mathbf{c}_x^r$ is the center of receiver cluster r
% $\mathbf{c}_y^s$ is the center of source cluster s
% N_{dir} denotes the number of directions.
for $r := 1$ **to** M_{rc} **do**
  if myid = owner$_{rec}(r)$ **then**
    Broadcast $\bar{\mathbf{x}}_m^r$ and $\mathbf{c}_x^r$
  endif
  $\mathbf{F}_m^\delta := 0$, $m = 1, \ldots, L$, $\quad d = 1, \ldots, N_{dir}$
  for $s := 1$ **to** N_{sc} **do**
    if myid = owner$_{src}(s)$ **then**
      $\delta' := arg\,min_{d=1,\ldots,N_{dir}} |\hat{\mathbf{u}}_d - \hat{\mathbf{c}}|$, where $\hat{\mathbf{c}} = \mathbf{c}/|\mathbf{c}|$ and $\mathbf{c} = \mathbf{c}_x^r - \mathbf{c}_y^s$
      $\mathbf{F}_m^{\delta'} := \mathbf{F}_m^{\delta'} + \sum_{\sigma=1}^{L} G(\bar{\mathbf{x}}_m^r, \bar{\mathbf{y}}_\sigma^s) \bar{\mathbf{A}}_\sigma^{\delta',s}, \quad m = 1, \ldots, L$
    endif
  endfor
  sum_reduce($\mathbf{F}_m^\delta$, owner$_{rec}(r)$, $\tilde{\mathbf{H}}_r^\delta(\bar{\mathbf{x}}_m)$)
endfor

6 Numerical experiments

6.1 Tuning the aperture and separation thresholds

To evaluate the accuracy of the directional Chebyshev interpolation technique in 3-D, we consider a very small test case where the explicit summation formulas for the electric field (48) can be used to evaluate reference solutions. Let the incident field be an x-polarized Gaussian beam with wave length $\lambda_0 = 1.053 \cdot 10^{-6}$ m, waist $w_0 = 1.132 \cdot 10^{-5}$ m, and offset $z_0 = 0$ from the center of the grating plane. Let the angle of incidence on the grating plane be 0.5 rad and let the grating have period $d_g = 1.1765 \cdot 10^{-6}$ m, height (valley to peak) $h_g = 3.5 \cdot 10^{-7}$ m, and side lengths $L_x = L_y = 1.0109 \cdot 10^{-4} m \approx 96\lambda_0$. The grating is discretized by 1920 by 1920 quads, corresponding to 20 quads per wave length in both directions. The surface current on the first grating is computed with the physical optics approximation from the incident Gaussian beam.

The observation plane is placed at distance of $6.405 \cdot 10^{-5}$ m from the center of the grating plane, in the direction of the exit angle for the $m = 1$ reflection, $\beta = 0.428605$ rad, perpendicular to the reflected beam. The observation plane is a square with side length $L_{obs} = 7 \cdot 10^{-5}$ m. The electric field integral for computing the $\mathbf{E}$ field on the observation plane was discretized by 4 collocation points per quad. Because the observation plane is perpendicular to the reflected beam, the scattered field can be resolved on a mesh with 100 by 100 quads. To minimize the computational cost for the explicit summation method, we only evaluate the electric field at the center of each quad.

The relative accuracy of the directional Chebyshev interpolation technique is evaluated in the discrete L_2 and max-norms, see Figure 25 (left). Because the computational cost increases rapidly with the order of interpolation, we here focus on the case $\ell = 5$. As a baseline, we took $\mathcal{A}_a = \mathcal{A}_s = 1.0$. In this case, the relative error is $1.25 \cdot 10^{-5}$ in max norm

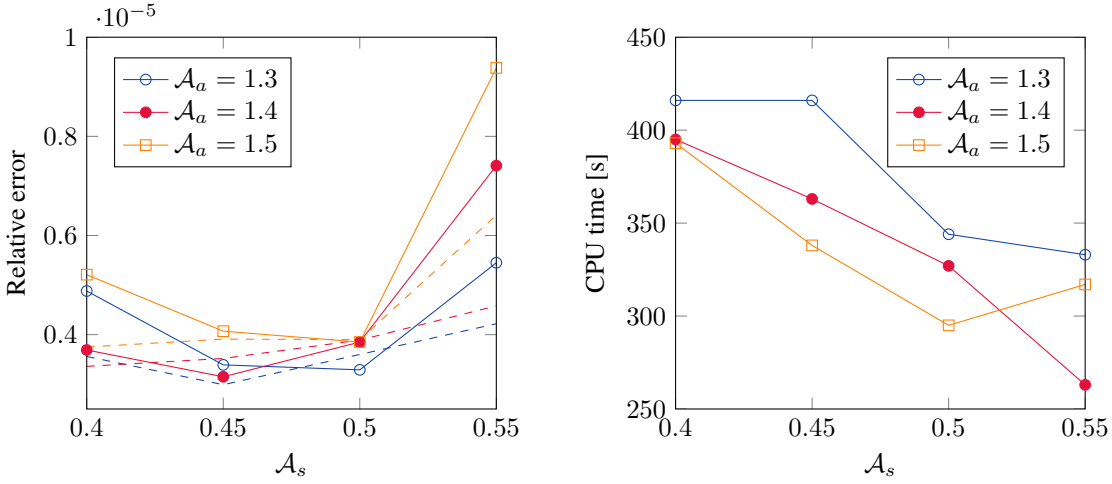

Figure 25: Left: Relative interpolation error in $\mathbf{E}$ on an observation screen, for different values of $\mathcal{A}_a$ and $\mathcal{A}_s$. The errors are shown in max-norm (solid) and in L_2-norm (dashed). Right: CPU times for evaluating $\mathbf{E}$ on the observation screen.

and $1.21 \cdot 10^{-5}$ in L_2-norm. After some experimentation, we found that the max-norm of the interpolation error has a local minima near $0.45 \leq \mathcal{A}_s \leq 0.5$, for all the values $\mathcal{A}_a = 1.3, 1.4, 1.5$. There is a similar, but less pronounced, trend for the L_2 error. Of the tested values, the smallest error in max-norm was $3.15 \cdot 10^{-6}$ and occurred for $\mathcal{A}_a = 1.4$ and $\mathcal{A}_s = 0.45$. The smallest error in L_2-norm was $2.99 \cdot 10^{-6}$. It occurred for $\mathcal{A}_a = 1.3$, but for the same $\mathcal{A}_s = 0.45$. For these values of $\mathcal{A}_a$ and $\mathcal{A}_s$, the errors are about four times smaller compared to the baseline case.

The analyses and numerical experiments in Sections 5.3-5.4 indicate that smaller values of $\mathcal{A}_a$ and $\mathcal{A}_s$ should always make the Chebyshev interpolation more accurate. However, the above 3-D experiments show a more complicated dependence on these parameters. We attribute this behavior to additional errors incurred by the multi-level anterpolation and interpolation algorithms, which is not included in the above analysis.

We also note that the smallest interpolation errors occur when the coefficient $\mathcal{A}_a$ is about three times larger than $\mathcal{A}_s$. This effect is probably specific to this application, because the offset vector $\mathbf{r}$ is always close to perpendicular to the separation vector $\mathbf{c}$. Thus, the variation of the phase in the directional kernel is mostly due to the separation between source and receiver clusters (controlled by $\mathcal{A}_s$), and to a lesser extent due to the misalignment between $\hat{\mathbf{u}}$ and $\hat{\mathbf{c}}$, which is bounded by the value of $\mathcal{A}_a$.

Next, we report on how the threshold values $\mathcal{A}_a$ and $\mathcal{A}_s$ influence the CPU time for our parallel implementation of the directional Chebyshev interpolation algorithm. Because the case is small, we perform the comparison using only 72 MPI-tasks, running on 2 nodes (72 cores) of the Quartz machine at Livermore Computing. As a reference point, the baseline case with $\mathcal{A}_a = 1$ and $\mathcal{A}_s = 1$ took 379 s of CPU time. The run-times for the aforementioned values of $\mathcal{A}_a$ and $\mathcal{A}_s$ are reported in Figure 25 (right), where we note that the timings on this system are not very precise and can vary by 10 to 15 percent.

Nevertheless, compared to the baseline case, a significantly more accurate solution can be calculated using less or equal amounts of CPU-time.

The computational cost of the directional Chebyshev interpolation can be dissected by studying how the number of clusters and directions depend on $\mathcal{A}_a$ and $\mathcal{A}_s$.

6.2 Parallel scaling

We consider a sequence of test problems that honor both the transverse and longitudinal length scales involved in beam propagation. We take the transverse length scale to be the beam radius, w_0. The longitudinal length scale is governed by the diffraction length, $z_R = 0.5kw_0^2$, which also is known as the Rayleigh length. The beam is the thinnest at its waist $z = z_0$ and only stays coherent for propagation distances $z - z_0 \leq \mathcal{O}(z_R)$. At larger distances, the beam becomes diffuse and is not useful for the grating compressor application.

Let the distance between the first and second grating, along the center path of the reflected beam, be L_{12}. For a table-top compressor operating in the infrared spectrum with center wave length $\lambda = 1.053 \cdot 10^{-6}m$, the beam would have a radius $\approx 1 \cdot 10^{-3}m$ and $L_{12} \approx 0.5m$. These dimensions can be characterized by the non-dimensional Fresnel number,

$$F := \frac{w_0^2}{\lambda L_{12}} = \frac{z_R}{\pi L_{12}} \approx 1.9, \quad z_R = \frac{kw_0^2}{2}.$$

The total path-length through the compressor is about $5L_{12} = 5z_R/(\pi F) \approx 0.84z_R$, which indicates that the EM-field exiting the compressor should have beam-like properties.

The gratings must be sufficiently wide to avoid scattering from the edges. Let the first grating have side lengths $L_x^1 \times L_y^1$, where L_y^1 is the non-dispersive direction. If the angle of incidence is α, $L_x^1 \approx L_y^1/\cos(\alpha)$. For a Gaussian beam we use $L_y^1 \approx 10w_0$. The second grating can have the same dimension in the non-dispersive direction, $L_y^2 = L_y^1$, but must be wider in the dispersive direction to capture the variation in direction of the reflected beam, due to angular dispersion. Here we use $L_x^2 = 1.5L_x^1$.

In the following numerical tests, we use a scaling factor $\gamma > 0$ and choose the dimensions of the beam and two gratings according to

$$\lambda = 1.053 \cdot 10^{-6}, \quad \alpha = 0.5, \quad \beta = 0.4286047, \quad w_0 = \gamma\, 3.16 \cdot 10^{-4}, \quad L_{12} = \gamma^2 0.05,$$
$$L_x^1 = \gamma\, 3.5 \cdot 10^{-3}, \quad L_y^1 = \gamma\, 3.13 \cdot 10^{-3}, \quad L_x^2 = \gamma\, 5.26 \cdot 10^{-3}, \quad L_y^2 = \gamma\, 3.13 \cdot 10^{-3}.$$

We consider the values $\gamma = 0.03, 0.06, 0.12, 0.24, 0.36$, which all fit in memory on 8 nodes (288 cores) of the Quartz machine at Livermore Computing. Because the longitudinal separation between the gratings is proportional to γ^2, the separation condition (94) implies that the cluster size on the top level, $d_0 = \sqrt{\mathcal{A}_s|\mathbf{C}|/k} \sim \gamma$. Because the grating sizes are proportional to γ, the number of clusters will be independent of γ. Here we have chosen the dimensions such that the first grating is decomposed into $N_{sc} = 80 \times 72$ clusters and the second grating has $M_{rc} = 120 \times 72$ clusters. This number of clusters allows the MPI-tasks to be evenly distributed on 36, 72, 144, and 288 cores, using one MPI-task per core.

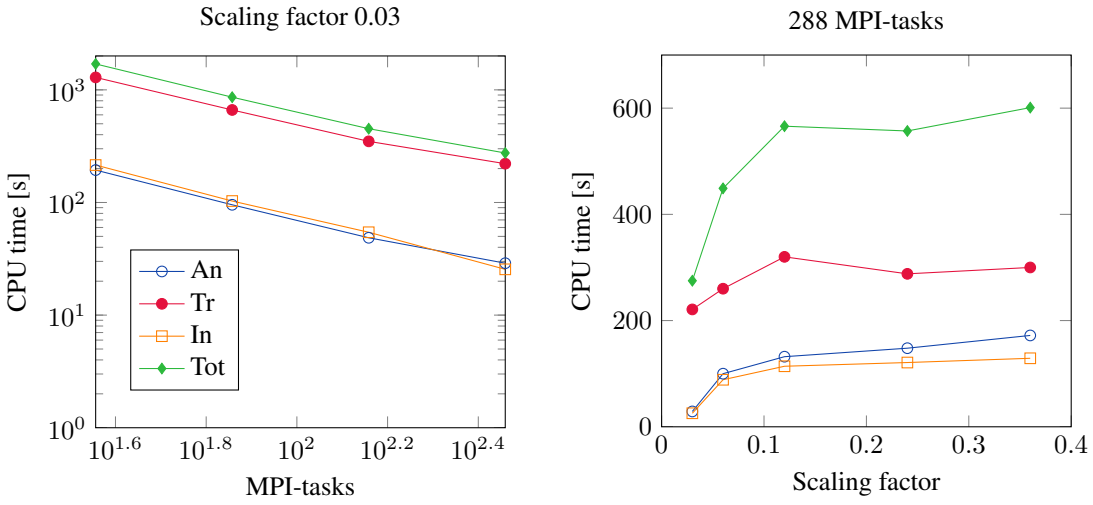

Figure 26: CPU time for the anterpolation (An), Transfer (Tr), Interpolation (In), and Total (Tot). Left: Varying the number of MPI-tasks (36, 72, 144, 288) for a fixed problem size (strong scaling). Right: Increasing the problem size for 288 MPI-tasks.

For the smallest problem size, with $\gamma = 0.03$, we report a strong scaling study in Figure 26 (left side). The total CPU time is dominated by the execution of the transfer algorithm. The anterpolation and interpolation algorithms require about 6 times less CPU-time than the transfer. Both the anterpolation and interpolation, which do not involve any MPI-communication, show almost perfect scaling. For the transfer operation there is a significant speed-up from 144 to 288 tasks, but it is not perfect. This behavior agrees with the performance estimate in Section 5.9.

On the right side of Figure 26 we report how the CPU-time depends on the problem size, when 288 MPI-tasks are used (1 MPI-task per core). Here we consider five values of the scaling factor $\gamma = 0.03, 0.06, 0.12, 0.24$, and 0.36. For the three larger values of γ, the CPU time for the transfer operation levels out, while the computational time for both the anterpolation and interpolation operations grow approximately linearly with γ. These trends can be understood by studying how the problem parameters vary with γ, see Table 3. For the smallest case, the minimal separation is $|\mathbf{C}| \approx 4.14 \cdot 10^{-5} m$ ($k \approx 5.97 \cdot 10^{6} m^{-1}$). However, the side lengths of the gratings are more than twice as large, which means that the ranges in aperture angles are large (2.30 and 2.52 rad). Despite the small size of the gratings, a significant number of directions are needed, which explains why the transfer operation dominates the total CPU-time for $\gamma = 0.03$ and, to a lesser extent, for $\gamma = 0.06$.

In general, the computational cost of the transfer operation depends on the product of the number of source clusters, the number of receiver clusters, and the number of directions, i.e., $N_{sc} M_{rc} N_{dir}$. Because N_{sc} and M_{rc} are constant, the transfer cost is proportional to N_{dir}. For the three larger values of γ, the CPU-time for the transfer operation levels out because the number of directions only grows marginally between $\gamma = 0.12$ and $\gamma = 0.36$. As γ gets larger, the range in aperture angle in the polar and azimuth

γ	$k\|\mathbf{C}\|$	$d/\|\mathbf{C}\|$	N_{tot}	M_{tot}	θ_{rg} [rad]	ϕ_{rg} [rad]	$4\Delta\theta$ [rad]	Dirs	Lev
0.03	2.47e2	4.49e2	8.59e7	1.08e7	2.30	2.52	1.91e-1	13×14	5
0.06	9.86e2	2.25e-2	3.44e8	4.30e7	1.69	1.96	9.55e-2	18×21	6
0.12	4.07e3	1.11e-2	1.40e9	1.75e8	1.00	1.23	4.70e-2	22×27	6
0.24	1.56e4	5.65e-3	5.40e9	6.81e8	0.55	0.64	2.39e-2	23×27	6
0.36	3.58e4	3.73e-3	1.23e10	1.54e9	0.37	0.44	1.58e-2	24×28	6

Table 3: Problem sizes as function of the scaling factor γ. All cases have the same number of source clusters ($N_{sc} = 80 \times 72$) and the same number of receiver clusters ($M_{rc} = 120 \times 72$). Here, N_{tot} is the number of point sources, M_{tot} is the number of receiver locations, $\theta_{rg} = \theta_{max} - \theta_{min}$ is the range in polar angle, $\phi_{rg} = \phi_{max} - \phi_{min}$ is the range in azimuth angle, and $\Delta\theta$ satisfies (98).

directions (θ_{rg} and ϕ_{rg}) are approximately proportional to $L_x/L_{12} \sim 1/\gamma$. Moreover, the aperture condition (95) gives $\Delta\theta \sim 1/(kd) \sim 1/\gamma$. Because both quantities decrease at the same rate when γ increases, the number of directions tends to a constant, which also means that the number of levels in the tree becomes constant. As the problem is scaled up, we can therefore expect the transfer cost to tend to a constant, which approximately agrees with the observed timings for the three largest γ in Figure 26. For a fixed number of source and receiver clusters, and a fixed number of levels in the tree, the computational cost for the leaf level anterpolation step (E2M) depends linearly on the number of point sources. In a similar way, the cost of the leaf level interpolation (L2E) in the receiver tree depends linearly on the number of receiver locations. The remaining costs of both the anterpolation (M2M) and interpolation (L2L) are constant when the number of clusters and the number of levels are fixed. This analysis agrees with the observed timings for the anterpolation and interpolation in Figure 26.

7 A symmetric compressor simulation

We consider simulating the symmetric compressor [25] outlined in Figure 27. The center wavelength is $\lambda_c = 1.053 \cdot 10^{-6}$ m and the period of the gratings is $d_g = 1.1765 \cdot 10^{-6}$ m. The angle of incidence on the first grating is $\alpha = 0.5$ rad. The grating equation (1) gives the angle of reflection $\beta_1 = 0.42860$ rad, corresponding to order $m = 1$ at the center wavelength. For the second grating, the incident and exiting angles are reversed because the first and second gratings are parallel. The third and fourth gratings are placed at a mirror image of the first and second gratings, with corresponding angles. The inter-grating distances indicated in Figure 27 refer to the path length of the center wavelength. The first and second gratings are parallel, but their centers are offset. In the same way, gratings three and four are parallel and their centers are also offset.

For a Gaussian incident field with radius $w_0 = 3.16 \cdot 10^{-4}$ m, the Rayleigh length is

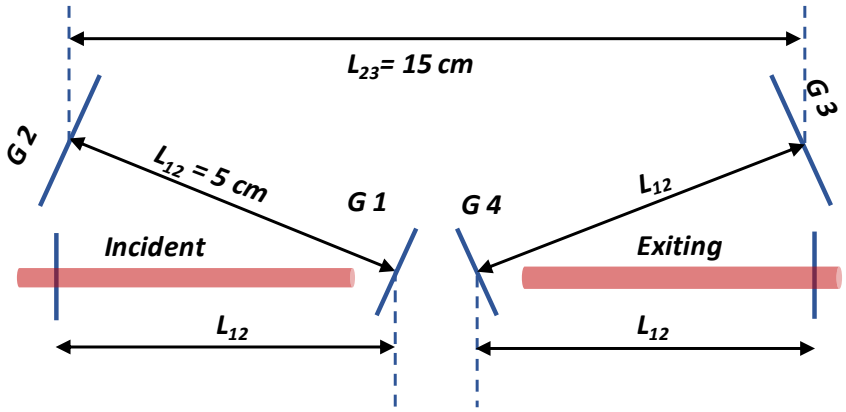

Figure 27: The geometry of a symmetric compressor.

$z_R = 0.5 k_c w_0^2 \approx 0.29416$ m. The path length through the compressor is about 0.25 m. By locating the beam waist to be in the middle of gratings two and three, the path length from the first grating to the waist is approximately $0.425\, z_R$. This is done so that both the incident and output fields maintain beam-like properties.

We consider the case when the time function along the centerline of the incident pulse is the chirped Gaussian described by (14), i.e.,

$$g(t) = p(t) e^{i\omega_c t}, \quad p(t) = \exp\left(\frac{-(1+ia)t^2}{\tau^2}\right).$$

The Fourier transform of the enveloped function $p(t)$ is given by (17). It can be written on the form

$$\widehat{p}(\Omega) = \sqrt{\pi \tau_0^2 (1-ia)}\, \exp\left(\frac{-\Omega^2 \tau_0^2 (1-ia)}{4}\right), \quad \Omega = \omega - \omega_c, \quad \tau_0 = \frac{\tau}{\sqrt{1+a^2}}. \tag{123}$$

Let the time function along the centerline of the output pulse and its Fourier transform be

$$e(t) = q(t) e^{i\omega_c t}, \quad \widehat{e}(\omega) = \widehat{q}(\omega - \omega_c), \tag{124}$$

where $\widehat{q}(\Omega)$ is the Fourier transform of the output envelope function.

For an idealized symmetric compressor (perfect gratings with constant line period and height, perfect alignment, etc.) the Fourier transform of the output envelope function can be expressed in terms of the incident envelope function and a transfer function (see Diels and Rudolph [8]),

$$\widehat{q}(\Omega) = \widehat{p}(\Omega) \exp(i k_c \gamma_c^2 L_{12} \Omega^2), \tag{125}$$

Here, L_{12} is the distance between the first and second gratings along the path of the center frequency, and $\gamma_c = \gamma(\omega_c)$ is the angular dispersion rate for the gratings, evaluated at the center frequency.

The angular dispersion rate is found by substituting $\lambda = 2\pi c/\omega$ into the grating equation (1) and differentiating it with respect to ω,

$$\gamma(\omega) := \frac{d\beta_m}{d\omega} = \frac{-2\pi\, c\, m}{\omega^2 d_g \cos(\beta_m)}. \tag{126}$$

For $m = 1$ and the above values of d_g and β_1, it becomes $\gamma_c = \gamma(\omega_c) = -5.5010 \cdot 10^{-16}$ s. By inserting the expression for $\widehat{p}$ from (123) into (126), we arrive at

$$\widehat{q}(\Omega) = \sqrt{\pi\tau_0^2(1-ia)}\exp\left(\frac{-\Omega^2\tau_0^2(1-ia)}{4}\right)\exp(ik_c\gamma_c^2 L_{12}\Omega^2). \tag{127}$$

Thus, the quadratic variation in the phase cancels if

$$\frac{\tau_0^2 a}{4} + k_c\gamma_c^2 L_{12} = 0, \quad a = -\frac{4k_c\gamma_c^2 L_{12}}{\tau_0^2}. \tag{128}$$

Inserting (128) into (127) and inverse Fourier transforming,

$$\widehat{q}(\Omega) = \sqrt{1-ia}\sqrt{\pi\tau_0^2}\exp\left(\frac{-\Omega^2\tau_0^2}{4}\right), \quad q(t) = \sqrt{1-ia}\exp\left(-\frac{t^2}{\tau_0^2}\right).$$

From (124), the idealized output time function becomes

$$e(t) = \sqrt{1-ia}\exp\left(\frac{-t^2}{\tau_0^2}\right)\exp(i\omega_c t).$$

Here we take $\tau_0 = 2 \cdot 10^{-13}$ s, which gives $a = -9.0282$. As a result, the time scale of the incident pulse becomes

$$\tau = \tau_0\sqrt{1+a^2} \approx 1.8167 \cdot 10^{-12} \text{ s}.$$

The time scale of the incident time function is τ, while it is τ_0 in the output pulse. The compression ratio of an ideal symmetric compressor is therefore determined by

$$\frac{\tau}{\tau_0} = \sqrt{1+a^2} \approx 9.0834.$$

where the coefficient a is defined by (128).

The idealized output time function and the phase of the output envelope function are shown in Figure 28. Compared to the incident time function and the phase of the incident envelope function (see Figure 4), the output time function has significantly shorter duration, and the output envelope function has constant phase.

7.1 The incident beam

We will consider two types of incident beams. First a Gaussian for which the magnetic field on the grating surface follows from an analytical formula. Secondly, we consider a

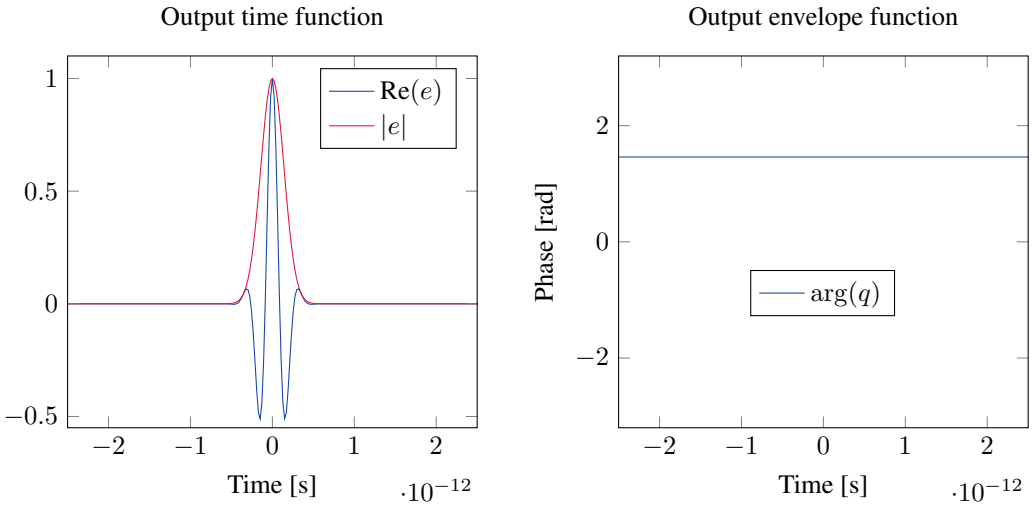

Figure 28: Left: real part and magnitude of the output time function, $e(t)$, with $\omega_c = 1.7888 \cdot 10^{13}$ rad/s. The actual value of ω_c is 100 times larger. Right: phase of the output envelope function, $\tan^{-1}(\mathrm{Im}\,(q)/\mathrm{Re}\,(q))$.

super-Gaussian beam, where the spatial envelope function is only known on the input transverse plane. The super-Gaussian beam is a simple example of a realistic case where the electro-magnetic fields of the beam cannot be described by a closed form analytical expression. Instead the incident beams are often modeled by a beam propagation code such as VBL [21]. In such models, it is only convenient to evaluate the fields along transverse planes, and not along the fine scale features of a grating surface, which also is inclined relative to the propagation direction of the incident beam.

Let (x, y, z) be the Cartesian coordinates with respect to a fixed "lab" frame such that the compressor resides in the half-space $z > 0$. Let the incident laser pulse travel in the positive z-direction. If a metallic plate of infinite extent was placed in front of the compressor, at $z = 0$, it would scatter the incident $\mathbf{E}$ and $\mathbf{H}$ fields completely, such that $\mathbf{E} = 0$ and $\mathbf{H} = 0$ behind the plate ($z > 0$), see Figure 29. We can decompose the total electric and magnetic fields into incident and scattered parts,

$$\mathbf{E} = \mathbf{E}_{in} + \mathbf{E}_{sc}, \quad \mathbf{H} = \mathbf{H}_{in} + \mathbf{H}_{sc}.$$

Because $\mathbf{E} = 0$ and $\mathbf{H} = 0$ behind the plate,

$$\mathbf{E}_{sc} = -\mathbf{E}_{in}, \quad \mathbf{H}_{sc} = -\mathbf{H}_{in}, \quad z > 0. \tag{129}$$

As a special case of the surface equivalence theorem, the physical equivalence theorem [3] allows the scattered field can be represented by a surface current $\mathbf{J}_s$ along the metallic plate. An expressions can be derived for the surface current,

$$\mathbf{J}_s = 2\,\widehat{\mathbf{n}} \times \mathbf{H}_{in}, \quad z = 0, \tag{130}$$

which in general is known as the physical optics approximation. However, in this case the formula (130) is exact because the metallic plate is planar and of infinite extent [3].

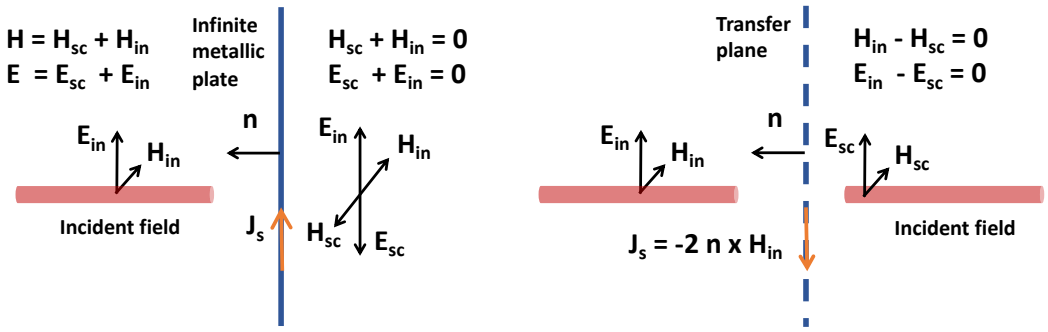

Figure 29: Left: a surface current $\mathbf{J}_s$ along the metallic plate at $z = 0$ is induced by the incident beam. Right: behind the metallic plate ($z > 0$), the incident field equals the field scattered by the surface current $-\mathbf{J}_s$.

The integral representations (6) and (8) are linear in $\mathbf{J}_s$. Thus, by reversing the sign of $\mathbf{J}_s$ in (130), the surface current $-\mathbf{J}_s$ will generate a scattered field that equals the incident field ($\mathbf{E}_{in}$, $\mathbf{H}_{in}$), for any location behind the metallic plate, see Figure 29. After discretization, the integral formulas (6) and (8) allow the incident field to be evaluated at any location with $z > 0$, in particular on the grating surface. Note that the surface current only depends on the incident magnetic field along the transverse plane $z = 0$. This quantity is readily available, either from a beam propagation code, or from an analytical formula.

7.2 Propagating the beam through the compressor

For simplicity, we only consider sinusoidal grating profiles, but this is not a restriction of our approach. In a local coordinate system, where the grating plane is aligned with the Cartesian (x', y') coordinates and the y' direction is aligned with the global y-coordinate, the profiles on all four gratings satisfy

$$z_0'(x') = \frac{h_g}{2} \sin\left(\frac{2\pi\, x'}{d_g}\right), \quad h_g = 3.50 \cdot 10^{-7}, \quad \text{Perfect profile.}$$

Note that h_g is the peak-to-valley height of the grating.

The first and fourth gratings have dimensions 3.43 mm by 3 mm. Because of the angular dispersion, gratings two and three are larger, with dimensions 5 mm by 2.82 mm. The gratings are discretized by 20 quads per center wavelength across the grating lines. Because the variation in surface current is significantly slower along the grating lines, we use 1 quad per wavelength along the grating lines. This results in about $1.63 \cdot 10^8$ quads for gratings one and four. For gratings two and three, we get about $3.19 \cdot 10^8$ quads per grating.

The envelope of the incident chirped Gaussian time function was truncated to $-3\tau \leq t \leq 3\tau$ to approximate a periodic function with period $T_{inc} = 1.088 \cdot 10^{-11}$ s. A discrete

Fourier transform with $N_f = 84$ frequencies corresponding to

$$\Omega_j = j\Delta\Omega, \quad j \in [-42, 41], \quad \Delta\Omega = \frac{1}{T_{inc}},$$

gives the discrete Fourier amplitudes of the incident envelope function

$$\widehat{p}_j, \quad j \in [-42, 41].$$

The corresponding discrete wave numbers are $k_j = (\Omega_j + \omega_c)/c$.

For each discrete wave number, the incident field is first transformed to a surface current on the first grating using the PO approximation. The scattered magnetic field is then evaluated along the second grating, where it is transformed to a surface current using PO. This procedure is repeated until a surface current is obtained on the fourth grating. The scattered electric field is then evaluated along a transverse observation plane at distance L_{12} from the fourth grating, see Figure 27. The observation plane has the dimensions 4 mm by 4 mm. Because it is transverse to the outgoing beam, it can be resolved on a relatively coarse mesh with 1000×1000 quads. The electric field for each discrete wave number is evaluated at the center of each quad on the observation plane. Once the electric field has been evaluated for all discrete wave numbers, we have a numerical representation of the spectral response function for the compressor,

$$\widehat{\mathbf{R}}_{m,n}(\Omega_j), \quad (m, n) \in [1, 1000]^2, \quad j \in [-42, 41].$$

This response function corresponds to the factor $\exp(ik_c\gamma_c^2 L_{12}\Omega^2)$ in the idealized formula (125). A fundamental difference from the idealized case is that the simulations capture the spatial variations of the spectral response function.

The discrete Fourier transform of the output envelope function for the electric field follows from

$$\mathbf{E}_{m,n}(\Omega_j) = \widehat{p}(\Omega_j)\widehat{\mathbf{R}}_{m,n}(\Omega_j), \quad (m, n) \in [1, 1000]^2, \quad j \in [-42, 41],$$

where $\widehat{p}(\Omega_j)$ is the Fourier coefficient of the incident envelope function. The electric field in the time domain is finally obtained by applying an inverse discrete Fourier transform to $\mathbf{E}_{m,n}(\Omega_j)$, at the center of each quad (m, n) on the observation plane. Because the incident electric field is polarized in the x-direction, the electric field on the observation plane is dominated by the $E^{(x)}$ component. In the following, we disregard the carrier wave in the time-dependent electric field and denote the time-dependent envelope function by

$$\mathcal{E}^{(x)}(x, y, t).$$

7.3 Computational results

The simulations were performed on 384 nodes (13824 cores) of the Quartz cluster at Livermore Computing using the parallel, distributed memory code **js2js**, which implements the directional Chebyshev interpolation technique described above. The simulations for

each wave number were distributed over 64 nodes (2304 cores), which means that 6 wave numbers could be grouped together and calculated simultaneously. Thus, all 84 wave numbers were processed in 14 groups, each including 6 wave numbers. Simulating 84 wave numbers in this fashion required about 5.5 hours of CPU time.

The cluster decomposition is constructed with the aperture and separation thresholds $\mathcal{A}_a = 1$ and $\mathcal{A}_s = 1$. The simulations used Chebyshev polynomials of order $\ell = 5$, for a total of $\ell^3 = 125$ node points per cluster. The following specifications depends slightly on the wave number: The surface current on the first grating is represented by $N_{tot} \approx 1.117 \cdot 10^9$ point sources and the magnetic field on the second grating is evaluated at $M_{tot} \approx 3.054 \cdot 10^8$ receiver locations. On the root level, the sources on the first grating are grouped into 55 by 49 clusters and the receivers on the second grating are grouped into 193 by 46 clusters. The tree had 7 levels with 4692 directions on the root level and one direction on the leaf level.

7.3.1 Gaussian incident beam

The magnetic field corresponding to a Gaussian incident beam can be directly evaluated on the grating surface from the analytical expression (28)-(30). Here, we consider the case where the electric field is polarized in the x-direction with amplitudes $A_x = 1 \cdot 10^3$ V/m and $A_y = 0$; the beam radius is $w_0 = 3.14 \cdot 10^{-4}$ m at the waist, and the offset from the waist is $z_0 = -0.125$ m.

The electric field envelope, $\mathcal{E}^{(x)}$, along the center line $y = 0$ of the observation plane is plotted in Figure 30. Note that the magnitude of $\mathcal{E}^{(x)}$ is well-focused both in space and time. The phase of $\mathcal{E}^{(x)}$ is constant in time and only decays slightly with $|x|$.

We consider two perturbations of the first grating only, i.e., gratings two, three, and four are not perturbed in this experiment. The first perturbation models line expansion due to heat disposition [1] by linearly expanding the grating period in the local y'-direction,

$$z_1'(x', y') = \frac{h_g}{2} \sin\left(\frac{2\pi\, x'}{d_g(1 + \varepsilon_1 y')}\right), \quad \varepsilon_1 = \frac{0.01}{1.5 \cdot 10^{-3}}, \quad \text{Perturbation \#1.}$$

This perturbation results in a ± 1 percent variation of the period over the grating surface. Secondly, we model inaccuracies in the manufacturing process by adding a long wavelength perturbation of the grating line height,

$$z_2'(x') = \frac{h_g}{2}\left(1 + \frac{\sin(2\pi x'/d_p)}{20}\right) \sin\left(\frac{2\pi\, x'}{d_g}\right), \quad d_p = 3.43 \cdot 10^{-4}, \quad \text{Perturbation \#2.}$$

This perturbation introduces a ± 5 percent variation of the line height.

For grating perturbation # 1, Figure 31 shows the electric field envelope, $\mathcal{E}^{(x)}$, on the observation plane. Compared to the perfect case, the amplitude is significantly lower and the beam is spread out in the x-direction. The phase is still constant in time, but decreases more significantly with $|x|$ (each black band indicates a 2π discontinuity in the phase due a branch cut in the $\tan^{-1}$ function).

For grating perturbation #2, Figure 32 shows $\mathcal{E}^{(x)}$ on the observation plane. Note the two waists in the outer contour of the magnitude at $x \approx \pm 0.75$ mm. This indicates that

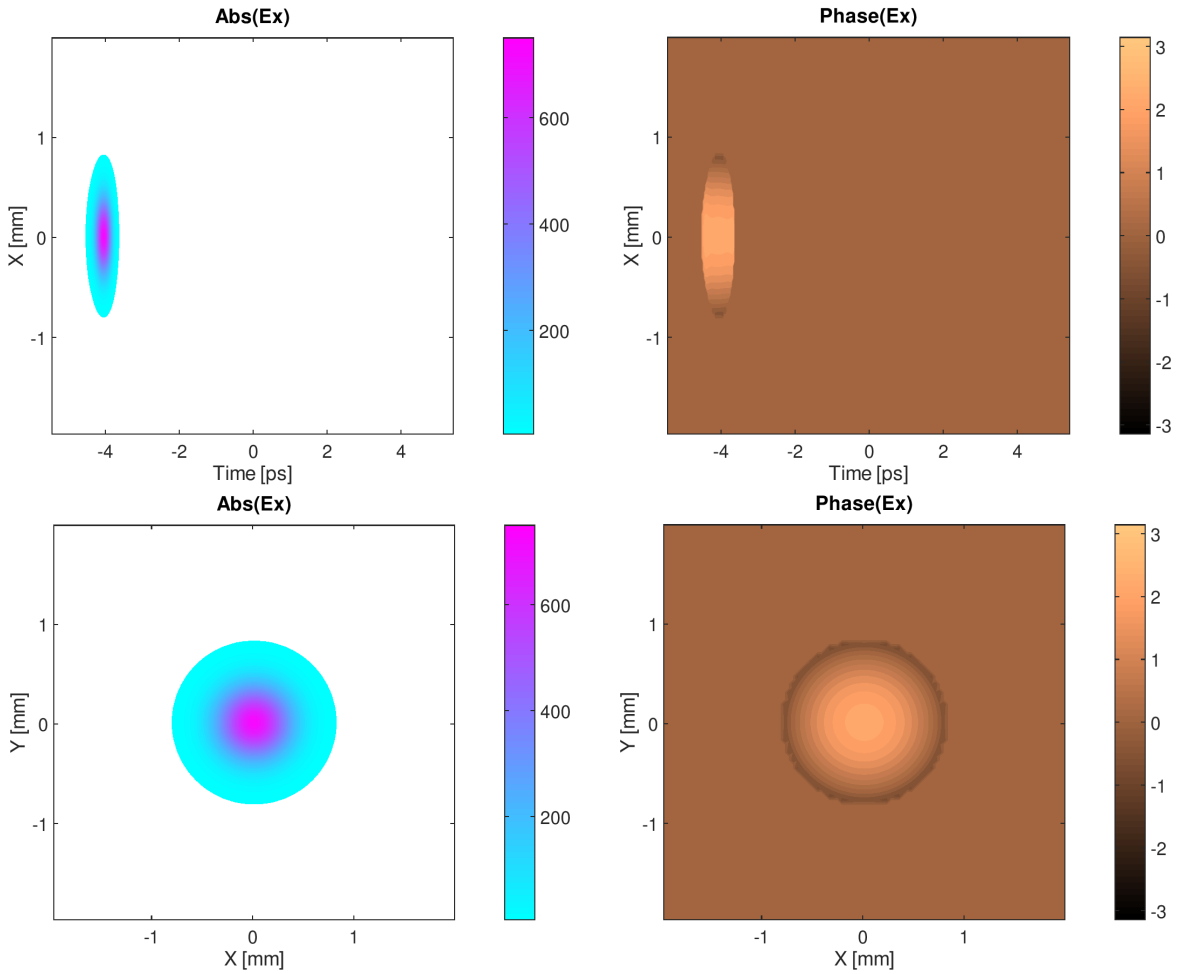

Figure 30: The $\mathcal{E}^{(x)}$ envelope on the observation screen for perfect gratings and a Gaussian incident beam. Left column: magnitude; right column: phase. Top row: $\mathcal{E}^{(x)}$ in the (t, x)-plane along the center line, $y = 0$. Bottom row: $\mathcal{E}^{(x)}$ in the (x, y)-plane for $t = -4.049 \cdot 10^{-12}$ s. Only $|\mathcal{E}^{(x)}| \geq 5$ is plotted.

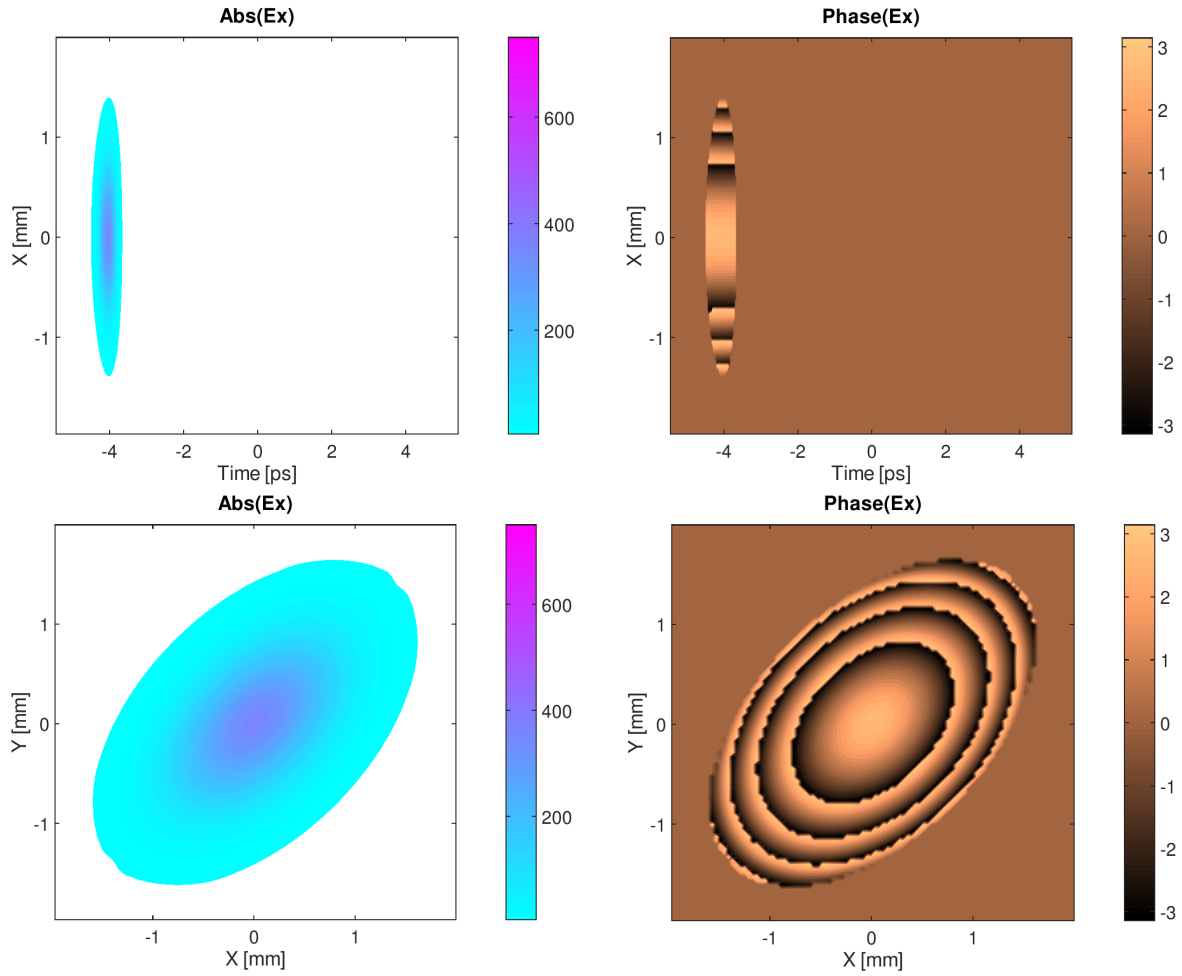

Figure 31: The $\mathcal{E}^{(x)}$ envelope on the observation screen for perturbation # 1 and a Gaussian incident beam. Left column: magnitude; right column: phase. Top row: $\mathcal{E}^{(x)}$ in the (t, x)-plane along the center line, $y = 0$. Bottom row: $\mathcal{E}^{(x)}$ in the (x, y)-plane for $t = -4.049 \cdot 10^{-12}$ s. Only $|\mathcal{E}^{(x)}| \geq 5$ is plotted.

the beam has been split into three beams; one main beam and two "ghost" beams [16], to the left and right of the main beam. Compared to the perfect case, the intensity of the field is now split between the three beams, with most intensity in main beam. The phase remains constant in time. Within the main beam the phase is approximately constant in $|x|$, but varies significantly with x in the two "ghost" beams.

7.3.2 Super-Gaussian incident beam

In a super-Gaussian beam, the spatial envelope function is only known on a transverse plane ($z = \text{const.}$),

$$\psi_{sg}(\xi,\eta,k) = \exp\left(-(\xi^4+\eta^4) - \frac{ikw_{sg}^2(\xi^2+\eta^2)}{2z_{sg}}\right), \quad \xi = \frac{x}{w_{sg}}, \quad \eta = \frac{y}{w_{sg}}. \tag{131}$$

Similar to the Gaussian beam, z_{sg} is the distance between the waist and the transverse plane. Because of the fourth power of ξ and η in the exponent, the magnitude decays much faster with $|\xi|$ and $|\eta|$ than for a Gaussian beam. This indicates that the width of the waist can be increased compared to the Gaussian case, without making the gratings larger. Here, we use $w_{sg} = 7.85 \cdot 10^{-4}$ m.

The super-Gaussian incident beam is specified on a transfer plane at the distance $L_{12} = 0.05$ m ahead of the first grating (see Figure 29). To make the beam waist coincide with the midpoint between gratings two and three, we set $z_{sg} = z_0 - L_{12} = -0.175$ m. As for the Gaussian incident beam, we choose the electric field to be polarized in the x-direction, which corresponds to

$$E^{(x)}(x,y,k) = \sqrt{\frac{\varepsilon}{\mu}} A_x \psi_{sg}\left(\frac{x}{w_{sq}}, \frac{y}{w_{sq}}, k\right), \quad E^{(y)}(x,y,k) = 0, \quad E^{(z)}(x,y,k) = 0,$$
$$H^{(x)}(x,y,k) = 0, \quad H^{(y)}(x,y,k) = \sqrt{\frac{\varepsilon}{\mu}} A_x \psi_{sg}\left(\frac{x}{w_{sq}}, \frac{y}{w_{sq}}, k\right), \quad H^{(z)}(x,y,k) = 0.$$

The magnetic field is converted into a surface current using the PO. As noted above, this procedure is exact because the incident plane is flat. The magnetic field and surface current on the transfer plane is represented on a regular mesh with 1000×1000 quads, and evaluated on the edge mid-points. The incident magnetic field on the first grating is then evaluated using the directional Chebyshev interpolation technique described above.

The time-dependent envelope function of the electric field can be obtained by inverse Fourier transforming $\widehat{p}E^{(x)}$. Figure 33 shows this quantity on the incident plane. Note the significant variation in phase in the radial direction and the "rounded square" shape of iso-levels in the magnitude.

For the case of perfect gratings, the electric field envelope on the observation plane is shown in Figure 34. Here we show two cross-sections of the solution: a (t,x)-plane along the center line $y = 0$, and a (x,y)-plane for a constant time. Note that the magnitude of $\mathcal{E}^{(x)}$ is well-focused both in space and time. The phase of $\mathcal{E}^{(x)}$ is approximately constant in time, but varies significantly with x and y. (As mentioned above, each black band indicates a 2π discontinuity in the phase due a branch cut in the $\tan^{-1}$ function).

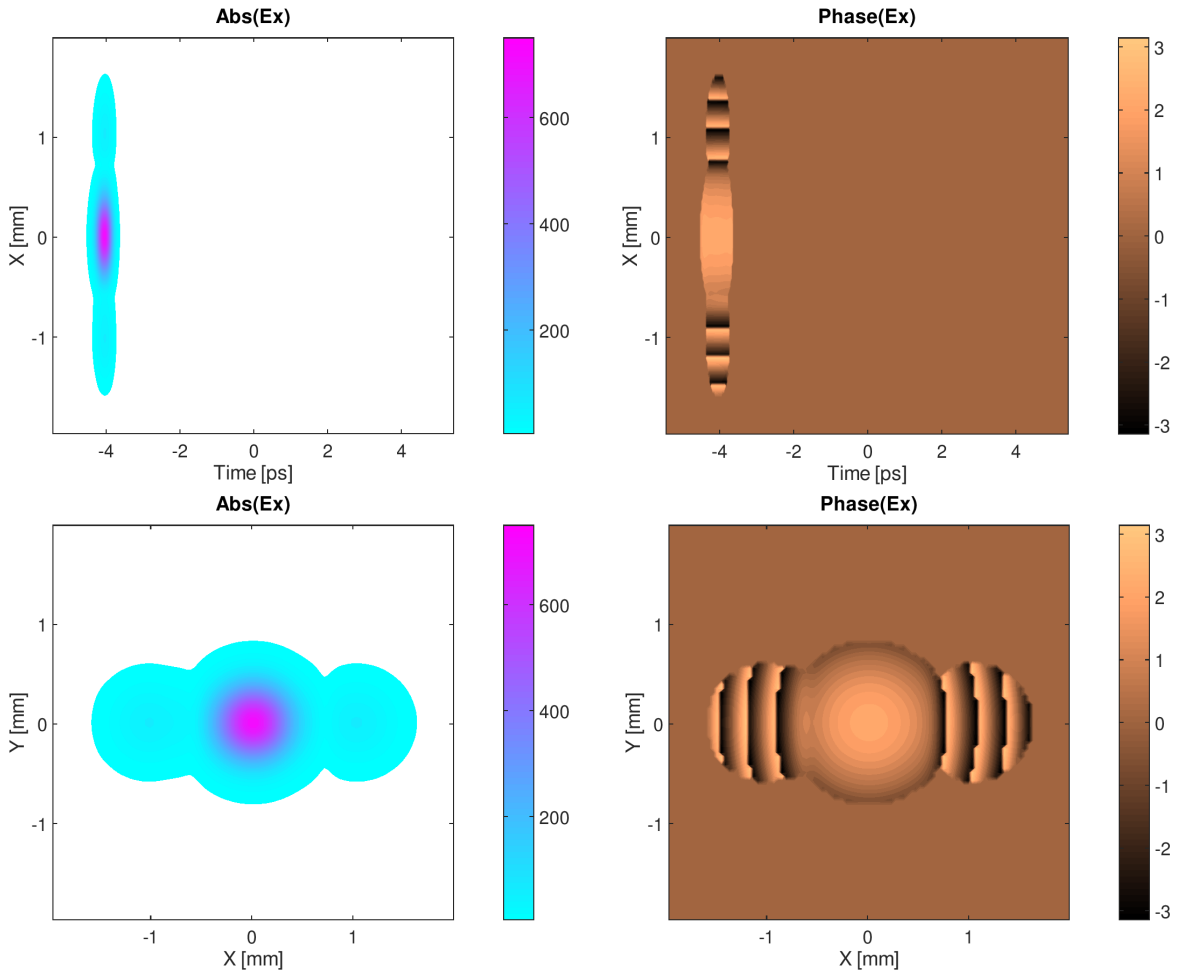

Figure 32: The $\mathcal{E}^{(x)}$ envelope on the observation screen for perturbation # 2 and a Gaussian incident beam. Left column: magnitude; right column: phase. Top row: $\mathcal{E}^{(x)}$ in the (t, x)-plane along the center line, $y = 0$. Bottom row: $\mathcal{E}^{(x)}$ in the (x, y)-plane for $t = -4.049 \cdot 10^{-12}$ s. Only $|\mathcal{E}^{(x)}| \geq 5$ is plotted.

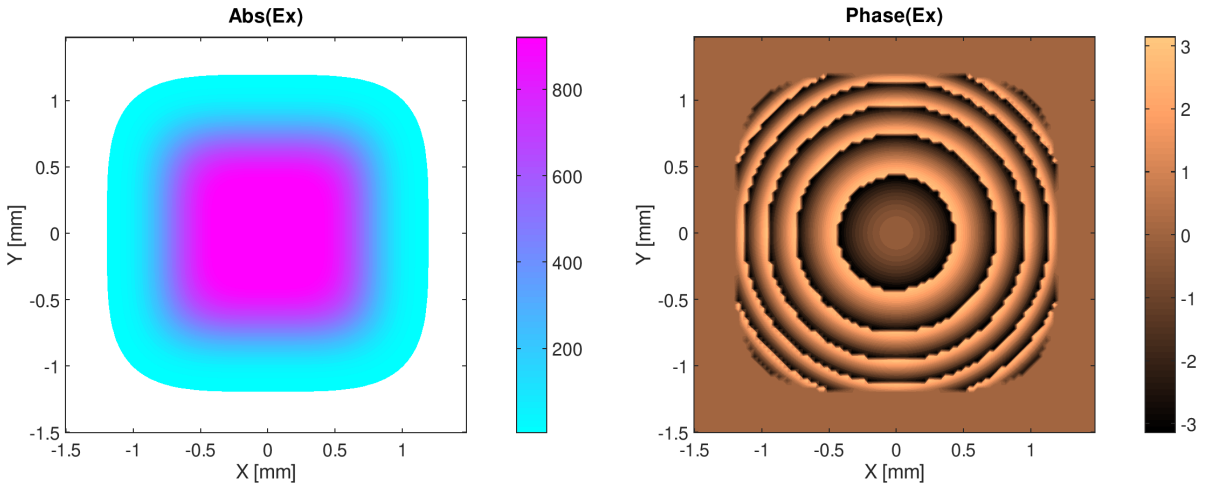

Figure 33: The time-dependent envelope function $\mathcal{E}^{(x)}$ for the super-Gaussian incident beam on the incident plane at $t = 0$. Left: magnitude, Right: phase. Only $|\mathcal{E}^{(x)}| \geq 5$ is plotted.

For grating perturbation # 1, the electric field envelope on the observation plane is shown in Figure 35. In the (t, x)-plane, the peak amplitude of the solution is lower, but both the amplitude and phase are otherwise very similar to the perfect case. However, in the (x, y)-plane, the solution is very different from the perfect case. An interesting observation is that the maximum magnitude now occurs along a diagonal line, with approximately constant phase along the perpendicular diagonal. This is likely due to the variation in line-period on the first grating, which perturbs the angular dispersion such that the beam is reflected in slightly different directions for different locations along the grating surface.

In comparing Figures 35 and 31, we note that the maximum magnitude occurs along the diagonal of the (x, y)-plane in both cases, but the diagonals are perpendicular. The reason for this behavior is currently not understood. In the super-Gaussian case, the magnetic field on the first grating is computed from the surface current on the incident plane. In the Gaussian case, it is evaluated from an analytical formula. To further investigate this discrepancy we could apply the incident plane approach for the Gaussian beam and compare the magnetic field on the first grating with the analytical formula.

We remark that the size of the observation screen had to be extended to 6 mm by 6 mm to capture the outgoing field for grating perturbation #1. To simplify graphical comparisons, the observation plane is shown at the same scale in Figures 34 and 35 . The size of gratings two and three were extended to 6.0 mm by 2.82 mm, and the size of the fourth grating was 5.0 mm by 3.0 mm.

Due to limited access to the Quartz machine, we were not able to simulate grating perturbation # 2 with a super-Gaussian incident beam.

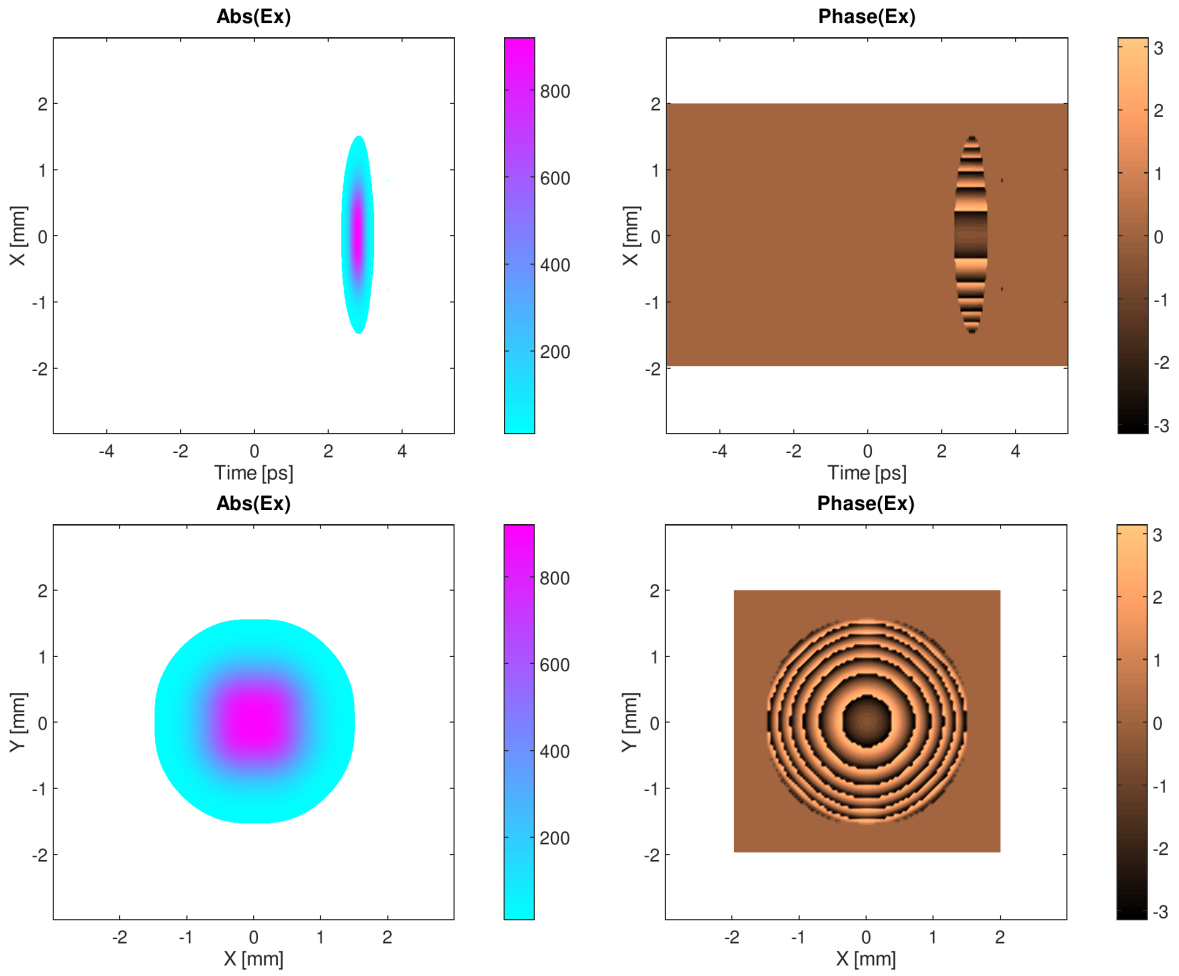

Figure 34: The $\mathcal{E}^{(x)}$ envelope on the observation screen for perfect gratings and a super-Gaussian incident beam. Left column: magnitude; right column: phase. Top row: $\mathcal{E}^{(x)}$ in the (t, x)-plane along the center line, $y = 0$. Bottom row: $\mathcal{E}^{(x)}$ in the (x, y)-plane for $t = 2.786 \cdot 10^{-12}$ s. Only $|\mathcal{E}^{(x)}| \geq 10$ is plotted.

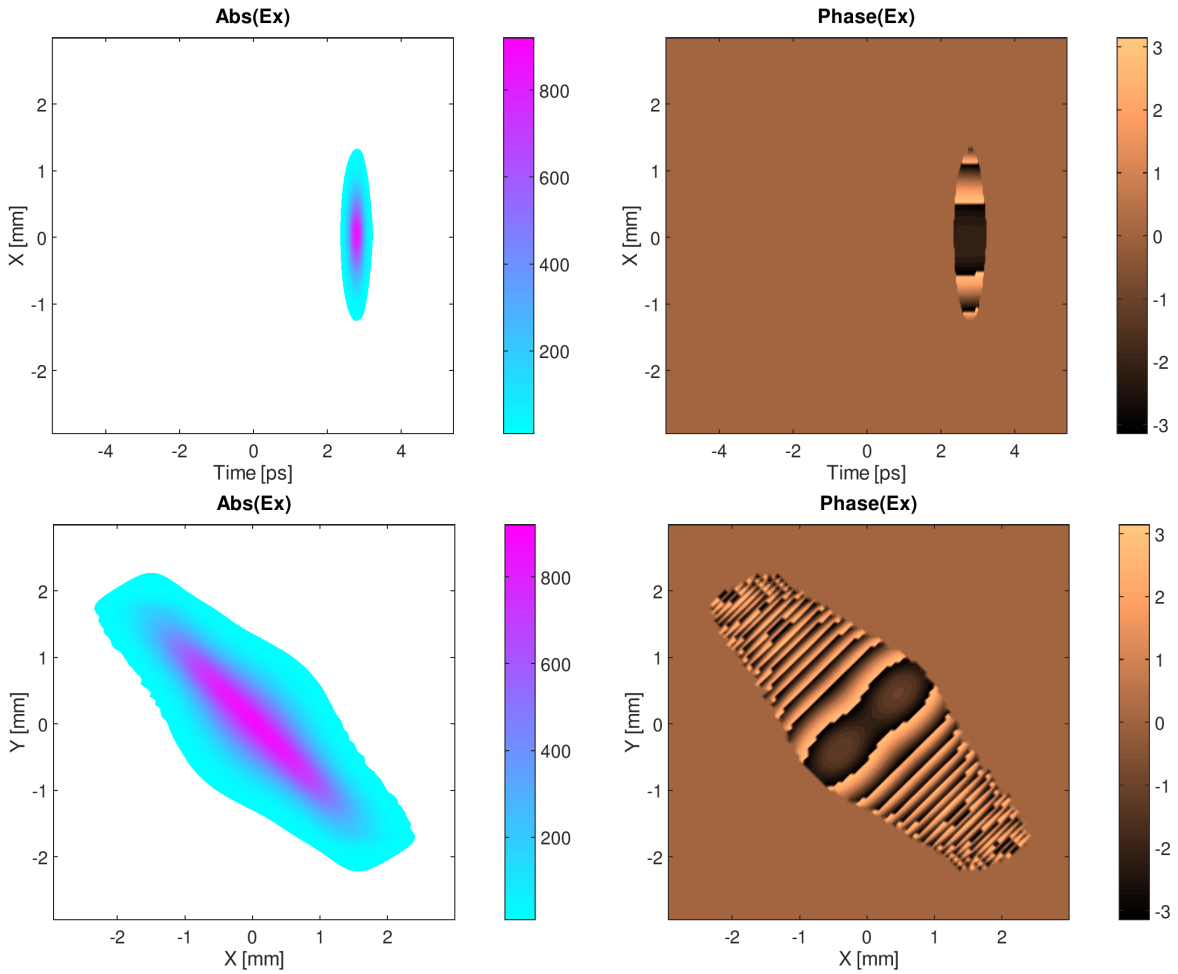

Figure 35: The $\mathcal{E}^{(x)}$ envelope on the observation screen for perturbation # 1 and a super-Gaussian incident beam. Left column: magnitude; right column: phase. Top row: $\mathcal{E}^{(x)}$ in the (t, x)-plane along the center line, $y = 0$. Bottom row: $\mathcal{E}^{(x)}$ in the (x, y)-plane for $t = 2.786 \cdot 10^{-12}$ s. Only $|\mathcal{E}^{(x)}| \geq 10$ is plotted.

8 Conclusions and outlook

We have described a numerical technique for simulating the propagation of a laser pulse through a grating compressor with metallic gratings. In the following description, we assume that the compressor consists of four gratings, but this is not a restriction of our approach. The incident pulse is first Fourier decomposed into a number of discrete frequency components, where each frequency corresponds to a monochromatic laser beam. For each frequency, the incident beam impinges on the first grating where it is diffracted towards the second grating. The diffracted beam from the first grating becomes the incident beam for the second grating, and so on, until the fourth grating is reached. The fourth grating diffracts the beam towards an observation plane, where the electric field is evaluated for that frequency. The procedure is repeated for all frequencies after which the electric field on the observation plane can be inverse Fourier transformed to obtain the electric field in the time domain. This electric field represents the outgoing laser pulse.

Our numerical technique for propagating each beam through the compressor is based on solving Maxwell's equations in the frequency domain using an integral representation of the solution in terms of the surface current. The surface current satisfies the electric field integral equation (EFIE). After discretization using a finite element method, the integral equation becomes a complex-valued linear system with a dense matrix, which can be solved iteratively using, e.g., the GMRES method. Our first major contribution is the implementation of a multi-level fast multipole algorithm (MLFMA) for accelerating the evaluation of the matrix-vector products during the iterative solution procedure. Due to an inherent numerical instability in the multipole expansion, a substantial part of the dense matrix can not be handled by the MLFMA and must be stored in memory. The memory requirement grows with the problem size and limit the applicability of the approach to gratings of size 0.1×0.1 mm^2.

Fortunately, we found that the physical optics (PO) approximation of the surface current can provide an accurate representation of the diffracted beam, particularly if it is scaled by a complex coefficient that only depends on the angle of incidence. With the PO approximation, the surface current follows directly from the incident magnetic field. Thus, the remaining computational challenge is to evaluate the integral representation of the magnetic field on a grating surface, due to the surface current on the preceding grating. For this purpose, we use a multi-level directional Chebyshev interpolation technique. Our second major contribution is the analysis of the accuracy of this technique and the implementation of the method in a parallel, distributed memory code called **js2js**. Based on this code, we are able to simulate a compressor with gratings of size 6×3 mm^2, using 64 nodes of a modern Linux cluster.

Compared to previous semi-analytical simulation techniques based on lumped optical element approximations of each grating, the proposed method allows arbitrary geometric perturbations of the grating line-profile to be analyzed by directly calculating the resulting electric field in the outgoing beam. We have successfully demonstrated this capability for two types of incident beams and two types of grating perturbations.

The directional Chebyshev techniques described in this paper could be generalized to simulate a much large compressor with decimeter-sized gratings. The calculation would

use the same hierarchical construction of source and receiver clusters and setup the same tree data structure, i.e., relatively few large clusters with many direction at the top level and many small clusters with only one direction at the leaf level. The key improvement would be to split the calculations into three basic stages:

1. E2M: Anterpolate point sources to the leaf level Chebyshev node points. The computational cost and memory requirement of this operation is linear in the total number of point sources, N_{tot}, and scales perfectly to many MPI-tasks on a parallel machine.

2. M2M, M2L, L2L: Use the current algorithm to anterpolate to the top level of the tree, transfer from the directional source clusters to the directional receiver clusters, and then interpolate down to the leaf level of the receiver tree. For a fixed number of clusters (N_{sc}, M_{rc}) and directions (N_{dir}), these operations require a constant amount of work, which can be distributed over not more than $N_{sc}M_{rc}$ MPI-tasks.

3. L2E: Interpolate from the leaf level Chebyshev node points in each cluster to the point receiver locations. Similar to the E2M operation, the cost and memory requirements of this work is linear in the number of receiver locations, M_{tot}, and scales perfectly to many MPI-tasks.

In the above approach, stages 1 (E2M) and 3 (L2E) could be executed on a much larger number of MPI-tasks than stage number 2, which only scales up to $N_{sc}M_{rc}$ tasks. While the memory requirements of stages 1 (E2M) & 3 (L2E) grow linearly with the total number of sources and receivers, the calculations in each cluster only depend on local data and is independent of all other clusters. These tasks can therefore be perfectly distributed over a large number of processors. The result of stage 1 (E2M) is the anterpolated source strengths at the Chebyshev node points in each cluster. This amount of data is independent of the size of the gratings and could be saved to a binary file, which would be read at startup of stage 2. After the M2M, M2L, and L2L operations are completed, another binary file could store the field values at the Chebyshev node point on the leaf level of the receiver tree. That file could then be read at startup of stage 3 (L2E). However, the result of stage 3 (L2E) is the interpolated magnetic field at all point receiver locations, which gives the surface current coefficients at all receiver locations. This amount of data would be large for a large grating, but it does not need to be saved to disk. The reason is that the surface current at all these points will only be used to calculate anterpolated source strengths for the next grating to grating calculation. To efficiently propagate the beam through the compressor it is therefore natural to group stage 3 (L2E) for grating $1 \rightarrow 2$ together with stage 1 (E2M) for grating $2 \rightarrow 3$, and so on. Then, we only need to read and write intermediate results for the Chebyshev node-points on the leaf level of the trees. This amount of data is independent of the size of the gratings.

The surface current on the first grating could either be obtained from an analytical formula (Gaussian beam), or by first calculating the equivalent surface current on a transfer plane, upstream of the first grating. Because the transfer plane is perpendicular to the direction of propagation, the magnetic field and surface current on that plane could be resolved on a relatively coarse mesh, from which the magnetic field on the first grating

could be evaluated. In a similar way, the electric field on the observation plane downstream of the last grating could also be resolved on a relatively coarse mesh. Thus, we could eliminate the need to store any large amounts of data between the various stages of a compressor simulation. The combined L2E and E2M operations could be run on a very large parallel machine, while the work for stage 2 (M2M, M2L, L2L) would be distributed over a smaller number of processes. Because the calculations for each wave number can be done independently, we could concurrently run stage 2 for many wave numbers and thus make use of much more than $N_{sc}M_{rc}$ processes in all stages of the algorithm.

Acknowledgments

This work was made possible by financial support from the Laboratory Directed Research and Development (LDRD) program at LLNL. The computer simulations were performed during a Dedicated Application Time (DAT) allocation on the Linux cluster Quartz at Livermore Computing. This work was performed under the auspices of the U. S. Department of Energy by Lawrence Livermore National Laboratory under Contract DE-AC52-07NA27344. This is contribution LLNL-TR-760459.

A Properties of the directional kernel in 1-D

We consider calculating the derivatives of the function

$$\kappa_1(\zeta) := e^{i\psi_1(\zeta)}, \quad \psi_1(\zeta) = \alpha + \beta_1\zeta + \frac{\gamma_1}{2}\zeta^2, \quad -1 \le \zeta \le 1, \tag{132}$$

where α, β_1 and γ_1 are real constants. Let $a := i\psi_1'$ and $b := i\psi_1''$. Because the third and all higher derivatives of ψ_1 are zero, the derivatives of κ_1 satisfy

$$\begin{aligned}
\kappa_1' &= \kappa_1 a, \\
\kappa_1'' &= \kappa_1 \left(a^2 + b\right), \\
\kappa_1^{(3)} &= \kappa_1 \left(a^3 + 3ab\right), \\
\kappa_1^{(4)} &= \kappa_1 \left(a^4 + 6a^2b + 3b^2\right), \\
&\vdots
\end{aligned}$$

In general, $\kappa^{(q)} = \kappa_1 P_q(a,b)$, where $P_q(a,b)$ is the polynomial

$$P_q(a,b) := p_{q,0}(a)^q + p_{q,1}(a)^{q-2}(b) + p_{q,2}(a)^{q-4}(b)^2 + \\ \ldots + p_{q,\lfloor q/2 \rfloor}(a)^{(q-2\lfloor q/2 \rfloor)}(b)^{\lfloor q/2 \rfloor}. \tag{133}$$

Due to the special structure of the phase function, the coefficients in (133) can be calculated explicitly.

Lemma 4. *The coefficients in the polynomial* (133) *are given by the formula*

$$p_{q,r} = 0, \quad q < 2r, \tag{134}$$

$$p_{q,r} = \frac{(2r)!}{2^r r!} \binom{q}{2r}, \quad q \geq 2r. \tag{135}$$

for $q = 0, 1, 2, \ldots$ *and* $r = 0, 1, 2, \ldots, \lfloor q/2 \rfloor$. *The coefficient of the last term in* (133) *corresponds to* $r = \lfloor q/2 \rfloor$. *If* q *is even,* $r = q/2$ *and* $2r = q$. *In this case,*

$$p_{q,\lfloor q/2 \rfloor} = \frac{q!}{\sqrt{2^q}(q/2)!}, \quad q \text{ even.}$$

If q *is odd,* $r = (q-1)/2$ *and* $2r = q-1$. *Thus,*

$$p_{q,\lfloor q/2 \rfloor} = \frac{(q-1)!\, q}{\sqrt{2^{(q-1)}}((q-1)/2)!} = \frac{q!}{\sqrt{2^{(q-1)}}((q-1)/2)!}, \quad q \text{ odd.}$$

Proof: The polynomial coefficients in (133) satisfy the recursion relations,

$$p_{q+1,0} = p_{q,0}, \qquad q \geq 1, \tag{136}$$

$$p_{q+1,1} = q p_{q,0} + p_{q,1} \qquad q \geq 2, \tag{137}$$

$$p_{q+1,2} = (q-2) p_{q,1} + p_{q,2}, \quad q \geq 4, \tag{138}$$

$$p_{q+1,3} = (q-4) p_{q,2} + p_{q,3}, \quad q \geq 6, \tag{139}$$

$$\vdots$$

The recursion starts with

$$p_{1,0} = 1, \quad p_{2,1} = p_{1,0}, \quad p_{4,2} = p_{3,1}, \ \ldots, \ p_{2r,r} = p_{2r-1,r-1}. \tag{140}$$

From (136) and (140) we get $p_{q,0} = 1$ for $q = 1, 2, 3, \ldots$. The recursion for next conefficient starts with $p_{2,1} = p_{1,0} = 1$, and by unrolling (137),

$$p_{q+1,1} = q + (q-1) + \ldots + 1 = \sum_{n=1}^{q} n = \frac{1}{2} q(q+1), \quad q \geq 1. \tag{141}$$

By insering the latter expression into (138) and unrolling the recursion,

$$2p_{q+1,2} = (q-2)(q-1)q + (q-3)(q-2)(q-1) + \ldots + 6.$$

We have $(q-2)q = (q-1)^2 - 1$, which gives

$$2p_{q+1,2} = \sum_{n=1}^{q-1} (n^3 - n) = \frac{1}{4}(q-1)^2 q^2 - \frac{1}{2}(q-1)q,$$

where we used Faulhaber's formula to calculate $\sum n^3$. We arrive at

$$p_{4,2} = p_{3,1} = 3, \tag{142}$$

$$\begin{aligned} p_{q+1,2} &= \frac{1}{8}\left((q-1)^2q^2 - 2(q-1)q\right) \\ &= \frac{1}{8}(q+1)q(q-1)(q-2), \quad q \geq 3. \end{aligned} \tag{143}$$

The first three coefficients thus satisfy

$$p_{q,0} = 1, \tag{144}$$

$$p_{q,1} = \frac{1}{2}q(q-1), \quad q \geq 2, \tag{145}$$

$$p_{q,2} = \frac{1}{8}q(q-1)(q-2)(q-3), \quad q \geq 4, \tag{146}$$

and a pattern is starting to emerge. For next coefficient, we make the ansatz

$$p_{q,3} = A_3 q(q-1)(q-2)(q-3)(q-4)(q-5),$$

which gives

$$A_3\left((q+1) - (q-5)\right)q(q-1)(q-2)(q-3)(q-4) = (q-4)p_{q,2},$$

when inserted into (139). By inserting (146) into the right hand side of the above expression, it simplifies to

$$6A_3 = \frac{1}{8}, \quad A_3 = \frac{1}{48}.$$

The procedure can be repeated to calculate all higher coefficients. It is convenient to write them on the form

$$p_{q,r} = A_r(2r)!\binom{q}{2r}, \quad q \geq 2r. \tag{147}$$

From (144)-(146), $A_0 = 1$, $A_1 = 1/2$, and $A_2 = 1/8$. After some algebra we find that A_r satisfies

$$A_r = \frac{1}{2r}A_{r-1} = \frac{1}{2r(2r-2)}A_{r-2} = \ldots = \frac{1}{2^r r!}.$$

References

[1] David A. Alessi, Paul A. Rosso, Hoang T. Nguyen, Michael D. Aasen, Jerald A. Britten, and Constantin Haefner. Active cooling of pulse compression diffraction gratings for high energy, high average power ultrafast lasers. *Opt. Expr.*, 24(26):30015, 2016.

[2] F.P. Andriulli, K. Cools, H. Bağci, F. Olyslager, A. Buffa, S. Christiansen, and E. Michielssen. A multiplicative calderon preconditioner for the electric field integral equation. *IEEE Trans. Antennas Propag.*, 56(8):2398–2412, 2008.

[3] C. A. Balanis. *Advanced Engineering Electromagnetics*. Wiley, New York, 1989.

[4] C.P.J. Barty, M. Key, J. Britten, R. Beach, G. Beer, C. Brown, S. Bryan, J. Caird, T. Carlson, J. Crane, J. Dawson, A.C. Erlandson, D. Fittinghoff, M. Hermann, C. Hoaglan, A. Iyer, L. Jones II, I. Jovanovic, A. Komashko, O. Landen, Z. Liao, W. Molander, S. Mitchell, E. Moses, N. Nielsen, H-H. Nguyen, J. Nissen, S. Payne, D. Pennington, L. Risinger, M. Rushford, K. Skulina, M. Spaeth, B. Stuart, G. Tietbohl, and B. Wattellier. An overview of llnl high-energy short-pulse technology for advanced radiography of laser fusion experiments. *Nucl. Fusion*, 44:S266–S275, 2004.

[5] A. Buffa and S.H. Christiansen. A dual finite element complex on the barycentric refinement. *Math. Comput.*, 76(260):1743–1769, 2007.

[6] W. Cai. High-order mixed current basis functions for electromagnetic scattering of curved surfaces. *J. Scient. Comput.*, 14:73–105, 1999.

[7] R. Chang and V. Lomakin. Quadrilateral barycentric basis functions for surface integral equations. *IEEE Trans. Antennas Propag.*, 61(12):6039–6050, 2013.

[8] W. Diels and W. Rudolph. *Ultrashort Laser Pulse Phenomena*. Elsevier, 2nd edition, 2006.

[9] M.G. Duffy. Quadrature over a pyramid or cube of integrands with a singularity at a vertex. *SIAM J. Numer. Anal.*, 19(6):1260–1262, 1982.

[10] B. Engquist and L. Ying. Fast directional multilevel algorithms for oscillatory kernels. *SIAM J. Sci. Comput.*, 29(4):1710–1737, 2007.

[11] C. Fiorini, C. Sauteret, C. Rouyer, N. Blanchot, S.Seznec, and A. Migus. Temporal aberrations due to misalignments of a stretcher-compressor system and compensation. *IEEE J. Quant. Electr.*, 30(1):1662, 1994.

[12] S. Fourmaux, C. Serbanescu, L. Lecherbourg, S. Payeur, F. Martin, and J. C. Kieffer. Investigation of the thermally induced laser beam distortion associated with vacuum compressor gratings in high energy and high average power femtosecond laser systems. *Opt. Expr.*, 17(1):178, 2008.

[13] W.C. Gibson. *The Method of Moments in Electromagnetics*. Chapman & Hall/CRC, 2008.

[14] L. Greengaard and V. Rokhlin. A fast algorithm for particle simulations. *J. Comput. Phys.*, 73:325–348, 1987.

[15] M. Lax, W. H. Louisell, and W. B. McKnight. From Maxwell to paraxial wave optics. *Phys. Rev. A*, 11(4):1365–1370, 1975.

[16] E.G. Loewen and E. Popov. *Diffraction Gratings and Applications*. Optical engineering. Marcel Dekker, 1997.

[17] J. Ma, P. Yuan, J. Wang, Y. Wang, G. Xie, H. Zhu, and L. Qian. Spatiotemporal noise characterization for chirped-pulse amplification systems. *Nature Comm.*, 6:6192, 2015. doi: 10.1038/ncomms7192.

[18] O.E. Martinez. Design of high-power ultrashort pulse amplifiers by expansion and recompression. *IEEE J. Quant. Elect.*, QE-23(8), Aug. 1987.

[19] M. Messner, M. Schanz, and E. Darve. Fast directionl multilevel summation for oscillatory kernels based on Chebyshev interpolation. *J. Comput. Phys.*, 231:1175–1196, 2012.

[20] S.M. Rao, D.R. Wilton, and A.W. Glisson. Electromagnetic scattering by surfaces of arbitrary shape. *IEEE Trans. Antennas Propag.*, AP-30(3):409–418, 1982.

[21] R. A. Sacks, K. P. McCandless, E. Feigenbaum, J.-M. G. Di Nicola, K. J. Luke, W. Riedel, R. J. Learn, and B. J. Kraines. The virtual beamline (VBL) laser simulation code. In A. A. S. Awwal and M. A. Lane, editors, *High power lasers for fusion research III*, volume 9345 of *Proceedings of SPIE*, 2015.

[22] J. M. Song and W. C. Chew. Error analysis for the truncation of multipole expansion of vector Green's functions. *IEEE Mictrowave Wireless Components Lett.*, 11(7):311–313, 2001.

[23] J.A. Stratton and L.J. Chu. Diffraction theory of electromagnetic waves. *Phys. Rev.*, 56:99–107, 1939.

[24] D. Strickland and G. Mourou. Compression of amplified optical pulses. *Opt. Comm.*, 56(3):219–221, 1985.

[25] E. B. Treacy. Pulse compression with diffraction gratings. *IEEE J. Quant. Electr.*, QE-5(9):454, 1969.

[26] L.N. Trefethen. *Approximation theory and approximation practice*. SIAM, 2013. ISBN: 978-1-611972-39-9.

[27] J.L. Volakis and K. Sertel. *Integral Equation Methods for Electromagnetics*. Electromagnetics and Radar. Scitech Publishing, 2012.